UNIVERSITY OF CALGARY

Effect of Temperature on Asphaltene Deposition Mechanisms in Horizontal Flow

by

Nicson Do

A THESIS
SUBMITTED TO THE FACULTY OF GRADUATE STUDIES
IN PARTIAL FULFILMENT OF THE REQUIREMENTS FOR THE
DEGREE OF MASTER OF SCIENCE

GRADUATE PROGRAM IN CHEMICAL ENGINEERING

CALGARY, ALBERTA

DECEMBER, 2021

Abstract

Asphaltene deposition is a longstanding flow assurance issue that has been extensively investigated at near ambient temperatures where asphaltenes typically precipitate as glassy particles. However, at the higher temperatures sometimes encountered in deep formations, asphaltenes may come out of solution as liquid droplets. Deposition at these conditions has not been rigorously examined. The purpose of this study was to investigate deposition behavior in the liquid droplet regime and compare it with deposition in the glassy particle regime.

An apparatus was designed and commissioned to investigate deposition mechanisms over a range of temperatures in horizontal laminar flow using a test fluid of bitumen diluted with n-heptane. Pre-diluted bitumen and additional n-heptane were fed through a static mixer to induce asphaltene precipitation and the subsequent mixture was then displaced through a capillary tube test section. The pressure drop across the test section was monitored for indications of deposition during the flow period, and the capillary tube was removed from the apparatus at the end of each experiment to measure the mass and location of the deposit. Asphaltene deposition was assessed considering the following variables: capillary tube lengths from 3 to 30 cm, solvent contents in the feed from 65 to 90 wt% n-heptane, fluid flow rates of 2 and 4 cm³/min, and temperatures from 50 to 130°C.

In the glassy particle regime, a highly porous, orifice-like deposit with a high solvent content formed near the inlet of the test section. The fully developed wet deposit occupied 37% of the tube volume on average. The initial deposition rate increased as the solvent content in the feed increased. Cycles of deposition and erosion were observed during the flow period. The results were consistent with the literature.

In the liquid droplet regime, periodically unstable stratified flow was observed. The heavy phase hold up cycled from 70 to 98% of the tube volume. The solvent content of the heavy phase was lower compared to glassy particle deposits and consistent with equilibrium heavy phase compositions reported in the literature. The heavy phase accumulated faster as the solvent content in the feed increased. In one experiment, an orifice-like deposit appeared to form at the start of the experiment indicating that, even in the liquid regime, deposition may occur near a flow

disturbance. However, the effect of the orifice was overwhelmed by the accumulation of the flowing heavy phase. The results suggest that the models and treatments developed for deposition in the glassy particle regime may not apply in the liquid regime.

Acknowledgement

First, I would like to thank my supervisor, Dr. Harvey Yarranton, for your continuous support, encouragement, advice, and patience. It has been a privilege to work alongside you as your student and to be a part of your research team. Thank you for always believing in me and challenging me to grow both personally and professionally. I appreciate your mentorship and your dedication towards all your students. I will always carry and pass along your teachings in my engineering career.

I would also like to express my gratitude to my Lab Manager, Florian Schoeggl. Thank you for sharing your wealth of experience with me, the fruitful discussions we had in your office, and the story about the "little red engine". Your thoughtful guidance and mind-expanding questions during the setup of my apparatus and experiments have made me a better engineer and person. I would also like to thank Elaine Baydak for her support and guidance in the laboratory. Your small gestures of bringing us treats during the holidays have always had a big impact of brightening our moods after a long day in the lab.

Thank you to the Natural Science and Engineering Research Council of Canada (NSERC) for funding this research project.

I would like to thank my friends, especially Javier, Laura, Daniela, and John for all the laughter and good times we shared together. I would also like to thank all current and past members of the HOPP research group: Sandra, Franklin, Andres, Yulman, Jairo, John, Emilio, Nicolay, Javier, Daniela, Amir, Benjamin, José, Alejandra, Carolina, and Kaveh. A special shout out to Daniela, who helped me tremendously with modeling the asphaltene yields in this thesis.

Finally, I would like to acknowledge my family and partner, Lilian, for all their love and support.

Dedication

To my family and my partner Lilian whose kindness and strength inspires me to be better everyday

Table of Contents

List of Tables

List of Figures

List of Symbols, Abbreviations, and Nomenclature

Symbols

A	Area available for deposition
A^H	Area occupied by the heavy phase
A^L	Area occupied by the light phase
A^*	Bitumen specific parameter in density correlation
A_0	Fitting parameter for dilute gas viscosity
A_p	Cross sectional area of the particle
A_Σ	Total cross sectional area of capillary tube
a	Fitting parameter in shear removal term for Eskin *et al.* deposition model
a_1, a_2, a_3, a_4	Fitting parameters in Watkinson's transport-adhesion model
a_1^*, a_2^*	Fluid specific parameters in effective density correlation
B^*	Bitumen specific parameter in density correlation
B_0	Fitting parameter for dilute gas viscosity
B_1	Adjustable constant in empirical fitting equation for asphaltene yield
b	Fitting parameter in shear removal term for Eskin *et al.* deposition model
b_1^*, b_2^*	Fluid specific parameters in effective density correlation
C	Particle concentration
C^*	Bitumen specific parameter in density correlation
C_A	Concentration of asphaltene particles
C_A^{eq}	Concentration of asphaltene particles at equilibrium
C_b	Concentration of asphaltenes in the bulk of the fluid
C_D	Drag coefficient
C_o	Orifice discharge coefficient
C_0	Concentration of asphaltenes at the inlet
C_1	Adjustable constant in empirical fitting equation for asphaltene yield
c_2, c_3	Fluid specific parameters in Expanded Fluid Viscosity Model
D	Diameter of the capillary tube
D^*	Bitumen specific parameter in density correlation

D_A	Diffusivity constant for asphaltenes
D_{Br}	Brownian diffusivity
D_h^L	Hydraulic diameter of the light phase
D_p	Diameter of the asphaltene particle
D_{turb}	Turbulent diffusivity
D_0	Fitting parameter for dilute gas viscosity
d	Average particle diameter
d_{cr}	Critical particle diameter
d_i	Diameter of an ith size particle
d_o	Diameter of the orifice
E	Activation energy
E_0	Fitting parameter for dilute gas viscosity
F_{ad}	Adhesion force
F_d	Drag force
f	Fanning friction factor
h^H	Height of heavy phase
h^L	Height of light phase
i_{cr}	Size fraction number corresponding to critical particle diameter
J	Mass flux
K_i	Partition coefficient for component i in Modified Regular Solution model
k_{Ag}	Kinetic constant for asphaltene aggregation
k_B	Boltzmann constant
k_D	Kinetic constant for asphaltene deposition
k_f	Thermal conductivity
k_m	Mass transfer coefficient
k_P	Kinetic constant for asphaltene precipitation
k_{sr}	Empirical term for shear removal in for Eskin *et al.* deposition model
L	Length of the capillary tube
L_{dep}	Length of the deposit
MW_m	Molecular weight of component m

$\dot{m}_{bit}^{H}$	Bitumen flow rate in heavy phase
$\dot{m}_{dep}$	Deposition rate per unit area
$m(t)_{dep}$	Estimated mass of deposition at time t
m_i	Total mass of asphaltene particles in i^{th} size fraction
N_i	Concentration of particles in the ith size fraction by number
N_{01}	Initial number concentration of particles in first size fraction at the onset of precipitation
n	Fitting parameter in shear removal term for Eskin *et al.* deposition model
nc	Number of components in the system
P	Pressure
P^H	Wetted perimeter of heavy phase
P^L	Wetted perimeter of light phase
Q	Volumetric flow rate
Q_{feed}	Total feed flow rate
q_A	Corrected asphaltene deposition mass fluz
q_Σ	Total deposition mass flux
R	Universal gas constant
Re	Reynolds number
R_{fo}	Thermal resistance due to fouling
Re_p	Particle Reynolds number
r	Radial direction
S	Sticking probability
S_i	Shattering rate
S_o	Empirical constant for sticking probability
SG_{bit}	Specific gravity of bitumen
SG_{C7}	Specific gravity of *n*-heptane
T	Temperature
T_f	Temperature of fluid
T_s	Temperature of deposition surface
t	Time

U	Heat transfer coefficient
V^H	Volume occupied by heavy phase
V_{dep}	Volume of deposit
V_k^H	Volume of heavy phase at time step k
V_Σ	Volume of capillary tube
v	Fluid velocity
v_{dBi}	Most probable fluctuation velocity for i^{th} size particles due to Brownian motion
v_{dtbi}	Most probable fluctuation velocity for i^{th} size particles due to turbophoresis
v_{dti}	Most probable fluctuation velocity for i^{th} size particles due to turbulent motion
v_p	Velocity of asphaltene particle
$\langle v_z \rangle$	Average fluid velocity under turbulent conditions
W	Volume of Couette cell
w	Width of circle segment
$w_{A,i}$	Mass fraction of asphaltene pseudo-component i
w_{bit}	Mass fraction of bitumen in mixture
w_{C7}	Mass fraction of n-heptane in mixture
$w_{C7\ dep}$	Mass fraction of n-heptane in deposit
x	Mole fraction
x_{dep}	Deposit thickness
Y	Asphaltene yield
Y_{bit}	Bitumen yield
y	Vertical distance from wall
z	Axial direction

Superscripts

Br	Brownian
eq	Equilibrium

H	Heavy phase
i	Section of capillary tube
L	Light phase
turb	Turbulent
298	At 298 Kelvin

Subscripts

A	Asphaltene
Ag	Aggregation
ad	Adhesion
Br	Brownian
b	Bulk
batch	Batch system
bit	Bitumen
C7	*n*-heptane
cr	Critical
D	Deposition
d	Drag
f	Fluid
h	Hydraulic
i	Size fraction of particle
j	Size fraction of particle
k	Time step
m	Component
n	Component
non-solvent	Non-solvent component
onset	At onset condition
P	Precipitation
p	Particle
s	Surface
sb	Between solvent and bitumen

sl	Slurry
sr	Shear removal
$turb$	Turbulent
w	Wall
Σ	Total

Greek Symbols

$\alpha_{i,j}$	Collision efficiency
β	Fluid specific parameter that correlates changes in density to changes in viscosity in Expanded Fluid Viscosity Model
$\beta_{i,j}$	Collision frequency function
$\beta_{i,j}^{Br}$	Collision frequency function from Brownian motion
$\beta_{i,j}^{turb}$	Collision frequency function from turbulent motion
β_{sb}	Density binary interaction parameter between solvent and bitumen
β_{sb}^{298}	Density binary interaction parameter between solvent and bitumen at 298 K
$\Gamma_{i,j}$	Breakage distribution function
γ	Activity coefficient
γ_p	Particle-wall interaction efficiency
δ	Solubility parameter
$\delta_{A,i}^{0}$	Solubility parameter of pseudo-component i at 25°C and 0.1 MPa
δ_{max}^{0}	Maximum solubility parameter of pseudo-component i at 25°C and 0.1 MPa
δ_{min}^{0}	Minimum solubility parameter of pseudo-component i at 25°C and 0.1 MPa
ε_{sb}	Viscosity binary interaction parameter between solvent and bitumen
θ	Central angle of the circle
μ	Viscosity of the fluid
μ_D	Dilute gas viscosity
μ_{sl}	Viscosity of the slurry

v	Molar volume
v_{bit298}	Specific volume of bitumen at 298 Kelvin
v_{C7298}	Specific volume of n-heptane at 298 Kelvin
ξ_k	Fraction of heavy phase that accumulates during time step k
ρ	Density of fluid
ρ^H	Density of heavy phase
$\rho_{A,i}^0$	Density of pseudo-component i at 25°C and 0.1 MPa
$\rho_{A,i}$	Density of pseudo-component i at temperature of system
ρ_{bit}	Density of bitumen
ρ_{C7}	Density of n-heptane
ρ_{mix}	Density of mixture
$\rho_{non\text{-}solvent}$	Density of non-solvent component
ρ_S^0	Fluid specific parameter in Expanded Fluid Viscosity Model
ρ_S^*	Compressed state density
τ_w	Shear stress at wall
φ	Volume fraction
φ^H	Volume fraction of heavy phase
ψ	Deposition efficiency

Abbreviations

ADEPT	Asphaltene Deposition Tool
CO_2	Carbon Dioxide
GOR	Gas Oil Ratio
ID	Inner Diameter
MRS	Modified Regular Solution
OD	Outer Diameter
SAGD	Steam Assisted Gravity Drainage
SARA	Saturates Aromatics Resins Asphaltenes

Chapter 1: Introduction

Asphaltenes are the heaviest fraction of crude oil that can precipitate out of solution when there are changes in pressure, temperature, or composition. Once precipitated, asphaltenes may form deposits in porous media (reservoirs) or in open flow (wellbores, pipelines, oil and gas facilities). In the reservoir, asphaltene deposition can result in formation damage, which impedes hydrocarbons from reaching the wellbore and significantly reduces the productivity of the reservoir (Srivastava *et al.* 1999; Seifried *et al.* 2013; Eskin *et al.* 2016). Asphaltene deposition in the reservoir and in open flow differ; this thesis focuses on open flow.

During live oil production and transport, asphaltenes may form deposits on the surface of wellbores and pipelines (Vargas *et al.* 2010; Eskin *et al.* 2011). As asphaltenes gradually adhere and accumulate onto the walls of wellbore/pipeline tubing, the diameter available for flow decreases resulting in higher pressure drops across the affected regions and lower production rates. Typically, chemical (xylene injection) or mechanical (jetting, scraping) methods are used to clean the deposits but are only partially effective. In addition to the economic costs associated with production losses, there are environmental costs related to consuming more fuel to provide enough pumping power to overcome pressure losses.

Asphaltene deposition can be a significant issue for undersaturated light crude oils (de Boer *et al.* 1995; AlHammadi *et al.* 2017). Lighter oils contain a significant amount of dissolved gases such as CO_2 or methane which are precipitants for asphaltenes. Therefore, oils with a high gas-oil ratio (GOR) tend to precipitate asphaltenes when depressurized leading to asphaltene deposition (Zhang *et al.* 2017; AlHammadi *et al.* 2017). Although deposition has been a flow assurance issue for a long time, it has proven challenging to assess in the laboratory and scale to field conditions.

Asphaltene deposition has been studied extensively at near ambient temperatures where asphaltenes are commonly considered to precipitate as glassy particles (Broseta *et al.* 2000; Wang *et al.* 2004; Nabzar and Aguilera, 2008; Seifried *et al.* 2013; Hoepfner *et al.* 2013; Vilas Bôas Fávero *et al.* 2016; Ghahfarokhi *et al.* 2017; Behmani *et al.* 2019). Several models have been

developed to predict and describe asphaltene deposition including include the deposition model created by Eskin *et al.* (2011) and the ADEPT model developed by Vargas *et al.* (2010). Both models incorporate important steps that affect asphaltene deposition, including precipitation, aggregation, transport, adhesion, and erosion. A shortcoming to these models is their sole applicability to particle deposition.

Asphaltene deposition at higher temperatures encountered in deep, offshore production has not been rigorously investigated. For example, asphaltene deposition has been reported in offshore developments in the Gulf of Mexico, Adriatic Sea, and the Persian Gulf, where reservoir temperatures may reach 80 to 130°C (Cenegy, 2001; Eskin *et al.* 2016). At these temperatures, asphaltenes may undergo glass transition and come out of solution as liquid droplets (Johnston *et al.* 2017; Duran *et al.* 2018). Deposition mechanisms for dispersed liquids likely differ significantly from those for dispersed particles.

1.1 Objectives

This thesis aims towards identifying and understanding the mechanisms involved in asphaltene deposition at elevated temperatures, where the precipitated asphaltenes have a morphological change from glassy particles to liquid droplets. Deposition at lower temperatures in the glass particle regime is also assessed in order to provide a baseline for comparison. The test fluid is bitumen diluted with *n*-heptane. This fluid was selected to ensure a sufficient mass of asphaltenes in the fluid to obtain measureable deposits in a practical run time and fluid usage rate. The fluid is not the same as typical offshore reservoir fluids but the mechanisms of the deposition process are expected to be similar.

The objectives of the thesis are as follows:
1. Design and commission an apparatus to measure asphaltene deposition from mixtures of *n*-heptane and bitumen in a horizontal flow configuration through a capillary tube. In this apparatus, the bitumen is first pre-diluted with *n*-heptane to a point below the onset of precipitation to reduce its viscosity and promote rapid mixing. Next, additional solvent and pre-diluted bitumen are displaced through a static mixer to generate asphaltene precipitation before entering the capillary tube test section. The pressure drop across the

test section is monitored during the flow period and used as an indicator of deposition. The mass and location of the deposit can be analyzed by removing the test section.

2. Develop procedures to ensure that meaningful data could be collected with the new apparatus, specifically:

   a. a methodology to assess that the experimental fluid is well mixed before entering the test section.

   b. a procedure to remove the residual fluid at the end of each experiment without altering the deposit.

3. Measure the pressure drop profiles, mass of deposit, and solvent content of deposit in deposition experiments. Evaluate the following variables:

   a. capillary tube lengths of 3, 15, 16.5, and 30 cm.

   b. solvent contents in the feed of 65, 75, and 90 wt% n-heptane.

   c. fluid flow rates of 2 and 4 cm³/min.

   d. temperatures of 50°C, 90°C, and 130°C.

4. Compare the measurements with literature data where applicable to validate the results.

5. Identify the deposition mechanism at different temperatures.

1.2 Thesis Structure

This thesis is organized into six chapters and the remaining five chapters are outlined below:

Chapter 2 reviews relevant background material related to asphaltene deposition. Preceding and concurrent steps to asphaltene deposition such as asphaltene precipitation, aggregation, and adhesion are discussed. Previous experimental methods and studies used to examine asphaltene deposition are reviewed. Existing asphaltene deposition models are also presented and discussed.

Chapter 3 describes the design of the asphaltene depositon apparatus and the experimental procedures used in this thesis to collect asphaltene deposition data. The design checks used to ensure that accurate and representative data could be obtained from the apparatus are also presented.

Chapter 4 presents the measurements from asphaltene deposition experiments in the glassy particle regime. The effects of capillary tube length, solvent composition in the feed, flow rate, and temperature on asphaltene deposition are discussed. The experimental data is analyzed to provide estimates of the initial deposition rates in addition to the size and length of the deposits. The experimental results obtained are compared with data from the literature.

Chapter 5 presents a preliminary study of asphaltene deposition in the liquid droplet regime. The change in deposition mechanism is identified and discussed in detail. The effects of capillary tube length and solvent composition in the feed are discussed.

Chapter 6 summarizes the main contributions and findings from this thesis. Recommendations for future studies with the apparatus are also discussed

Chapter 2: Literature Review

This chapter begins with a review of crude oil composition and chemistry with an emphasis on asphaltenes. Then, the literature related to asphaltene deposition are reviewed. Asphaltene precipitation, asphaltene particle aggregation and asphaltene adhesion are significant steps in asphaltene deposition and are all discussed. The chapter concludes with a discussion of deposition measurements, results from previous deposition studies, and a review of asphaltene deposition models.

2.1 Crude Oil Chemistry

2.1.1 Crude Oil Composition

Crude oils are naturally occurring complex liquid petroleum mixtures. The primary constituents of petroleum are hydrocarbons, but crude oils also contain organic compounds such as nitrogen, oxygen and sulfur as well as metals, specifically iron, nickel and vanadium. The quality of a crude oil is tied to its composition, with higher quality crude oils being easier to process and refine into useful petroleum products. Physical properties that are easy to measure, such as boiling point, density and viscosity are commonly used to define the quality of an oil. These properties are shown in Table 2.1 for different types of crude oil (Ramirez-Corredores, 2017).

Table 2.1: Selected physical properties of different types of crude oil. Adapted from Ramirez-Corredores (2017).

Classification	Mean Boiling Point, °C	Viscosity cSt	Density kg/m³	API Gravity
Extra Light	<350	<2	<830	>39
Light	250 – 450	2 – 10	830 – 870	31.1 – 39
Median	300 – 500	10 – 100	870 – 920	22.3 – 31.1
Heavy	400 – 600	100 – 5000	920 – 1000	10.0 – 22.3
Extra Heavy	>500	>5000	>1000	>10

The hydrocarbons found in crude oil can be generalized into three chemical classes depending on their molecular structures (Speight, 2007):

- Paraffins are saturated hydrocarbons can be further broken down into *n*-paraffins and iso-paraffins. *n*-Paraffins are straight chained hydrocarbons while and iso-paraffins contain branched chains.

- Naphthenes are saturated hydrocarbons and are also known as cycloparaffin hydrocarbons. They contain as least one ring structure with the majority of naphthene rings consisting of five or six carbon atoms.

- Aromatics are hydrocarbons that contained at least one benzene ring. They may also be connected to paraffinic side chains or naphthenic rings. In general, an increase in the aromaticity of a crude oil is also linked to an increase in boiling temperature (Ramirez-Corredores, 2017).

Although crude oil components fall into the above three classes, there are hundreds of thousands, if not millions, of different molecular species within a crude oil. As the carbon number increases, the number of isomers and compounds that can be formed also increases significantly. Clearly, it is not feasible to distinguish and describe every molecule. Instead, crude oils are characterized into a relatively small fraction of components based on gas chromatographic, distillation, solubility, and liquid chromatographic assays.

One approach that is often used to characterize heavy oils is the SARA characterization method. SARA fractionation defines crude oil in terms of saturates, aromatics, resins and asphaltenes. Asphaltenes are separated based on their solubility, and the other three fractions, collectively known as maltenes, are separated using liquid chromatography. A complete description of the methodology is provided in ASTM D2007 and ASTM D4124. This thesis focuses on the asphaltenes.

2.1.2 Asphaltenes

Asphaltenes are defined as the petroleum components insoluble in *n*-alkanes (such as *n*-pentane or *n*-heptane) and soluble in aromatic solvents (such as toluene). They are the densest, highest molecular weight, and most polar components of crude oil (Ramirez-Corredores, 2017; Speight and Long, 1996). Asphaltenes are not a single component but rather a complex mixture of different molecules each consisting of one or more polynuclear aromatic cores linked to alkyl and cycloalkyl side chains (Speight and Long, 1996). They also contain a high number of heteroatoms (nitrogen,

oxygen, and sulfur) and metals (such as vanadium and nickel) compared to the rest of the crude oil (Gray, 2015). Examples of typical asphaltene molecules are shown in Figure 2.1. Asphaltene monomer molecular weights range from 400 to 1000 g/mol and their densities range from 1.0 to 1.2 g/cm³ (Mullins, 2008; Yarranton *et al.* 2013; Barrera *et al.* 2013).
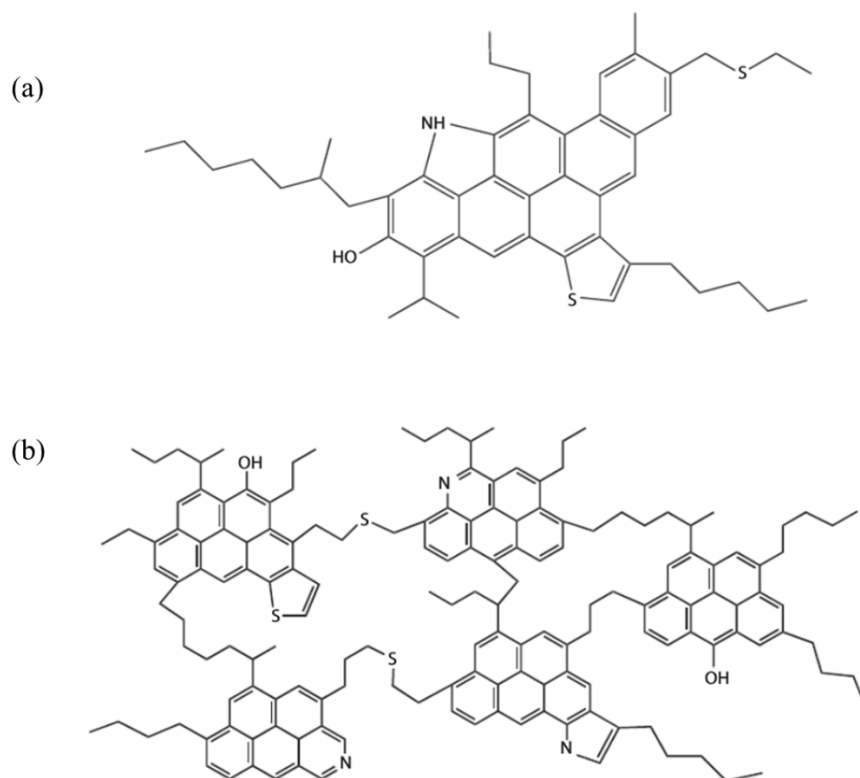
Figure 2.1 Example of asphaltene molecular structures: (a) island (continental) model; (b) archipelago model. (Kelland, 2014).

Asphaltenes self-associate into nano-aggregates with a broad size distribution. Numerous techniques have been employed to measure their molecular weights including isothermal titration calorimetry (Merino-Garcia *et al.* 2004), small angle x-ray scattering (Dickie and Yen, 1967; Eyssautier *et al.* 2012), ultracentrifugation (Dickie and Yen, 1967; Eyssautier *et al.* 2012), and vapour pressure osmometry (Dickie and Yen, 1967; Barrera *et al.* 2013). The nanoaggregates can range in size from dimers to structures of approximately 50,000 g/mol (Speight, 2007; Eyssautier *et al.* 2011; Yarranton *et al.* 2013). The average nanoaggregate molecular weights of asphaltenes extracted from the crude oil range from approximately 3000 to 10000 g/mol based on vapor

osmometry (Yarranton *et al.* 2013; Barrera *et al.* 2013). The diameter of the aggregates is in the order of 10 to 50 nm (Yarranton *et al.* 2013).

While the mechanism behind asphaltene self-association is still unresolved, two main concepts have been proposed: the colloidal approach and the macromolecular approach. The colloidal approach treats asphaltenes as colloids dispersed in the oil (Pfeiffer and Sal, 1939; Eyssautier *et al.* 2012). Asphaltenes form the core of each colloid and are stabilized by a layer of resins which prevents asphaltene-asphaltene interactions and keep the colloids dispersed in the oil. Upon mixing with a poor aliphatic solvent, the resin layer is removed and the asphaltenes start to aggregate and precipitate.

The macromolecular approach treats asphaltenes as macromolecular assemblies dissolved in the oil, analogous to polymers in a solution (Agrawala and Yarranton, 2001; Merino-Garcia *et al.* 2004). The nano-aggregates can be considered as assemblies of propagators or terminators. Propagator molecules contain multiple active sites that can connect to other molecules while terminators contain only one active site and are incapable of further association. Asphaltenes predominantly serve as propagators while resins are primarily terminators. The nano-aggregates of resins and asphaltenes are considered to be in thermodynamic equilibrium with the other components in the oil. In this case, asphaltene precipitation is a phase transition caused by changes in the equilibrium conditions. A phase transition is more consistent with the observed phase behavior; for example liquid heavy phase formation at higher temperatures (Zhang *et al.* 2003; Gray *et al.* 2004). Most asphaltene precipitation models are chemical equilibrium models and hence implicitly assume that the asphaltene nano-aggregates are dissolved rather than dispersed in the oil.

2.2 Asphaltene Precipitation

2.2.1 Asphaltene Precipitation Behavior

The nature of the precipitated asphaltenes depends on the conditions. For example, in a heavy oil diluted with *n*-pentane or higher carbon number *n*-alkanes at temperatures up to approximately 90°C, asphaltenes precipitate out of the oil as 0.5 μm diameter glassy particles (Maqbool *et al.* 2009). Above approximately 130°C, an asphaltene-rich phase "precipitates" as liquid droplets.

Between 90 and 130°C, the asphaltenes are in a glass/liquid transition (Johnston *et al.* 2017a; Duran *et al.* 2018). Figure 2.2 shows the morphology of the precipitated asphaltenes at two different temperatures.
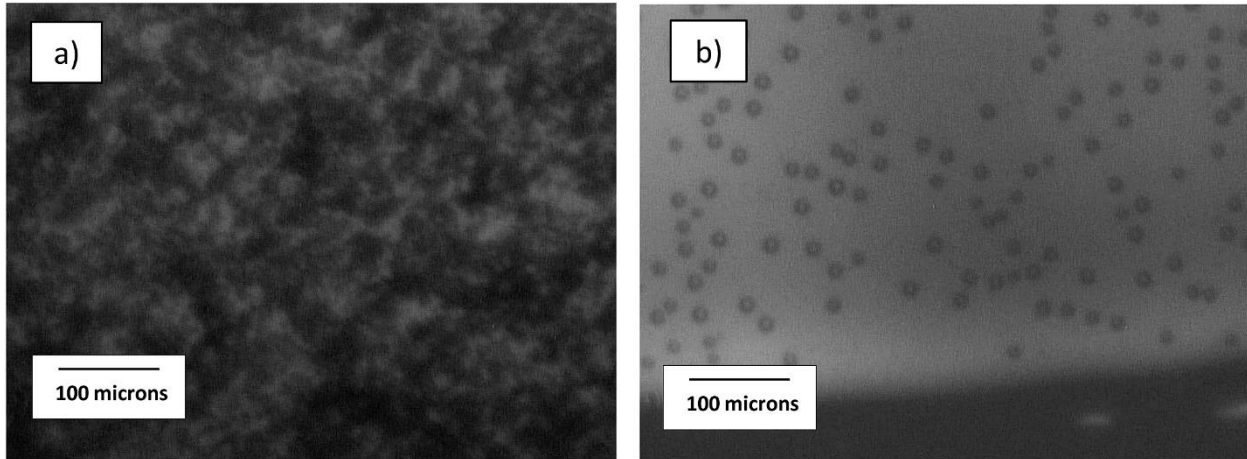
Figure 2.2 Asphaltenes precipitated from *n*-pentane diluted bitumen at: a) 23°C (glassy particles) and b) 165°C (liquid droplets) (Johnston *et al.*, 2017a)

Asphaltenes can precipitate due to changes in temperature, pressure, or composition. During live oil production from undersaturated reservoirs (reservoir pressure > bubble point pressure), depressurization can cause asphaltene precipitation, most commonly in highly undersaturated light to medium crude oils which barely solubilize the asphaltenes present in the oil. Depressurization reduces the density of the oil making it a poorer solvent for asphaltenes. The maximum amount of asphaltene precipitation occurs at the bubble point pressure (De Boer *et al.* 1995; Akbarzadeh *et al.* 2012). Any further decreases in pressure below the bubble point pressure causes solution gases to evolve. Since the solution gases are poor solvents for asphaltenes, the remaining oil becomes a better solvent for the asphaltenes and no further precipitation occurs. In theory, the oil could redissolve the asphaltenes but the kinetics of asphaltene redissolution are slow (Beck *et al.* 2005) and redissolution may not occur in practice.

Asphaltene precipitation can also occur in heavy oil *in situ* and surface processes when the oil is diluted with an incompatible solvent. Similarly, asphaltene precipitation can occur in crude oil dilution or blending processes for pipeline transport or in refineries. In the laboratory, *n*-alkanes

such as *n*-pentane or *n*-heptane are commonly used to initiate asphaltene precipitation (Hu and Guo, 2001; Akbarzadeh *et al.* 2005; Wiehe *et al.* 2005; Maqbool *et al.* 2009; Duran *et al.* 2019).

In solvent diluted heavy oil, the onset condition is defined as the mass fraction of solvent where precipitation is first detected. The amount of precipitated asphaltenes is typically defined as a yield (mass of precipitate divided by mass of feed oil). The asphaltene yield increases with increasing solvent content above the onset but tends to reach a plateau at higher solvent contents. The asphaltenes that precipitate first are the densest, highest molecular weight, most polar, and most heteroatomic fraction of the asphaltenes (Speight, 2007). The amount of precipitate at a given solvent content depends on the type of solvent, temperature, and pressure. In *n*-alkanes, the asphaltene yield decreases as the carbon number of the precipitant increases from 3 to 10. Above carbon numbers of 10, the amount of precipitation slightly decreases (Hu and Guo, 2001; Wiehe *et al.* 2005). Asphaltene onsets and yields are only slightly sensitive to temperature. In general, asphaltenes become more soluble (higher onsets and lower yields) as temperature increases up to approximately 100°C (Hu and Guo, 2001; Akbarzadeh *et al.* 2005) and then become less soluble at higher temperatures (Johnston *et al.* 2017a). Asphaltenes become more soluble at higher pressures (Johnston *et al.* 2017a; Mancilla-Polanco *et al.* 2018; Perez Claro *et al.* 2019).

Asphaltene precipitation has also been found to vary as a function of contact time with solvents (Maqbool *et al.* 2009; Duran *et al.* 2019). As contact times increase, asphaltene yields tend to increase and the onset of precipitation to decrease to a lower precipitant content (Maqbool *et al.* 2009). In an anaerobic environment, asphaltene onsets and yields approach an equilibrium value after approximately 150 hours of contact time (Duran *et al.* 2019). At lower precipitant contents (<75wt% *n*-heptane), the asphaltene yields increased slowly and approached its equilibrium value within 50-150 hours, while equilibrium asphaltene yields were reached in a shorter time at higher precipitant contents (Duran *et al.* 2019). In an aerobic (oxygen-rich) environment, asphaltene yields appear to increase indefinitely suggesting an oxidation effect.

2.2.2 Asphaltene Precipitation Models
Since asphaltene precipitation is a precursor to asphaltene deposition, a precipitation model is a required as part of or in complement to a deposition model. This thesis focuses only on deposition

but a brief review of asphaltene precipitation modeling is provided below. Asphaltene precipitation has been successfully modeled using a thermodynamic equilibrium approach based on equations of state or regular solution theory. These models treat asphaltene precipitation as a liquid-liquid equilibrium where components partition between an asphaltene-rich liquid phase and a solvent-rich liquid phase.

Cubic equations of states (EoS) have been applied to study asphaltene precipitation behaviour in n-alkane diluted heavy oils (Castellanos-Díaz *et al.* 2011; Agrawal *et al.* 2012; Johnston *et al.* 2017b). Modelling approaches employing Cubic EoS are widely used because they are easy to implement into commercial simulators and have relatively fast computation times. This type of model has been able to match saturation pressures and asphaltene onsets but tends to underpredict asphaltene yields at higher solvent dilutions. Johnston *et al.* used compositionally dependent solvent/asphaltene binary interaction parameters to improve the prediction of asphaltene yields in n-pentane diluted bitumen. However, the model is unable to accurately capture phase compositions at temperatures above 100°C and its tuning parameters are difficult to generalize for other solvents.

The cubic plus association (CPA) EoS has been applied to characterize asphaltene precipitation in live oils accounting for pressure, temperature, and composition effects, and n-alkane diluted bitumens (Li and Firoozabadi, 2010a; Li and Firoozabadi, 2010b; Zhang *et al.* 2019). Compared to the cubic equations of state, this model introduces additional terms to describe the self-association between asphaltene molecules and the cross-association between asphaltenes and maltenes or asphaltenes and n-alkane solvents. Recently, Zhang *et al.* used the CPA equation of state to model the phase behaviour of n-alkane diluted bitumen. The model captured asphaltene yields and phase boundary data but lost accuracy near and above the critical temperature of the solvents.

The perturbed chain statistical associating fluid theory (PC-SAFT) EoS was developed to understand the phase behaviour of complex associating fluids and has also effectively captured asphaltene precipitation behavior (Gonzalez *et al.* 2004; Gonzalez *et al.* 2007; Panuganti *et al.* 2011; Punnapala and Vargas, 2013; Zúniga-Hinojosa *et al.* 2014). One of the main assumptions of this model is that asphaltene phase behaviour is controlled by London dispersion forces and polar

interactions play a negligible role. The model has been predominantly applied to live oils where depressurization drives asphaltene precipitation, but has recently been applied to *n*-alkane diluted heavy oils and bitumens. While this model has been able to accurately predict the asphaltene precipitation process, it is computationally intensive due to the number of input parameters required for the model.

The modified regular solution model is an activity coefficient based model that includes the enthalpy from a regular solution and the entropy of mixing molecules of different sizes. This model has been successful in predicting the onset and amount of asphaltene precipitation from *n*-alkane diluted heavy oils (Alboudwarej *et al.* 2003; Akbarzadeh *et al.* 2005). The original version of model assumed that solvent cannot partition to the asphaltene-rich heavy phase. However, the model was recently updated to include partitioning of all components between the liquid phases (Ramos-Pallares and Yarranton, 2020). The model is straightforward to apply but is not applicable to vapour-liquid equilibrium and has not been rigorously tested for asphaltene precipitation from a live oil depressurization.

2.3 Asphaltene Aggregation

When asphaltenes separate from the oil as part of a liquid heavy phase, the droplets will tend to coalesce into a continuous liquid. To the author's knowledge, this coalescence process has not been studied or linked to asphaltene deposition. In contrast, there is considerable research on the aggregation of precipitated glassy asphaltene particles.

2.3.1 Asphaltene Aggregation Behavior in the Glassy Particle Regime

When asphaltenes precipitate as glassy particles, they form primary particles with diameters ranging from 0.5-5 µm (Ferworn *et al.* 1993; Rastegari *et al.* 2004; Calles *et al.* 2008; Hoepfner *et al.* 2013b; Seifried *et al.* 2013a; Duran *et al.* 2018). These primary particles almost instantaneously aggregate into larger porous structures that may reach hundreds of micrometers in diameter (Rastegari *et al.* 2004; Calles *et al.* 2008; Hoepfner *et al.* 2013b; Seifried *et al.* 2013a; Duran *et al.* 2018; Soleimani-Khormakala *et al.* 2019). Duran *et al*. 2018 demonstrated that the aggregates are fused structures that can be broken under sufficient shear but do not reform. These aggregates are considered to be a product of a phase transition. They are two orders of magnitude larger than the

nano-aggregates formed by self-association. They may incorporate the nano-aggregates but are distinct from them.

Asphaltene aggregates are considered to be fractal structures; that is, their porosity and density scale with their diameter to the power of their fractal dimension. The diameter of an asphaltene aggregate is typically defined by its maximum diameter (Rastegari *et al.* 2004; Duran *et al.* 2018). Fractal dimensions can be applied in 1, 2, or 3 dimensions (Rahmani *et al.* 2005). For this thesis, only the three-dimensional (3D) fractal dimension is considered and for simplicity, it will just be referred to as the fractal dimension. For an aggregate, as the fractal dimension increases, its structure becomes more compact and three-dimensional in nature. For example, a fractal dimension of 2 corresponds to a planar or highly porous spherical structure while a fractal dimension of 3 corresponds to a Euclidean solid. Precipitated asphaltenes that form micrometer scale asphaltene aggregates have fractal dimension ranging from 1.6 to 2.8 (Rastegari *et al.* 2004; Rahmani *et al.* 2005; Duran *et al.* 2018). Figure 2.3 shows an example of aggregated asphaltenes in *n*-heptane diluted bitumen.
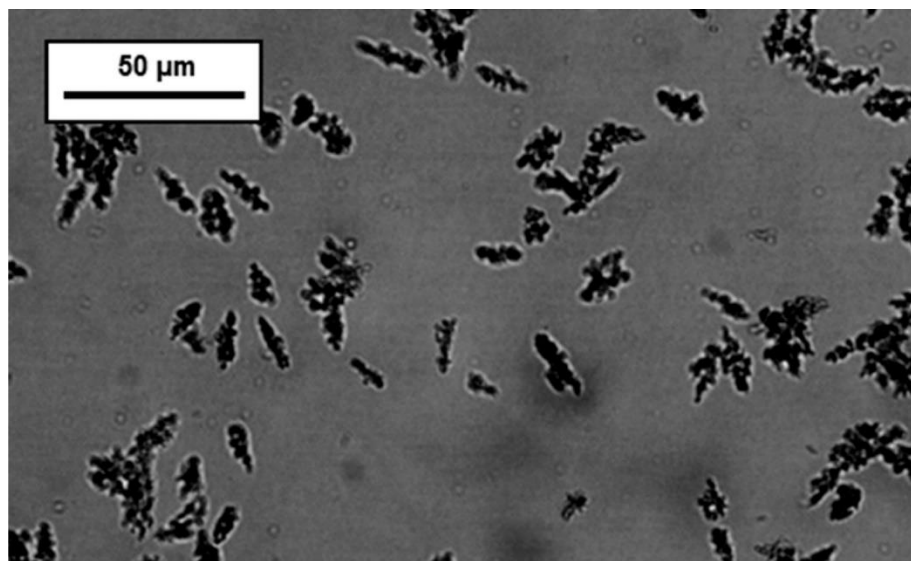
Figure 2.3 Asphaltene aggregates from *n*-heptane diluted bitumen (Duran *et al.*, 2018).

The size and fractal dimension of the aggregates depends on several factors including the type and amount of precipitate, the asphaltene content of the crude oil, and shear conditions. Size is discussed first. In general, asphaltene aggregates are larger in crude oils that have a higher

asphaltene concentration (Ferworn *et al.* 1993; Duran *et al.* 2018). The aggregates are also larger and have a wider size distribution when formed in a stronger precipitant (Calles *et al.* 2008; Seifried *et al.* 2013a). For example, the average asphaltene aggregate size in a crude oil residue diluted with *n*-alkanes increased progressively from *n*-heptane to *n*-hexane to *n*-pentane diluent at the same dilution ratio (Calles *et al.* 2008). The average steady-state size of the asphaltene aggregates also increases as the precipitant content increases above the onset of precipitation. Duran *et al.* (2018) reported asphaltene aggregates reaching a maximum size at 80 wt% *n*-heptane in two different bitumens, with any subsequent increases in solvent content resulting in a decrease in aggregate size. Similarly, the average size of the asphaltene aggregates reached a plateau as solvent content increased in a series of both light and heavy crude oils diluted with *n*-heptane (Ferworn *et al.* 1993). For asphaltene aggregates generated from heptol solutions and a crude oil residue, it was reported that the aggregate size continued to increase as the precipitant content increased (Rastegari *et al.* 2004; Calles *et al.* 2008).

The influence of mixing intensity (shear) and contact time between the precipitant and crude oil on the size of asphaltene aggregates is less clear. For example, Rastegari *et al.* (2004) observed aggregates becoming smaller at higher shear rates in heptol solutions. Some researchers reported that moderate increases in shear rate resulted in larger aggregates due to the increased number of collisions between asphaltene particles. Further increases in shear rate causes the size of asphaltene aggregates to decrease. At a constant shear rate, asphaltene aggregates in heptol grow to a maximum size before decreasing and eventually reaching a steady-state plateau where there is a balance between aggregation and breakage (Torkaman *et al.* 2018; Soleimani-Khormakala *et al.* 2019). Increasing the shear rate causes the asphaltene aggregates to reach their maximum size at a shorter contact time between the precipitant and crude oil.

Duran *et al.* (2018) observed that asphaltene aggregates in *n*-heptane diluted bitumen are only shear sensitive initially during their formation. An increase in shear rate causes a reduction in the initial aggregate size. Under a constant shear rate, there is little or no change to the size of the asphaltene aggregates over time at lower *n*-heptane contents while aggregates at higher *n*-heptane content can be shattered under sufficient shear. In addition, there is some evidence that precipitated

asphaltenes are only sticky for a few minutes after precipitation (Duran *et al.* 2018). Therefore, asphaltenes may have the ability to form aggregates only when they first precipitate.

The fractal dimension of asphaltene aggregates are also affected by the factors mentioned above but changes in the fractal dimension have been studied to a lesser extent. In general, asphaltene aggregates form lower porosity structures (higher fractal dimension) as the precipitant concentration increases (Hoepfner *et al.* 2013b; Duran *et al.* 2018). Duran *et al.* reported a maximum in the fractal dimension that corresponds to the precipitant content where the maximum aggregate size is reached. A decrease in fractal dimension was observed at higher precipitant content. Fractal dimensions were observed to increase with shear rate in heptol solutions (Rahmani *et al.* 2005; Soleimani-Khormakala *et al.* 2019), resulting in more compact asphaltene aggregates. In contrast, Duran *et al.* (2018) observed no change in the fractal dimension in whole oils as a consequence of shear.

2.3.2 Asphaltene Aggregation Modeling in the Glassy Particle Regime
Asphaltene aggregation occurs concurrently with precipitation and may play a role in the deposition process. Therefore, an aggregation model is required as part of or in complement to an asphaltene deposition model. A brief review of asphaltene aggregation modeling is provided below.

Asphaltene aggregation is commonly modeled using the population balance approach originally proposed by Smoluchowski (Rahmani *et al.* 2003; Rastegari *et al.* 2004; Torkaman *et al.* 2018; Soleimani-Khormakala *et al.* 2019). In these models, a dynamic equilibrium is assumed between asphaltene aggregation and breakage, which are controlled by shear and temperature of the environment. The distribution of the number of particles per aggregate is determined from the population balance. A size distribution is established for asphaltene aggregates based on the number of primary particles in the aggregate. To predict the size distribution of asphaltene aggregates as a function of time, most of the models require several assumptions leading to different fitting parameters specific to each system. As a result, the models are hard to generalize and are unique to that particular system.

Recall from Section 2.2.1 that asphaltene precipitation is a function of contact time with solvents. Therefore, the amount of precipitated asphaltenes available for aggregation also varies as a function of time. This effect has been neglected in most early aggregation models, where the amount of precipitated asphaltenes are simply based on the asphaltene yield at a fixed contact time (Rahmani *et al.* 2003; Rastegari *et al.* 2004; Torkaman *et al.* 2018; Soleimani-Khormakala *et al.* 2019). To account for this behaviour, Maqbool *et al.* (2011) allowed the concentration of "unstable" asphaltenes to vary over time and modeled the aggregation of asphaltene nanoaggregates to the micrometer scale. The model required only one fitting parameter and was able to match asphaltene yields and onset (appearance of 0.5 μm diameter glassy particles) over time. However, one limitation of this model is it can predict the yield or aggregate size distribution over time, but not both simultaneously. Recently, Duran *et al.* (2019) modified the model by Maqbool *et al.* to account for initial rapid asphaltene aggregation when they contact a precipitant and the eventual decrease in stickiness (ability for further aggregation) of asphaltene aggregates as time increases. The kinetics for both asphaltene precipitation and aggregation were captured by the model. The model successfully matched both the yield and aggregate size distribution over time.

2.4 Asphaltene Adhesion in the Glassy Particle Regime

In order to establish a deposit, asphaltenes particles (or droplets) must not only be transported to a surface of a pipe or vessel but also adhere to the deposition surface and to each other. To the author's knowledge, the adhesion of asphaltene droplets from a liquid heavy phase onto a surface has not been studied but substantial research has been done on the adhesion process in the glassy particle regime. Asphaltene adhesion has been examined in the laboratory with various apparatus including the atomic force microscope (AFM), surface force apparatus (SFA), quartz crystal microbalance (QCM), X-ray photoelectron spectroscopy tests, and UV-vis spectrophotometer. A detailed description of the above methods are provided elsewhere (Ducker *et al.* 1992; Alboudwarej *et al.* 2005; Xie and Karan, 2005; Israelachvili *et al.* 2010).

2.4.1 Asphaltene Adhesion Behaviour in the Glassy Particle Regime

Asphaltene adhesion is strongly influenced by the surrounding fluid. In a polar solvent such as water, the interactions between asphaltenes and silica are repulsive at longer distances and become

attractive (adhesive) as they approach each other. At very short distances, a strong steric repulsion exists between the two surfaces. As adsorption time increases however, the adhesion force between asphaltenes and silica decrease, indicating asphaltene molecules are capable of rearranging themselves at the asphaltene-silica interface. The asphaltene-silica interactions become more attractive when the salinity of the aqueous solution is increased (Abraham *et al.* 2002). This observation suggests the repulsive forces that built over time in polar solvents are electrostatic in nature. A similar trend was reported for interactions between asphaltene films (Liu *et al.* 2006).

Non-polar organic solvents also affect the adhesion process based on their compatibility with asphaltenes (Wang *et al.* 2010; Natarajan *et al.* 2011; Natarajan *et al.* 2014; Zhang *et al.* 2016). In a solvent like toluene in which the asphaltenes are fully miscible, asphaltene films repel each other at long distances but experience a weak attraction to each other after contact during the initial separation. The attraction likely corresponds to asphaltene molecules interlocking with each other during their initial encounter. Over time, this adhesion force disappears and the repulsive force extends to longer distances as the asphaltenes become solvated and swell in toluene. The repulsion arises due to steric effects.

On the other hand, in a solvent like *n*-heptane in which the asphaltenes are only partially miscible, the asphaltene films exhibit repulsion at long distances but a strong attraction during separation. As the ratio of *n*-heptane in heptol solutions increases, the adhesion force between asphaltene films also increases (Wang *et al.* 2010; Natarajan *et al.* 2011; Zhang *et al.* 2016). The attraction between asphaltene films can be characterized based on van der Waals forces. The adhesion force gradually weakens over time, suggesting that asphaltene molecules on the surface reorient themselves such that steric effects increase between the approaching asphaltene films. Compared to the asphaltene films in toluene, asphaltenes in *n*-heptane are less swollen and more rigid. In general, as the surrounding environment changes from miscible to partially miscible conditions, the interactions between asphaltene films switch from repulsion to adhesion.

The amount of asphaltene adsorption in miscible conditions also varies depending on the type of metal surface used. Asphaltenes preferentially adsorb onto the following metals in a decreasing order: gold > stainless steel > iron > aluminum (Alboudwarej *et al.* 2005; Xie and Karan, 2005).

Multiple factors play a role in the affinity of asphaltenes towards different metals including the properties of the metal, the number of adsorption sites available, and the chemical structure of asphaltene molecules. For example, X-ray photoelectron spectroscopy tests have found that nitrogen, oxygen, and sulfur heteroatoms on asphaltene molecules play a major role in the adsorption process. Specifically, the carboxylic, thiophenic, sulfide, pyridinic, and pyrrolic chemical functional groups are involved.

As the concentration of asphaltenes increases, the amount of asphaltene adsorption onto metal and mica surfaces increases (Xie and Karan, 2005; Rudrake *et al.* 2009; Natarajan *et al.* 2014). A larger asphaltene concentration also results in a higher initial adsorption rate that is diffusion-controlled. In addition, the time required to reach equilibrium conditions decreases at higher asphaltene concentrations. The overall amount of asphaltene adsorption also increases as the surrounding environment becomes a poorer solvent for asphaltenes (increasing ratio of *n*-alkanes in the mixture).

Alboudwarej *et al*. (2005) found that asphaltene adsorption on metals appears to follow Langmuir (Type I) isotherms. The asphaltenes occupy the available surface area for adsorption as a monolayer. However, multilayer asphaltene adsorption has been observed in QCM experiments at later times (Xie and Karan, 2005; Abudu and Goual, 2009; Zahabi *et al.* 2012). These experiments differ from the previous film studies where a pure solvent was placed next to an already adsorbed asphaltene monolayer film. In this case, asphaltene nanoaggregates were present in the solvent. These aggregates tend to adsorb as multilayers that are loosely packed and have solvent contents ranging from 85-90% (Abudu and Goual, 2009; Zahabi *et al.* 2012). Since asphaltenes tend to adsorb as monolayers (or perhaps multilayers) on metal surfaces, subsequent adhesion of glassy asphaltene particles likely consists of adhesion of asphaltene particles to asphaltene coated surfaces.

2.4.2 Asphaltene Adhesion Modeling

Asphaltene adhesion is the first step in the deposition process. Hence, an adhesion model is required as part of or in complement to an asphaltene deposition model. Two approaches to modeling asphaltene adhesion are reviewed and discussed below.

Asphaltene adsorption onto QCM crystals has been modeled with the simplified Ward-Tordai equation (Xie and Karan, 2005; Abudu and Goual, 2009; Zahabi and Gray, 2012). In this model, the adsorption process is assumed to be irreversible and diffusion-controlled. Specifically, the amount of asphaltene adsorption in toluene solutions is expected to be proportional to the bulk concentration of asphaltenes, the square root of diffusivity, and the square root of time. At early times, the adhesion rate determined from QCM measurements does indeed vary linearly with $\sqrt{t}$, confirming the initial process is diffusion-controlled. However, this relationship breaks down at later times. In addition, the apparent diffusion coefficient of asphaltenes in toluene solutions at early times and the estimated diameter of the asphaltene particles from this approach are inconsistent with literature values. Zahabi and Gray (2012) concluded that diffusivity and asphaltene size estimates from QCM measurements are unreliable.

Another approach is to treat the adhesion process as a first-order chemical reaction at the deposition surface (Watkinson, 1968; Asomaning, 1997; Epstein, 1997; Ebert and Panchal, 1997; Yeap *et al.* 2005; Watkinson, 2007; Jamialahmadi *et al.* 2009). The kinetic rate constant for adhesion is assumed to be proportional to the Arrhenius equation. This assumption means that the adsorption rate grows exponentially with an increase in the surface temperature. In order for asphaltenes to adsorb onto a surface, they must overcome an activation energy barrier, which is used as a fitting parameter in the models. The energy barrier may arise from van der Waals forces or electrostatic double layer forces. This model has been commonly used to describe the initial asphaltene adhesion process in heat exchangers at temperatures where asphaltenes are transitioning to the liquid phase or are fully liquid. It has not been rigorously tested at temperatures where asphaltenes precipitate as glassy particles. While the model has been able to successfully capture the early-time temperature dependency of the adhesion process, the activation energy is specific to each system. Therefore, the approach is hard to generalize and is unique to that particular system.

2.5 Asphaltene Deposition in the Glassy Particle Regime

Asphaltene deposition in the glassy particle regime involves the adhesion and accumulation of asphaltene particles at the surface of a reservoir, wellbore, pipe, or vessel. This thesis focuses on

asphaltene deposition in open flow (wellbores, pipelines, facilities). First, methods to measure asphaltene deposition are reviewed, then the observed deposition behavior, and finally the modeling of asphaltene deposition including the two main asphaltene deposition models from the literature.

2.5.1 Asphaltene Deposition Measurement

Asphaltene deposition in open flow has been studied in the laboratory with numerous techniques including coupon deposition tests, capillary tests, flow loop apparatuses, Taylor-Couette cells, confocal laser-scanning microscopy, electron microscopy, and packed bed columns. Coupon deposition tests have been used to assess different chemicals additives in their abilities to inhibit asphaltene deposition (Fouchard and Carmichael, 2014; Bae *et al.* 2016). In this method, a stainless-steel coupon is submerged vertically into crude oil along with a magnetic stirrer to ensure the solution is well mixed when a solvent is added to induce asphaltene precipitation. In some tests, a chemical additive is also added to the crude oil to test its ability to prevent asphaltene buildup. After the metal coupon undergoes a soak period, it is removed from the mixture and allowed to dry. The amount of asphaltene deposition is then measured gravimetrically from the change in mass of the coupon. Coupon deposition tests show the propensity of asphaltenes to deposit onto metal surfaces, but most tests are focused on the effectiveness of a certain chemical asphaltene inhibitor and do not attempt to investigate asphaltene deposition mechanisms.

In a capillary test, asphaltenes are precipitated out of solution by mixing the crude oil and an *n*-alkane precipitant together. The mixture then travels through a capillary tube (test section) where asphaltenes may adhere to the surface of the pipe and form a deposit. The deposition rate is based on the change in pressure drop across the capillary tube. A higher pressure drop corresponds to a larger deposit. Capillary tests are an effective method to investigate asphaltene deposition on the capillary walls due to their sensitivity in detecting changes in pressure drop (Broseta *et al.* 2000; Wang *et al.* 2004; Nabzar and Aguilera, 2008). While capillary flow experiments can provide insight into asphaltene deposition mechanisms, most studies were restricted to the laminar flow regime and could not simulate turbulent flow which may be present in wellbores and pipelines.

Asphaltene deposition under turbulent conditions has been studied using flow loop apparatuses (Ghahfarokhi *et al.* 2017). The deposition rate is again based on the change in pressure drop as deposition occurs. A large volume of fluid sample is required for flow loop apparatuses to generate the high flow rates necessary for turbulent flow. The fluid sample must be recirculated into the system via a high-capacity pump, which may break up existing asphaltene aggregates, thus changing the aggregation process, which can play a role in the deposition process (Eskin *et al.* 2011). Therefore, flow loop apparatuses may not be a suitable method to examine asphaltene deposition in turbulent flow.

Techniques based on pressure drop do not identify where the deposit occurs or how large the deposit is. However, imaging techniques such as confocal laser-scanning microscopy (Seifried *et al.* 2013b) and electron microscopy (Hoepfner *et al.* 2013a) have been used to visualize the location of the asphaltene deposits in capillary tests. In confocal laser-scanning microscopy, a laser beam travels through an objective lens and is directed at a small section of a glass capillary tube after a deposition experiment. The laser beam scans the capillary tube section by section and the transmitted light is then detected by a pinhole aperture and photomultiplier tube. The pinhole aperture blocks out of focus light and the photomultiplier tube amplifies light from the sample to construct a high-resolution image. Similarly, images from an electron microscope are generated on a point by point basis. First, an electromagnetic lens is used to focus a beam of primary electrons onto the cross-section of a metal capillary tube with asphaltene deposits. As the primary electrons excite the atoms in the deposit and capillary tube, secondary electrons are emitted and are captured by a secondary electron detector, which translates the signal to create an image.

Another method is the Taylor-Couette cell (Eskin *et al.* 2011; Akabarzadeh *et al.* 2012; Eskin *et al.* 2012). A Taylor-Couette cell consists of two concentric cylinders. The inner cylinder rotates at an adjustable speed to simulate different turbulent intensities while the outer cylinder is fixed to allow asphaltene deposits to accumulate on its inner wall. The annular space between the two cylinders is filled with a live oil sample at a pressure above the asphaltene onset pressure. Asphaltenes are then generated via pressure drop induced precipitation from the fluid sample as the inner cylinder rotates to generate a shear force for fluid flow. The apparatus can be configured to operate as both a batch process and continuous flow-through process. At the end of each

experiment, the remaining oil in the apparatus is displaced with helium and the deposit (asphaltenes + trapped oil) is dissolved with a dichloromethane wash. The deposit is recovered after evaporating off the solvent and its mass and composition of the deposit can be obtained using standard techniques. It has been shown that Couette cells are able to simulate the asphaltene deposition conditions in a flowing pipe even though the flow pattern is circular rather than axial (Eskin *et al.* 2011). However, the Couette cell cannot be used to analyze the location of the deposits.

Asphaltene deposition has also been examined in a packed bed (Vilas Bôas Fávero *et al.* 2016; Kuang *et al.* 2018). The packed bed column consists of a vertical glass or stainless-steel column packed with stainless steel spheres. Asphaltenes are first generated via solvent induced precipitation and the resulting mixture is pumped upwards through the packed bed column. Kuang *et al.* (2018) modularized the original apparatus developed by Vilas Bôas Fávero *et al.* (2016) by splitting the vertical column into multiple sections, thus allowing the location of the deposit to be analyzed. At the end of the experiment, the apparatus is first washed with cyclohexane to remove the residual fluid and trapped oil in the asphaltene deposits. Next, a toluene wash removes the remaining asphaltenes on the metal spheres and the mass of asphaltene deposits is measured after evaporating off the toluene. Due to the increased surface area created by the metal spheres, the packed bed column has been used successfully to evaluate different chemical asphaltene inhibitors. However, it may only give limited insights into asphaltene deposition mechanisms as its tortuous flow path is not representative of open pipe flow in wellbores and pipelines.

2.5.2 Asphaltene Deposition Behavior in the Glassy Particle Regime

The amount of asphaltene deposition was inferred in early capillary flow experiments from pressure drop measurements and it was assumed that the deposit was a uniform layer of equal thickness (Broseta *et al.* 2000; Wang *et al.* 2004). Later, imaging techniques showed the majority of asphaltene deposits are concentrated near the inlet of the capillary tube (Seifried *et al.* 2013b; Hoepfner *et al.* 2013a). This observation was also confirmed by monitoring the pressure drop profiles across capillaries of different lengths (Hoepfner *et al.* 2013a). Both capillaries showed a similar pressure drop profile indicating most of the deposition occurs at the entrance of the capillary tube. In addition, Kuang *et al.* (2018) confirmed the location of the deposits

gravimetrically by cutting the capillary tube into equal segments and subtracting the original mass of the tube. The deposit mass was found to be concentrated in the first and last sections of the capillary tube.

It has been inferred that the majority of asphaltene deposits consist of submicron asphaltene aggregates (Eskin *et al.* 2011; Eskin *et al.* 2012; Hoepfner *et al.* 2013a; Bemani *et al.* 2019). Eskin *et al.* performed a force balance calculation acting on a deposited asphaltene particle at the wall, which indicated that asphaltene aggregates up to several microns in size had the potential to deposit. Eskin *et al.* also developed a numerical model for asphaltene deposition that is presented in detail later in section 2.5.4. Briefly, the critical particle size was used as a fitting parameter, and the modeling results showed the asphaltene aggregates were two orders of magnitude smaller than predicted in the force balance calculations. In addition, it was found that asphaltene particles that were aged and grew beyond 250 nm did not deposit in capillary tests (Hoepfner *et al.* 2013a; Bemani *et al.* 2019).

Asphaltene deposition has been shown to increase in stronger precipitants and as the amount of precipitant increases. For example, as the concentration of *n*-heptane increases, the rate of deposition also increases and is detected faster (Hoepfner *et al.* 2013a; Seifried *et al.* 2013b; Vilas Bôas Fávero *et al.* 2016; Li *et al.* 2017). When the carbon number of an *n*-alkane precipitant increases from 5 to 8, the precipitated asphaltenes form a detectable deposit sooner (Chaisoontornyotin *et al.* 2016; Kuang *et al.* 2018). The decrease in time to deposition corresponds to the increase in the amount of asphaltene precipitation as the *n*-alkane carbon number decreases, indicating the importance of asphaltene solubility on the deposition process (Hoepfner *et al.* 2013a; Chaisoontornyotin *et al.* 2016).

Fluid dynamics also plays an important role in the deposition process. As fluid flows through a pipe, shear stress acts on the pipe wall. In the case of a developing asphaltene deposit layer, the shear stress acts on the deposit interface. Shear stress increases with increasing flow velocity and fluid viscosity. When the shear stress is below a critical value (pseudo-yield stress), the deposition is controlled by the ability of asphaltene particles to transport themselves to the wall (Nabzar and Aguilera, 2008; Eskin *et al.* 2011; Eskin *et al.* 2012); that is, there is no shear removal of the

deposits. In this regime, it is expected that asphaltene deposition increases at higher flow rates, which has been observed in capillary flow experiments (Seifried *et al.* 2013b; Vilas Bôas Fávero *et al.* 2016; Li *et al.* 2017). Above the pseudo-yield stress, an increase in flow rate leads to a plateau or decrease in the amount of asphaltene deposition because the deposit is sheared off as it forms (Eskin *et al.* 2011; Eskin *et al.* 2012; Ghahfarokhi *et al.* 2017).

Asphaltene deposition may also be affected by temperature but the effect of temperature on the deposition process has only been considered in a few recent studies. Bemani *et al.* (2019) investigated asphaltene deposition in a capillary tube at temperatures up to 70°C and found that a higher temperature accelerated the deposition process. Kuang *et al.* (2018) studied the deposition of different two crudes oil at temperatures ranging from 20 to 120°C in a packed bed apparatus. In one of the oils, the amount of deposition increased as the temperature increased, whereas the opposite occurred for the other oil. Their results suggested competing factors are at play in the deposition process. They concluded that a higher temperature results in an increased mass transfer rate of asphaltenes to the deposition surface. At the same time, a higher temperature also increases the solubility of the asphaltenes in the oil, causing less precipitation and reducing the amount of asphaltenes available for deposition. In addition, at temperatures above 100°C, the asphaltene-rich phase may become a liquid. Deposition from a dispersed liquid likely differs significantly from deposition of dispersed particles but this difference was not considered in the study.

2.5.3 Fundamentals of Deposition Modeling

Asphaltene deposition is a multi-step process including asphaltene precipitation into primary particles, particle aggregation, transport of particles to the pipe wall, adhesion of particles to the pipe surface, and erosion of the deposit due to shear forces. Each step is discussed below.

Asphaltene Precipitation:

In most deposition models, the equilibrium condition for asphaltene precipitation is predicted using an equation of state approach. Since deposition occurs in shorter times than required for equilibrium, the kinetics of precipitation are accounted for using an exponential relationship with time and a kinetic rate constant that is proportional to the insoluble asphaltene concentration. The precipitated asphaltene particles are usually assumed to have a uniform primary particle size.

Particle Aggregation:

Aggregation is included in the models through a kinetic term or a population balance based kinetic model. These approaches will be presented in the models shown later.

Transport:

Fluid flow through wellbores/pipelines is typically in a turbulent flow regime (Eskin *et al.* 2011; Kurup *et al.* 2011; Kurup *et al.* 2012). The flow in the core of the pipe is turbulent but there is a laminar sublayer near the wall and in between the two regions, a buffer layer that shares characteristics of both the laminar and turbulent boundary layers. The different flow zones are shown in Figure 2.4 where u is the fluid velocity, τ_w is the shear stress at the wall, y is the distance from the wall, and δ_i is the thickness of the ith layer (*e.g.* $i = $ t for turbulent layer). The no-slip condition applies at the wall; that is, the fluid velocity is zero at the wall.
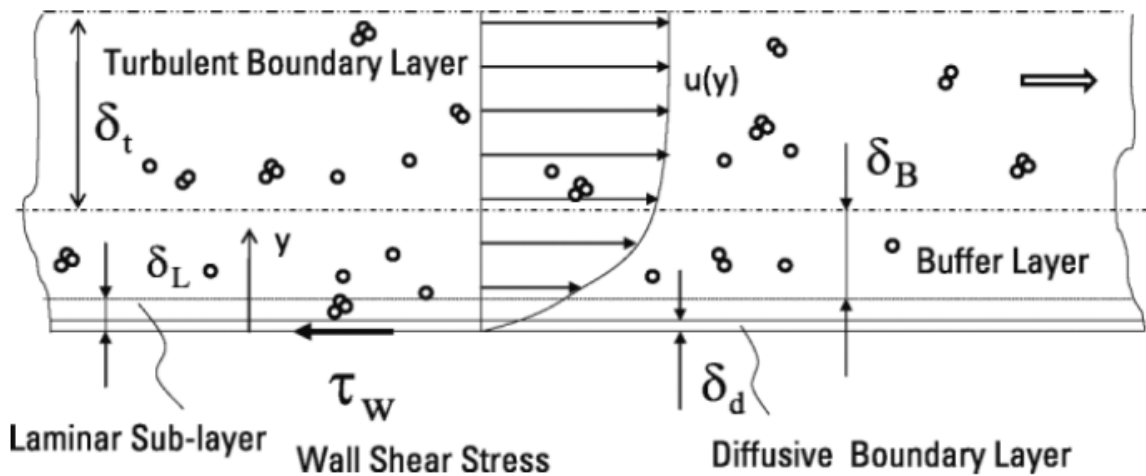
Figure 2.4 Boundary layer structure diagram. Taken from Eskin *et al*. 2011.

Asphaltene particles are transported along the pipe by advection while transport to the wall is orthogonal to the advection and is governed by diffusion or turbophoresis depending on the particle's size and relaxation time (Guha, 2008). Diffusion is the net movement of small particles along a concentration gradient due to Brownian motion and is described by Fick's law of diffusion:

$$J = -(D_{Br} + D_{turb})\frac{dC}{dy} \tag{2.1}$$

where J is the mass flux, D_{Br} is the Brownian diffusivity, D_{turb} is the turbulent diffusivity and $\frac{dC}{dy}$ is the particle concentration gradient. Turbophoresis is the transport of particles towards the wall that occurs when the turbulence decreases near the pipe wall causing a velocity slip between the particle velocity and fluid velocity which propels particles to the wall due to inertia. A particle's relaxation time is related to its inertia and is the time it takes for the particle to reach the velocity of the fluid it resides in. An increase in particle size equates to higher inertia and a larger relaxation time. When the particles are small and the relaxation time is small, they can effectively follow the fluid streamlines. As they get bigger, sudden changes in the fluid velocity may cause the particles to divert from the fluid streamlines and collide with the pipe wall causing deposition.

Between the laminar sub-layer and turbulent boundary layers, turbulent diffusion and turbophoresis may propel asphaltene particles towards the wall. Immediately adjacent to the wall within the diffusive boundary layer, Brownian motion is solely responsible in moving submicron asphaltene particles to the wall (Eskin *et al.* 2011). As particles get bigger in size, the role of diffusion as the dominant transport mechanism to the wall diminishes and is overtaken by turbophoresis. Turbophoresis starts to affect deposition when particles sizes exceed 1 μm (Guha, 2008).

Adhesion:

Once an asphaltene particle arrives at the wall, it has the potential to adhere to the wall and form a deposit. Adhesion is included in the models through a "sticking probability" term. The sticking probability is defined using a particle-wall interaction efficiency constant, kinetic rate constant, or estimated from the ratio of the adhesion force to drag force. In most models adhesion is assumed to be invariant over time. However, a recent study by Duran *et al.* (2018) showed that precipitated asphaltenes are only sticky for a few minutes after precipitation. Therefore, asphaltenes may have the ability to form deposits only near where they precipitate. A time dependence in the adhesion term would be required to model this effect.

Erosion:

Even after a deposit is formed, it may be eroded under sufficient shear. The amount of erosion from the deposit layer depends on many factors, including the adhesion force, the magnitude of

shear stress acting on the deposit, the thickness and porosity of the deposit, and the particle size distribution within the deposit (Eskin *et al.* 2011). Several semi-empirical models have been developed to capture asphaltene deposition mechanisms accounting for asphaltene floc size and concentration, shear conditions, fluid properties, and surface properties.

To date, the most comprehensive models include the deposition model created by Eskin *et al.* (2011) and the ADEPT model developed by Vargas *et al.* (2010). Both models apply only to particle deposition (not liquid phase deposition) and are discussed in more detail below.

2.5.4 Eskin *et al*. Asphaltene Deposition Model

The deposition model developed by Eskin and coworkers was developed from Couette cell experiments where fluid flow was in the turbulent regime. They placed a significant emphasis on capturing the asphaltene growth and size distribution mechanism and the mechanism of asphaltene transport to the wall (Eskin *et al.* 2011). They included a shear removal term to consider the reduction in deposition rate when there is an increase in shear stress at the wall. Their model can also be coupled with a precipitation module that uses a cubic equation of state to predict the amount of asphaltene precipitation as a function of pressure (Akbarzadeh *et al.* 2012).

Particle Aggregation:

The particle size distribution is split into *im* discrete fractions where the average particle diameter (*d*) in a fraction is double that of the previous fraction (i.e. $d_i = 2d_{i-1}$). The evolution of the particle size distribution as they grow in size is then calculated as follows:

$$\frac{dN_1}{dt} = \left(\frac{dN_1}{dt}\right)_{batch} + \frac{Q}{W}(N_{01} - N_1) \tag{2.2}$$

$$\frac{dN_i}{dt} = \left(\frac{dN_i}{dt}\right)_{batch} + \frac{Q}{W}N_i \qquad i = 2, \ldots, im \tag{2.3}$$

where N_i is the concentration of particles in the ith fraction by number (i =1 for the first fraction), N_{01} is the initial number concentration of particles in the first fraction at the onset of precipitation, Q is the volumetric flow rate, and W is the volume of the Couette cell. The change in concentration per unit time by number for a batch system is expressed as:

$$\left(\frac{dN_i}{dt}\right)_{batch} = N_{i-1}\sum_{j=1}^{i-2} 2^{j-i+1}\alpha_{i-1,j}\beta_{i-1,j}\,N_j + \frac{1}{2}\alpha_{i-1,i-1}\beta_{i-1,i-1}N_{i-1}^2 -$$

$$N_i\sum_{j=1}^{i-1} 2^{i-j}\alpha_{i,j}\beta_{i,j}\,N_j - N_i\sum_{j=1}^{im-1}\alpha_{i,j}\beta_{i,j}\,N_j - S_iN_i + \sum_{j=i+1}^{im}\Gamma_{i,j}S_jN_j \quad i,j = 1,\dots,im \quad (2.4)$$

where $\alpha_{i,j}$ is the collision efficiency of an ith size particle in with another j^{th} size particle, $\beta_{i,j}$ is the collision frequency function of an ith size particle in with another j^{th} size particle, S_i is the shattering rate of the ith size particle, and $\Gamma_{i,j}$ is the breakage distribution function that specifies the number of ith size particles that are formed when a jth size particle shatters.

The collision efficiency was assumed to be a constant and the same for all particle sizes. The collision frequency function is calculated as

$$\beta_{i,j} = \beta_{i,j}^{Br} + \beta_{i,j}^{turb} \tag{2.5}$$

$$\beta_{i,j}^{Br} = \frac{2}{3}\frac{k_BT_f}{\mu}\frac{(d_i+d_j)^2}{d_id_j} \tag{2.6}$$

where $\beta_{i,j}^{Br}$ is the collision frequency function from Brownian motion, $\beta_{i,j}^{turb}$ is the collision frequency function from turbulent diffusion, k_B is the Boltzmann constant, T_f is the temperature of the fluid, μ is the viscosity of the fluid, d_i is the diameter of an ith size particle, and d_j is the diameter of a jth size particle.

Based on numerical simulations that show the majority of asphaltene particles are submicron particles, the model assumes that asphaltene aggregation is controlled by Brownian motion and the turbulent collision frequency function in Eq. 2.5 can be neglected. The model also assumes that submicron particles cannot be shattered under turbulent flow. Hence, the shattering and breakage terms in the particle size distribution equation can be neglected. The only fitting parameter for this part of the model is the collision efficiency, α.

Particle Deposition (Transport, Adhesion, and Erosion):

The asphaltene deposition rate is given by

$$q_A = k_{sr}q_\Sigma \tag{2.7}$$

where q_A is the corrected deposition mass flux, q_Σ is the total deposition mass flux, and k_{sr} is an empirical equation accounting for the shear removal of the deposits. The total deposition mass flux can be further broken down into the following components:

$$q_\Sigma = \gamma \sum_{i=1}^{i=i_{cr}} m_i N_i \left[\frac{v_{dBi}}{2} + \frac{v_{dti}}{2} + v_{dtbi} \right] \tag{2.8}$$

where,

$$v_{dBi} = \left(\frac{2k_b T_f}{\pi m(d_i)} \right)^{\frac{1}{2}} \tag{2.9}$$

$$v_{dti} = \sqrt{\frac{2}{\pi}} \sqrt{\overline{V_y'^2 \left(\frac{d_i}{2} \right)}} \tag{2.10}$$

and where γ is the particle-wall interaction efficiency, m_i is the total mass of the asphaltene particles in i^{th} fraction, i_{cr} is the size fraction number that corresponds to the critical particle diameter d_{cr}, v_{dBi} is the most probable fluctuation velocity for i^{th} size particles due to Brownian motion, v_{dti} is the most probable fluctuation velocity for i^{th} size particles due to turbulent motion, v_{dtbi} is the fluctuation velocity for i^{th} size particles due to turbophoresis, $m(d_i)$ is the mass of an asphaltene particle in the ith fraction, and $\overline{V_y'^2 \left(\frac{d_i}{2} \right)}$ is the mean square fluid fluctuation velocity at the moment an ith size asphaltene particle touches the wall .

The shear removal term is expressed as

$$k_{sr} = \left(a + \frac{b}{\tau_w} \right)^n \tag{2.11}$$

where τ_w is the shear stress at the wall, and $a, b,$ and n are fitting parameters.

Since it was assumed most depositing particles are submicron particles, Brownian motion is considered to be the dominant mode of transport to the wall and the term for turbophoresis is neglected. It is also assumed that the particle-wall interaction efficiency (γ) is constant; that is, all asphaltene particles have the same "stickiness" regardless of size. This parameter is treated as a fitting parameter along with the critical particle diameter d_{cr}. Overall, ignoring the shear removal term, the model has three fitting parameters (α, γ, d_{cr}) but has six fitting parameters ($\alpha, \gamma, d_{cr}, a, b, n$) in when shear removal is included.

The model was shown to be able to match deposition profiles produced from five different reservoir fluids from the Gulf of Mexico (Akbarzadeh *et al.* 2012). After performing a sensitivity analysis, Akbarzadeh *et al.* was able to reduce the fitting parameters of the model to two: the particle-particle collision efficiency and the exponent n in the shear removal term. If a reservoir

fluid from a different source is used, it is likely that the model would have to be retuned with the six fitting parameters in order to provide accurate predictions of the deposit profile. The disadvantages of this model are the large number of fitting parameters and its inapplicability at higher temperatures where the morphology of the asphaltene-rich phase changes to that of a dispersed liquid.

2.5.5 ADEPT Asphaltene Deposition Model

The ADEPT model was developed using data from capillary experiments where fluid flow was in the laminar regime. This model is based on the transport of asphaltene particles within a pipe or wellbore and captures asphaltene precipitation, aggregation, and deposition (Vargas *et al.* 2010). It has been successfully applied to match deposition profiles in capillary flow experiments and in the field. The original formulation of the model includes precipitation, aggregation, transport and adsorption mechanisms but no erosion. A key assumption in the model is that only primary asphaltene particles (no asphaltene aggregates) take part in the deposition process because inertia causes the aggregates to be carried away by the fluid flow. The concentration of primary particles is given by:

$$\frac{\partial C_A}{\partial t} = k_P\left(C_0 - C_A^{eq}\right)exp\left(-k_P\frac{z}{\langle v_z\rangle}\right) - v\frac{\partial C_A}{\partial z} + \frac{1}{r}\frac{\partial}{\partial r}\left(D_A \cdot r \cdot \frac{\partial C_A}{\partial r}\right) - k_{Ag}C_A \qquad (2.12)$$

where C_A is the concentration of asphaltene particles, C_0 is the concentration of asphaltene particles at the inlet, C_A^{eq} is the equilibrium asphaltene concentration, v is the fluid velocity, $\langle v_z\rangle$ is the average fluid velocity under turbulent conditions, D_A is the diffusivity constant, k_P is the kinetic constant for precipitation, and k_{Ag} is the kinetic constant for asphaltene aggregation. The axial direction along the pipe, radial direction across the pipe, and time are represented by *z, r,* and *t* respectively. The initial condition for the model is given by:

$$C_A = C_0 \ at \ t = 0, for \ all \ r, z \qquad (2.13)$$

and the boundary conditions are as follows:

$$\frac{\partial C_A}{\partial r} = 0 \ at \ r = 0, for \ all \ z \qquad (2.14)$$

$$D_A\frac{\partial C_A}{\partial r} = -k_D C_A \ at \ r = R, for \ all \ z \qquad (2.15)$$

$$C_A = C_0 \ at \ z = 0, for \ all \ r \qquad (2.16)$$

where k_D is the kinetic constant for deposition.

The first term on the right hand side of Eq. 2.12 accounts for the appearance of the asphaltene particles by precipitation and accounts for precipitation over time (in effect over distance of flow). The equilibrium concentration of asphaltenes is predicted using the PC-SAFT equation of state. Physical and thermodynamic properties such as densities and saturation pressures are required as inputs in order to characterize the oil and tune the equation of state. The kinetic constant for precipitation, k_p, is a fitting parameter.

The second and third terms on the right hand side of Eq. 2.12 account for the transport of asphaltene particles in the axial and radial directions, respectively. Axial transport is assumed to occur by advection only (negligible axial diffusion). Radial transport is assumed to occur by diffusion only. and is modelled using Fick's law. The diffusivity is a required input. The fourth term on the right hand side of Eq. 2.12 accounts for asphaltene particle aggregation which is modeled as a pseudo first order reaction. Finally, asphaltene deposition is also modeled as pseudo first order reaction via a boundary condition applied at the pipe surface (Eq. 2.15). The kinetic constants for aggregation, k_{Ag}, and depostion, k_D, are fitting parameters.

The model has a total of three fitting parameters: k_P, k_{Ag}, and k_D. Additional input parameters include the diffusivity, the dimensions of the pipe, and the fluid flow rate. The fluid properties required for the asphaltene precipitation model are also required inputs. The output of the model is a deposit profile along the pipe or wellbore.

The model was later reduced to one dimension in order to reduce the computational time required to run the model and to incorporate the effect of turbulent diffusion (Kurup *et al.* 2011). The constant diffusivity in the original model was replaced with an axial dispersion term which included both Brownian and turbulent diffusion. Since the model was originally developed from capillary flow experiments, further modifications were applied to the model to simulate the turbulent flow observed in the field. The model was adjusted to distinguish between bulk flow and boundary layer flow, and it was assumed that the fluid flow observed in the capillary experiments is similar to the flow in the laminar boundary layer (Kurup *et al.* 2012). In addition, a pseudo-transient simulator was developed to account for the changes in velocity and pressure drop due to the buildup of the deposit layer. The disadvantage of this model is that it is not applicable at higher

temperatures where the morphology of the asphaltene-rich phase changes to that of a dispersed liquid.

2.6 Asphaltene Deposition in the Glass Transition and Liquid Regime

Asphaltene deposition at temperatures where asphaltenes undergo glass transition or are liquid droplets has only been studied in a limited extent, mainly through investigating fouling in heat exchangers. Multiple factors may contribute to fouling in heat exchangers including suspended impurities (dirt, clay), precipitated asphaltenes, insoluble gum, and coke formation. This thesis and the discussion below will be centered around asphaltene deposition. Similar to Section 2.5, methods to measure asphaltene deposition are reviewed first, followed by the observed deposition behavior, and lastly an asphaltene deposition model from the literature is presented.

2.6.1 Asphaltene Deposition Measurement

Asphaltene deposition at temperatures from 185 to 310°C has been investigated with a flow loop apparatus (Watkinson, 1968; Asomaning and Watkinson, 2000; Watkinson, 2007; E and Watkinson, 2009). Heavy oil is blended with a diluent such as fuel oil, Paraflex lubrication oil, and heavy vacuum gas oil. The mixture is brought to experimental conditions, passed through a test section, and recirculated around the flow loop. The test section consists of an electrically heated annular probe which can be removed from the apparatus at the end of each experiment to examine the deposits with an electron microscope. The deposition rate is based on the change in heat transfer coefficient. As a deposit builds, it increases the thermal resistance of the heat transfer surface, which results in a decrease in the heat transfer coefficient. Limitations associated with using flow loop apparatuses to analyze asphaltene deposition have been discussed previously in Section 2.5.1.

2.6.2 Asphaltene Deposition Behaviour

Asphaltene deposition has been shown to increase in heavy oil blends where the diluents induce greater asphaltene precipitation. For example, in diluents with a higher saturate content such as Paraflex or a *n*-pentane-fuel oil mixture, the initial rate of deposition was greater compared to a heavy vacuum gas oil or xylene-fuel oil mixture (Asomaning and Watkinson, 2000; Watkinson, 2007; E and Watkinson, 2009).

In experiments where the temperature of the bulk fluid was kept constant at 85°C and the initial surface temperature of the annular probe varied from 185 to 310°C, the initial asphaltene deposition rate grew with increases in surface temperature (Watkinson, 1968; Asomaning, 1997; Asomaning and Watkinson, 2000; E and Watkinson, 2009). Upon inspecting the deposit with an electron microscope, a dual layer deposit was formed. The deposit layer closest to the probe was tightly packed and bound to the surface while the outer layer was more porous and loosely attached. Due to the high temperatures and long experimental runtimes (up to 50 hours), the inner deposit layer were most likely asphaltenes initially that underwent thermal reactions to form petroleum coke (Asomaning, 1997). When the initial surface temperature of the annular probe was kept constant at 220°C and the temperature of the bulk fluid allowed to change from 60 to 100°C, the initial deposition rate decreased as the bulk fluid temperature increased. From 100 to 140°C, the initial deposition rate reached an asymptotic minimum, suggesting that as the bulk fluid temperature increases, the asphaltenes in the oil become more soluble, thus reducing the amount of precipitation and deposition.

2.6.3 Transport-Adhesion Model

The transport-adhesion model was developed by Watkinson to capture fouling in heat exchangers in order to optimize their operating time. Although applied in the transition or liquid phase regime, the model assumes that the asphaltenes act as glassy particles. It primarily focuses on describing the transport and adhesion of asphaltenes to the deposition surface. This model applies to any kind of particle deposition and is not specific to asphaltene deposition.

As deposits accumulate onto the surface of heat exchangers, the overall thermal resistance increases, which corresponds to a decrease in the heat transfer coefficient and causes the temperature of the deposition surface to increase. The change in heat transfer coefficient is related to the deposition rate as follows:

$$\frac{dR_{fo}}{dt} = \frac{d\left[\frac{1}{U}\right]}{dt} = \frac{1}{k_f}\frac{dx_{dep}}{dt} \tag{2.17}$$

where R_{fo} is the thermal resistance due to fouling, U is the heat transfer coefficient, x_{dep} is the deposit thickness, and k_f is the thermal conductivity.

The deposition rate is calculated as follows:

$$\frac{dx}{dt} = a_1 k_m (C_b - C_w) S - a_2 \tau_w x_{dep} \tag{2.18}$$

where a_1 and a_2 are empirical fitting constants, k_m is the mass transfer coefficient, C_b is the concentration of asphaltenes in the bulk of the fluid, C_w is the concentration of asphaltenes at the wall, S is the sticking probability, and τ_w is the shear stress at the wall. The first term on the right hand side of Eq. 2.18 accounts for the transport and adhesion of asphaltene particles to the wall while the second term accounts for the removal of asphaltene particles due to shear. The asphaltenes are assumed to be spherical particles. In Watkinson's model, the sticking probability was further expanded into:

$$S = S_o \frac{F_{ad}}{F_d} \tag{2.19}$$

where S_o is an empirical fitting constant, F_{ad} is the adhesion force between the particle and the wall, and F_d is the drag force on the particle. The model assumes the adhesion force is proportional to the surface area of the asphaltene particle and is similar to a chemical reaction that can be described by the Arrhenius equation as follows:

$$F_{ad} = a_3 D_p^2 e^{-\frac{E}{RT_s}} \tag{2.20}$$

where a_3 is an empirical fitting constant, D_p is the diameter of the asphaltene particle, E is the activation energy, R is the universal gas constant, and T_s is the temperature of the deposition surface. The drag force exerted on the particle is calculated at a distance of $D_p/2$ when the particle is just contacting the wall. Assuming a linear velocity distribution in the laminar sub-layer next to the wall, the velocity of the particle at this point can be expressed as:

$$v_p(y) = \frac{y \rho v^2 f}{2\mu} = \frac{D_p \rho v^2 f}{4\mu} \tag{2.21}$$

where v_p is the velocity of the asphaltene particle, y is the vertical distance from the wall, ρ is the density of the fluid, v is the velocity of the fluid, f is the Fanning friction factor, and μ is the viscosity of the fluid. The drag force is then calculated as follows:

$$F_d = \frac{\rho}{2} v_p^2 A_p C_D = \frac{\rho}{2} \left(\frac{D_p \rho v^2 f}{4\mu} \right)^2 \frac{\pi}{4} D_p^2 C_D \tag{2.22}$$

where A_p is the cross sectional area of the particle, and C_D is the drag coefficient. The drag coefficient is a function of the particle Reynolds number, which can be calculated as follows:

$$Re_p = \frac{\rho D_p v}{\mu} \tag{2.23}$$

Substituting the expanded terms of Eq. 2.19-2.22 into Eq. 2.18, the final equation becomes:

$$\frac{dx}{dt} = a_4 k_m (C_b - C_w) \frac{e^{-\frac{E}{RT_s}}}{D_p^2 v^4 f^2 C_D} - a_2 \tau_w x_{dep} \tag{2.24}$$

where a_4 is a collection of the constant terms given by:

$$a_4 = \frac{128 a_1 a_3 S_o \mu^2}{\pi \rho^3} \tag{2.25}$$

Many variations of the transport-adhesion model are available in the literature (Watkinson, 1968; Epstein, 1997; Ebert and Panchal, 1997; Yeap *et al.* 2005; Watkinson, 2007) and Watkinson's model was chosen only for illustrative purposes. It should be also noted that the model presented above is only applicable to early-time deposition behaviour before significant deposit buildup. For the latter case, the velocity of the fluid would change due to restrictions in the flow diameter. In general, all transport-adhesion models start with Eq. 2.18 and arrive at different final forms due to the assumptions made in each model. The shortcoming of these models are the large number of fitting parameters that do not have a physical basis. In addition, the model erroneously assumes asphaltenes precipitate as glassy particles and does not consider changes in the asphaltene morphology at the high temperatures often encountered in heat exchanger operations. Transport-adhesion models are likely insufficient to model asphaltene deposition as they do not take into account asphaltene precipitation and aggregation, which can play a significant role in the deposition process.

2.7 Summary

Depending on the temperature and solvent conditions, asphaltenes can precipitate as glassy particles or as part of a viscous heavy phase. Asphaltene deposition in the glassy particle regime has been extensively investigated and includes precipitation, aggregation, transport, adhesion, and erosion steps. Asphaltene deposition onto hot surfaces (185 to 310°C) where they can deposit and react has also been investigated. This process is modeled as mass transfer and adhesion to a surface with simultaneous erosion. However, no studies were found on asphaltene deposition in the glass transition and liquid regime at the temperatures that may be encountered in deep offshore production; that is, from 80 to 130°C.

Chapter 3: Experimental Methods

This chapter describes the experimental methods used in this thesis. First, asphaltene onset and yield measurements were required to determine when an experiments was in the single or two phase region and to determine the particle (or heavy phase) concentrations in the feed in the two phase region. Previously developed procedures used to determine asphaltene yield curves and the onset of asphaltene precipitation in solvent diluted bitumen are presented. Then, the new apparatus and procedure for obtaining asphaltene deposition measurements are discussed in detail including the design key parameters and the tests used to validate the method.

3.1 Materials

The bitumen sample used in this study, WC-B-A3(8), is a Western Canadian bitumen obtained from a SAGD process and provided by Japan Canada Oil Sands Ltd. The terms in the sample name describe the region (WC = Western Canada), the type of oil (B = bitumen), the source reservoir (A3), and the sample number (8). The sample number is for internal use and this sample will be designated as WC-B-A3 for the remainder of the thesis. The WC-B-A3 sample was dewatered in the field. Its molecular weight, density, viscosity and SARA assay were measured in a previous study (Grimaldo-Aguilar, 2018) and are presented in Table 3.1. In addition, *n*-heptane (99.5% purity) was purchased from Fisher Scientific. Industrial grade nitrogen (purity) and cyclohexane (99.0% purity) were purchased from Air Liquide Canada Inc. and MilliporeSigma respectively. Toluene of 99.5% purity was purchased from Fisher Scientific.

Table 3.1: Selected properties of WC-B-A3 bitumen from Grimaldo-Aguilar (2018).

Property	WC-B-A3 Bitumen
Density, g/cm^3 at 20°C	1.009
Viscosity at 20°C and 1 atm, mPa.s	317000
Molecular weight, g/mol	570
Saturates, wt%	19.2
Aromatics, wt%	41.0
Resins, wt%	18.2
C5-asphaltenes, wt%	20.2

3.2 Asphaltene Yield and Onset Measurements

Asphaltene yields were only measured at ambient conditions (21°C and 0.1 MPa). Yields at higher temperatures were predicted from the Modified Regular Solution model, as will be discussed in Appendix A.

A bench top procedure was used to determine the asphaltene yields at ambient conditions (21°C and 0.1 MPa). In this method, known masses of n-heptane and bitumen are added to a set of 30 mL centrifuge tubes to make up solvent compositions ranging from 35 to 90 wt%. The mixtures are sonicated for 1 hour and allowed to settle for 24 hours. Next, the tubes are centrifuged at 4000 rpm for 5 minutes to separate the asphaltene-rich heavy phase from the diluent-rich light phase. The supernatant is decanted and the residue washed with 20 cm^3 of solvent. The mixtures are sonicated for 1 hour and settled for an additional 24 hours. Then, the tubes are centrifuged at 4000 rpm for 5 minutes and the supernatant is removed. The tubes are left to dry for 24 hours in a fume hood at ambient conditions and then placed in a 60°C oven under vacuum for 14 days. Finally, the residual masses in each tube is measured and the yield calculated. The repeatability of the yields is ±0.5 wt% based on a 90% confidence interval and a large number of measurements over many years.

The onset of precipitation is determined by fitting the measured yields as shown in Figure 3.1 for n-heptane diluted bitumen at 21°C and atmospheric pressure. The yields are fitted using an empirical expression proposed by Johnston $et\ al.$ (2017a):

$$Y = B_1[1 - exp\{-C_1(w_{C7} - w_{onset})\}] \qquad (3.1)$$

where Y is the asphaltene yield in wt%, w_{C7} is the n-heptane content, w_{onset} is the n-heptane content at the onset of the asphaltene-rich phase, and B_1 and C_1 are constants. The constants and the onset composition are adjusted to minimize the least square error. The uncertainty of the fitted onset based on the uncertainty of the yield data is ±0.6 wt% solvent.
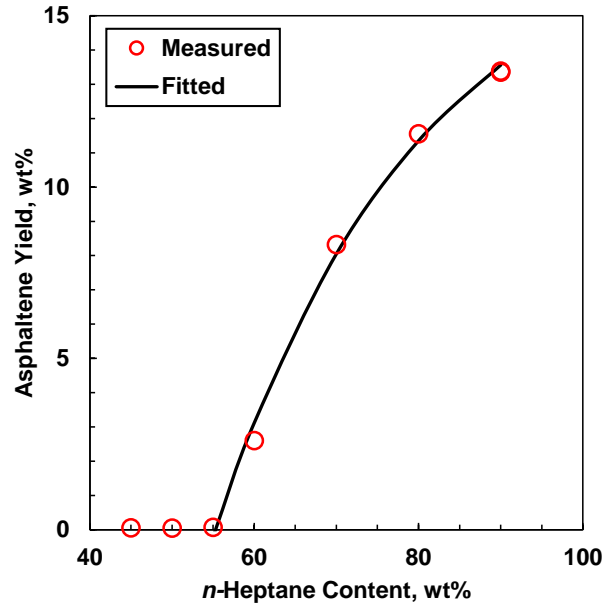
Figure 3.1 Asphaltene yield curve for bitumen diluted with n-heptane at 21°C.

3.3 Asphaltene Deposition Measurements

The deposition apparatus is designed to provide pressure drop profiles over time for deposition in capillary tube test section. In addition, the test section can be removed to determine the location, mass, and solvent content of the deposit. The apparatus, procedure, and design checks for the method are presented below.

3.3.1 Asphaltene Deposition Apparatus

A new apparatus was designed to measure the amount of asphaltene deposition in flow through a tube and is shown in Figure 3.2. The main components are two pumps, two blind cells equipped with pistons to contain *n*-heptane and pre-diluted bitumen (for injection during the experiment), a static mixer, a capillary tube where deposition occurs, a differential pressure transducer that monitors the pressure drop across the capillary tube, and an oven to house the apparatus. Other components include two hydraulic oil supply cylinders, a waste collector vessel, a backpressure regulator, a cyclohexane blind cell used to remove non-deposited materials at the end of each experiment, and a nitrogen cylinder used for pressurizing the apparatus before each experiment. The core components are described in further detail below:

- Each blind cell has a maximum pressure rating of 69 MPa and a maximum capacity of 450 cm³.

- The Quizix SP-5200 system is a variable volume positive displacement pump capable of injecting hydraulic fluid at flow rates in the range of 0.0001 to 15 cm³/min. It has a maximum pressure rating of 69 MPa.

- The Demi 2510S pump is a variable volume positive displacement pump capable of injecting hydraulic fluid at flow rates in the range of 0.01 to 10 cm³/min. It has a maximum pressure rating of 17.2 MPa.

- The static mixer is a custom-made design intended to create crossflow between pre-diluted bitumen and solvent to promote better mixing. More details are provided below.

- The capillary tube (test section) has an internal diameter of 1.8 mm and a length of 30 cm. The dead volume is 0.72 cm³. Ball valves (Swagelok ® SS-42GS4) are located on each side of the capillary tube so that the tube can be isolated from the rest of the apparatus.

- The Rosemount 1151 differential pressure transducer can detect pressure drops up to 277.46 inH$_2$O (69.04 kPa) and is precise to $\pm$ 0.01 inH$_2$O ($\pm$ 0.0025 kPa). It has a maximum pressure rating of 25.0 MPa.

- The Blue M POM-136B-1 air bath controls the temperature of the apparatus with a self-tuning temperature controller and can maintain the temperature of the oven to within $\pm$ 0.1°C.

A schematic of the static mixer is shown in Figure 3.3. The static mixer consists of a ⅛" capillary tube (3.18 mm outer diameter, 1.75 mm inner diameter) placed concentrically within a ¼" capillary tube (6.35 mm ID). Slits are cut into the ends of each tube and the tube end is crimped in to create a venturi effect. The slits create crossflow to promote mixing between the *n*-heptane and pre-diluted bitumen. The fluid with the higher velocity (either *n*-heptane or pre-diluted bitumen depending on the ratio of the two) is set to flow through the interior tube and the other fluid is set to flow through the annular space. The velocity difference between the fluid stream inside and outside the ⅛" capillary tube promotes mixing.
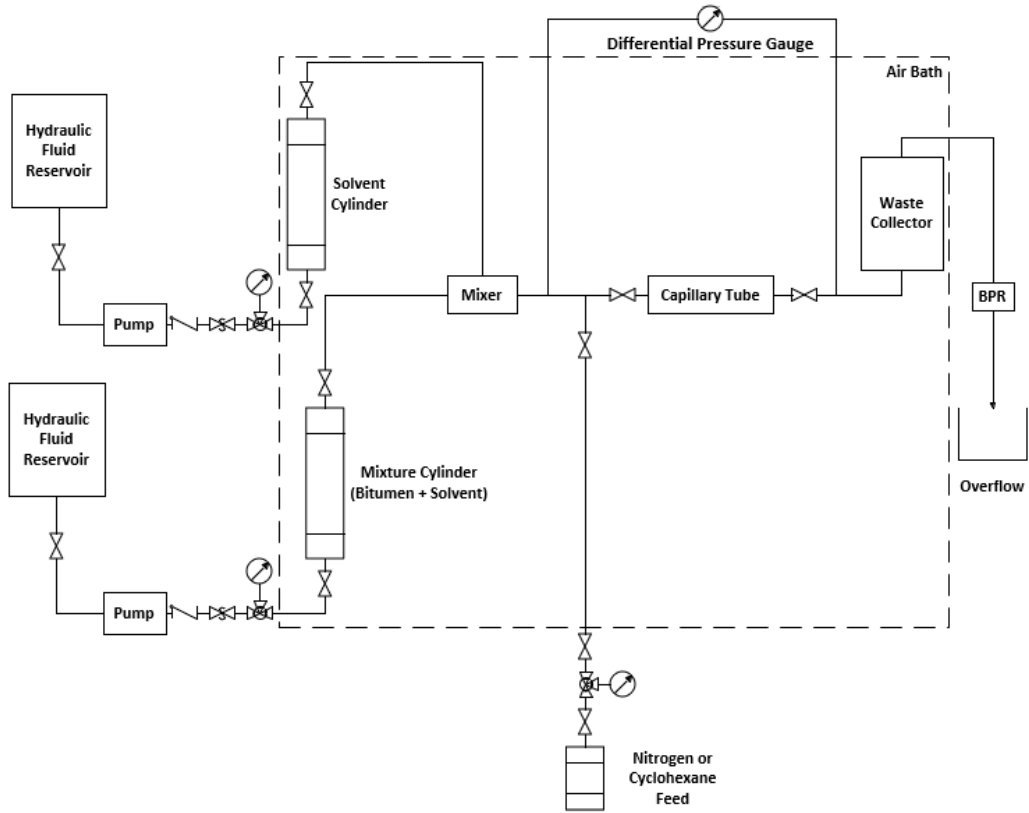
Figure 3.2 Schematic of the asphaltene deposition apparatus.
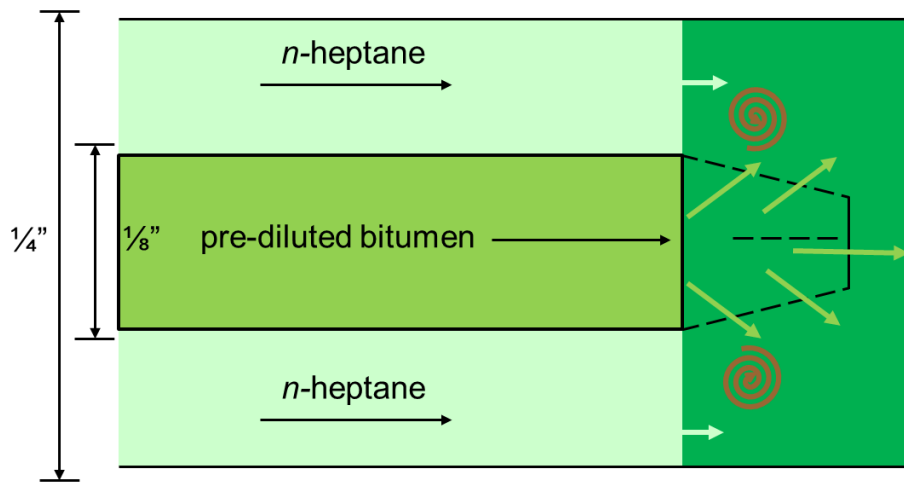
Figure 3.3 Schematic of the static mixer.

3.3.2 Experimental Procedure

Pre-dilution of Bitumen

The bitumen is pre-diluted to 50 wt% *n*-heptane (a point below the onset of precipitation) in order to reduce its viscosity and promote rapid mixing in the static mixer. A known mass of bitumen is added to a beaker with an internal diameter of 7.6 cm and a height of 13.5 cm. The beaker is placed into an 80° oven for 15 minutes to reduce the viscosity of the bitumen. The *n*-heptane is added in two steps. In the first step, 10 wt% of the total solvent mass (5 wt% of the final mixture) is added dropwise at a rate of approximately 1 cm³/min, while the solution in the beaker is stirred manually. The second step commences when the viscosity of the solution is low enough to use an impeller. A 4-blade impeller mixer with a 5 cm diameter is placed in the beaker with the pre-diluted bitumen. The mixer is turned on at 195 rpm and the remaining mass of solvent is added at a rate of approximately 1cm³/min to achieve the final solvent content.

Preparation of Capillary Tube

Before starting each deposition experiment, a new capillary tube is cut from Swagelok® tubing and deburred to smooth out any visible roughness in its flow path. The mass and length of the capillary tube are measured and recorded. In addition, the individual nuts and ferrules used to connect the capillary tube to the apparatus are weighed before they are attached to the capillary tube.

Initialization

To initialize an experiment, known masses of *n*-heptane and pre-diluted bitumen are placed into two separate blind cells. Hydraulic oil is injected into each blind cell to remove any residual air in the cells and the cells are connected to the rest of the apparatus. Nitrogen is injected to bring the apparatus to experimental pressure and to dilute the oxygen in the system. Next, approximately 40 cm³ of *n*-heptane is injected to prefill the dead volume space before the waste collector vessel. The air bath is then turned on and set to the experimental temperature. The apparatus is left at the set temperature for a minimum of four hours to allow the system to attain thermal equilibrium.

Deposition Procedure

After the apparatus is brought to temperature, solvent and pre-diluted bitumen are injected separately to the static mixer at a fixed total volumetric rate. The volumetric flow rate is specified at ambient conditions (21°C) and then converted to experimental conditions by accounting for the thermal expansion of the hydraulic oil. The fluids are mixed to reach the experimental compositions (typically between 65 to 90 wt% n-heptane). The mixture is passed through the capillary tube (the test section) where the pressure drop across the test section is monitored to detect asphaltene deposition. Once the mixture leaves the test section, it travels to a waste collection cylinder, where it is stored until the end of the experiment.

When the target time of the experiment is reached (approximately 3 hours and 40 minutes), the pumps are turned off to stop the fluid injection. The oven is turned off and its doors are opened to allow the apparatus to cool. The Demi 2510S pump is disconnected from the solvent cylinder and connected to the cyclohexane feed. Within 20 minutes of shutting the pumps off, approximately 15 cm³ of cyclohexane at room temperature is injected to remove any undeposited material in the capillary tube and to help cool the capillary tube. Then, the capillary tube is removed from the apparatus to measure the mass and location of the deposits. The ball valves at either end of the capillary tube are closed, isolating the test section from the rest of the apparatus. The nut at the outlet end is slowly loosened allowing the fluid inside the tube to depressurize before removing the tube from the apparatus. The residual fluid is drained and the tube is set aside for further analysis, which is described below. The rest of the apparatus is disassembled and cleaned with toluene.

Measurement of Solvent Content in Deposit

Once the capillary tube is taken out of the apparatus and its mass is monitored over time to determine the solvent content of the deposit. In the first stage of drying, the solvent that coats the deposit and the tube will evaporate. In the second stage, the solvent inside the deposit will diffuse out and evaporate as well. Since the evaporation rate is faster in the first stage, there are two distinctive regions when the mass of the deposit is plotted as a function of time, as shown in Figure 3.4. Each region is fitted with a curve and the mass of solvent inside the deposit is determined from the intercept of the curves. The solvent content of the deposit is then calculated from the mass

of solvent in the deposit and the dry mass of the deposit. The solvent content of the deposit consists of both entrained solvent and solvent within the deposit.
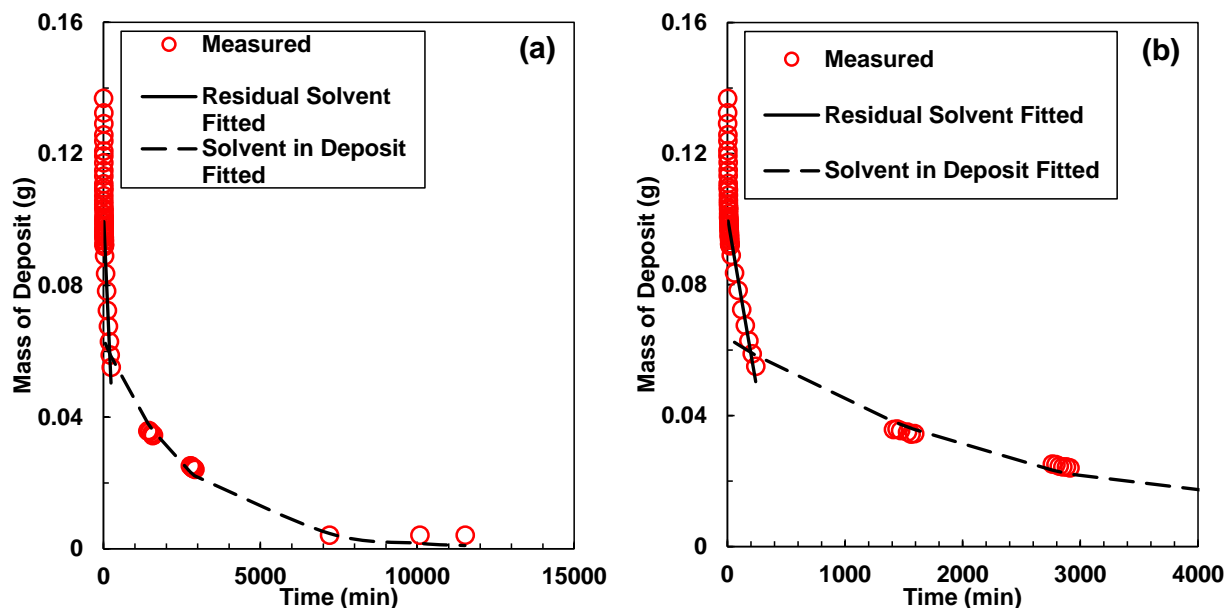
Figure 3.4 Solvent drying curve for experiment at 90 wt% n-heptane for a) entire drying process; b) initial 4000 min of drying process.

Mass and Location of Deposit

Once the deposit is completely dry, the capillary tube is cut into four equal segments. The mass of each segment is measured and the mass of deposit is determined from the difference between the mass of each segment and the mass of the capillary tube in each segment. The capillary tube mass is calculated from the length of the segment and the nominal mass/length of tube. The average mass/length is calculated from the known masses of the individual components used to construct the capillary tube. The deposit masses are then corrected based on the total mass lost during the cutting procedure averaged over each segment.

3.4 Design Checks on Deposition Measurement Method

The following factors may prevent the collection of representative, accurate, and usable data during deposition experiments with the new apparatus:

- the effectiveness of the mixing of bitumen and solvent in the pre-dilution stage and in the static mixer
- the detection limit of the differential pressure transducer
- the disruption of the deposit bed when flushing the capillary tube prior to removal from the apparatus

Each factor is discussed below.

3.4.1 Mixing of Bitumen and Solvent

It is possible that the bitumen and solvent do not completely mix during pre-dilution or in the static mixer. First, consider the pre-dilution step. If solvent is added too quickly to the bitumen during pre-dilution, the high local solvent concentration will cause premature asphaltene precipitation. Asphaltene precipitation is difficult to reverse and therefore the final concentration of insoluble asphaltenes will be higher than expected and could alter the subsequent deposition experiment.

A modified bench top procedure was used to confirm that there was no premature asphaltene precipitation after the pre-dilution procedure. Known masses of the pre-diluted mixture were placed into 30 mL centrifuge tubes and then known masses of *n*-heptane were added to each tube to bring the mixture above the onset of precipitation. The solvent content in the tubes ranges from 55 to 90 wt%. The asphaltene yields were then measured using the procedures described previously in Section 3.2. Figure 3.5 shows a comparison of the asphaltene yields obtained from the traditional bench top method and the modified bench top method with predilution. The asphaltene yield measurements are consistent between both methods, confirming that the pre-dilution procedure did not alter the subsequent asphaltene precipitation.
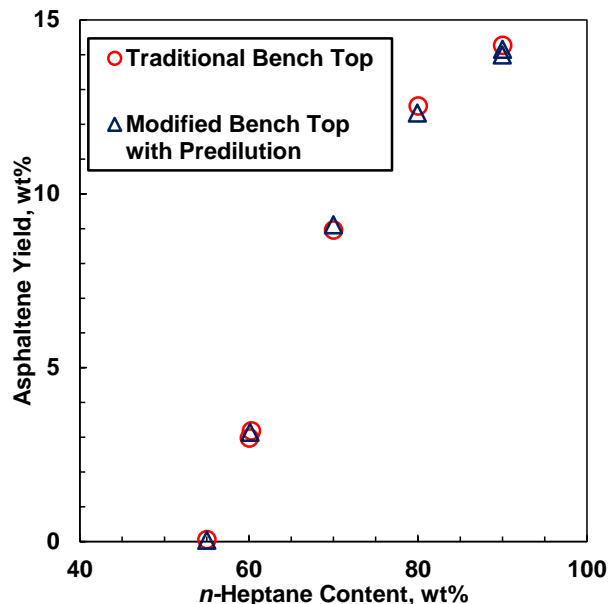
Figure 3.5 Comparison of asphaltene yield data performed with traditional bench top method and modified bench top method at 24h contact time.

Now consider the static mixer. If there is poor mixing at the static mixer, there would be incomplete partitioning of the asphaltenes in the mixture. The bitumen would not be fully dispersed which would lead to a higher than expected apparent asphaltene yield in the solvent-rich light phase. Therefore, effective mixing is indicated by yields that match the bench top method yields at the appropriate contact time.

The contact time of the static mixture was 1 min. However, it was not possible to accurately measure the asphaltene yields at 1 min using the bench top procedure. Instead, the bench top procedure was used to measure asphaltene yields at three different contact times: 24 hours, five hours, and 30 minutes. The asphaltene yields were then extrapolated to 1 min in order to obtain a baseline for complete mixing. The asphaltene yields at the three distinct contact times and the extrapolated baseline are shown in Figure 3.6.
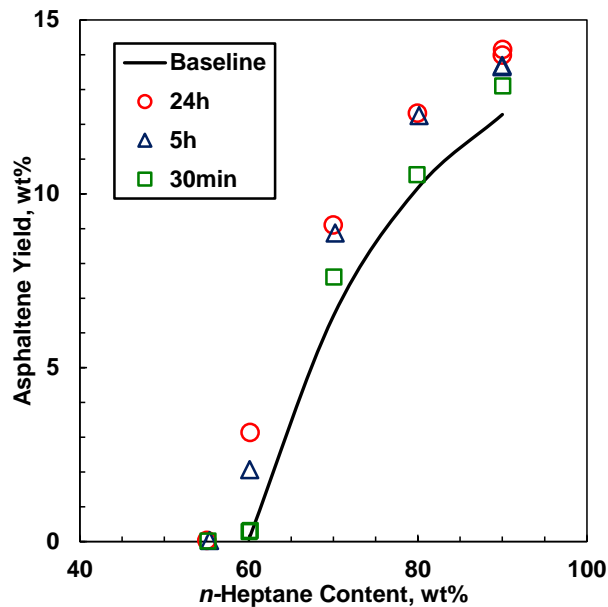
Figure 3.6 Asphaltene yield data from n-heptane diluted bitumen at different contact times. Extrapolated baseline for asphaltene yields at 1 min contact time.

Next, the Asphaltene Deposition Apparatus was modified as shown in Figure 3.7 to measure the amount of asphaltene yield in the light phase from the static mixer at ambient conditions. The lines connecting the static mixer to the differential pressure gauge and the rest of the apparatus were removed and the outlet of the static mixer was left open to the atmosphere. The static mixer was tilted slightly downwards to facilitate the sample collection process.

After the blind cells were filled with *n*-heptane and pre-diluted bitumen, the pumps were turned on to inject the mixture at solvent compositions ranging from 65 to 90 wt% of the fluid mixture. The total flow rate for the mixtures were fixed at 22.5 cm³/min. Two samples were collected for each solvent composition each in a 30 mL centrifuge tube. After filling each tube for approximately one minute, the tubes were immediately centrifuged at 4000 rpm for five minutes to separate the heavy phase from the light phase. A sample of the light phase was taken and placed into a separate clean tube. The tubes were then placed inside an 80°C oven for 14 days to evaporate all the solvent in the sample, leaving behind a residue of bitumen.

The bitumen was weighed and known masses of *n*-heptane were added to dilute the bitumen to 90 wt% solvent to precipitate all the remaining asphaltenes. The masses of asphaltene in the light phase at each solvent composition were then measured following the bench top procedure described in Section 3.2. The asphaltene yields were determined from a material balance. Figure 3.8 shows that the asphaltene yields at the static mixer outlet match the extrapolated baseline from the bench top tests to within the error of the measurements (±1.0 wt% based on 90% confidence interval), indicating there is complete mixing between the pre-diluted bitumen and solvent after exiting the static mixer.
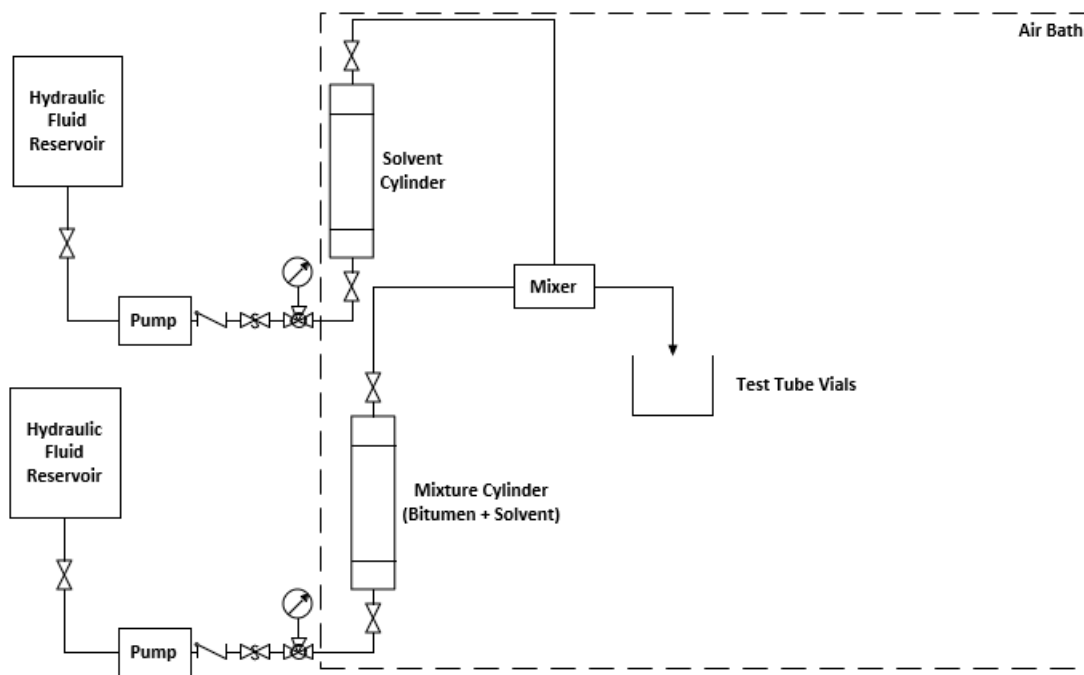
Figure 3.7 Schematic of modified asphaltene deposition apparatus used to measure asphaltene yields from static mixer.
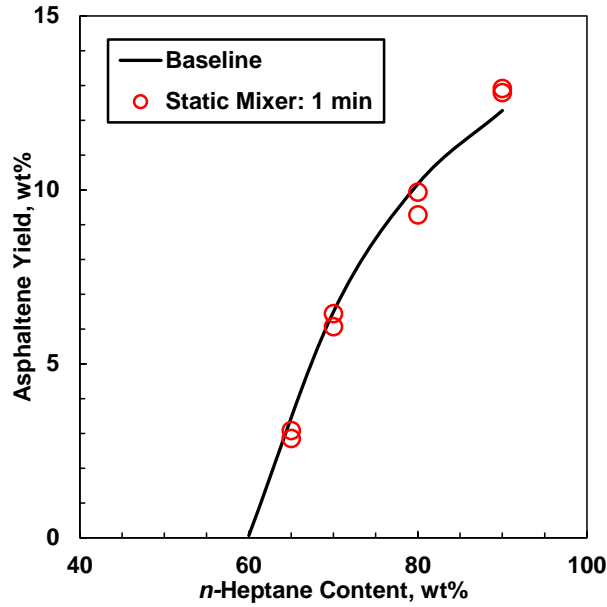
Figure 3.8 Comparison of asphaltene yield obtained from static mixer and extrapolated baseline.

3.4.2 Detection Limit of the Differential Pressure Transducer

During the experiments, the pressure drop across the capillary tube is used as an indicator of asphaltene deposition. Some of the pressure drops are very low and therefore the detection limit of the differential pressure transducer must be established before interpreting the pressure drop data from the deposition tests. The detection limit was established by comparing the pressure drop measurements for flow below the onset of precipitation with analytical predictions for pipe flow in the single phase regime.

Bitumen was pre-diluted with solvent to a point below the onset of precipitation and then flowed through the apparatus. In this single phase regime, the pressure drop can be predicted using the Hagen-Poiseulle equation:

$$\Delta P = \frac{128 \mu Q L}{\pi D^4} \tag{3.2}$$

where ΔP is the pressure drop across the capillary tube, μ is the viscosity of the fluid, Q is the volumetric flow rate, L is the length of the capillary tube, and D is the diameter of the tube. Figure 3.9 shows the pressure drop profiles at two different experimental compositions below the onset of precipitation (40 wt% and 50 wt% n-heptane). The predicted pressure drop from the Hagen-

Poiseulle equation is also shown in each plot by the dashed lines. In all cases, the measured pressure drops fluctuate and are generally above the theoretical pressure drop. There is also an initial startup period of approximately 30 minutes where the apparatus is equilibrating.
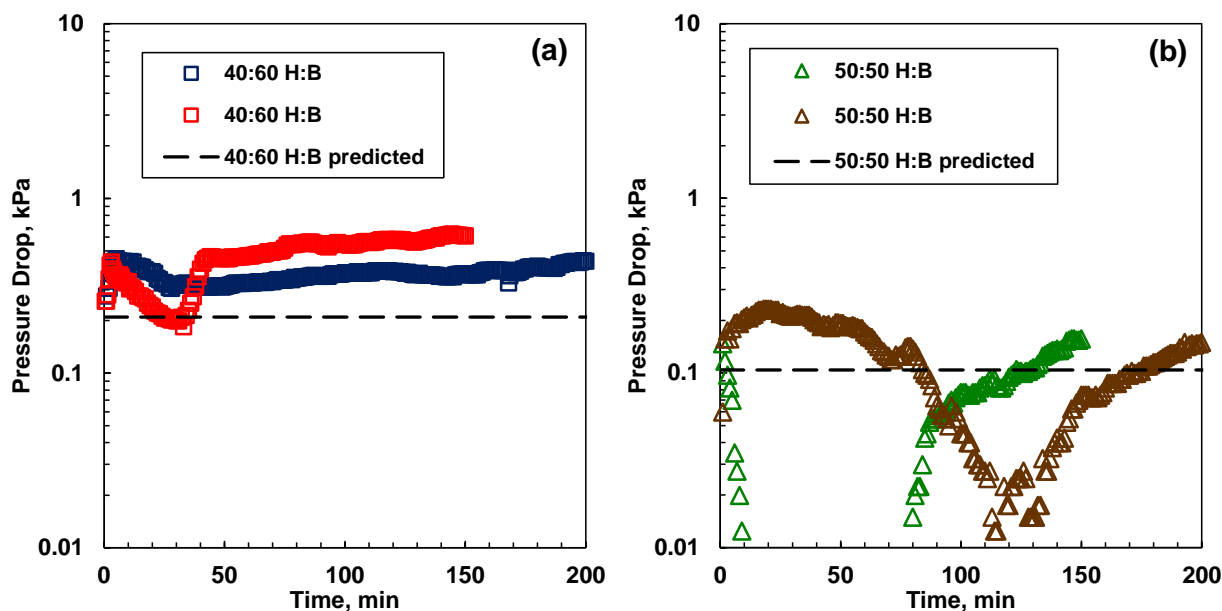
Figure 3.9 Pressure drop profiles below the onset of precipitation for a) 40 wt% n-heptane mixture b) 50 wt% n-heptane mixture.

In addition, an experiment where bitumen was pre-diluted to 50 wt% toluene (instead of *n*-heptane) was performed and the pressure drop profile is shown in Figure 3.10. Similar to the experiments above, there are oscillations in the pressure drop even though there are no precipitated asphaltenes in the solution and the magnitudes of the observed pressure drop are greater than the theoretical pressure drops. The detection limit of the differential pressure gauge was taken to be the maximum measured differential pressure and is approximately 0.6 kPa. Measured data below this value are ambiguous as they are within the error of the differential pressure gauge, and only data above this value are interpreted as indicators of asphaltene deposition. The precision of the pressure measurement above the threshold is ± 0.0025 kPa. The uncertainty of the measurement above the threshold was ±0.25 kPa based on a 90% confidence interval and the variation of the initial differential pressure gauge before flow.
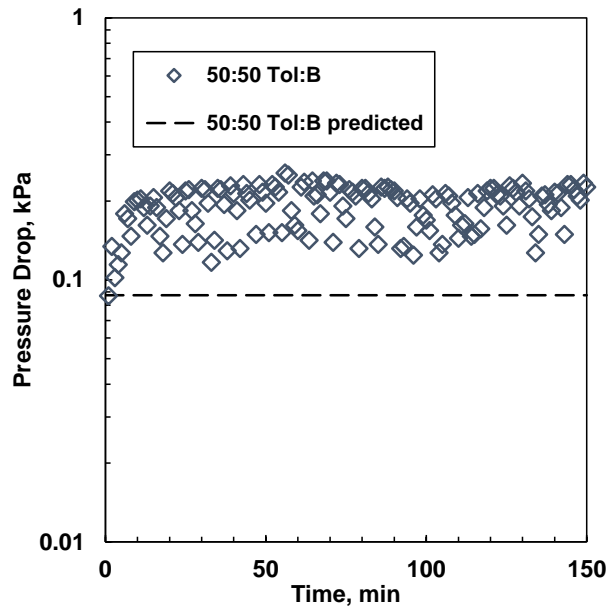
Figure 3.10 Pressure drop profile for 50 wt% toluene mixture.

Figure 3.11 shows the pressure drop profile for an experimental composition of 65 wt% *n*-heptane above the onset of precipitation. The pressure drops are both above the detection threshold of 0.6 kPa and the theoretical pressure drop, indicating that deposition has occurred. Hence, differential pressure data above the threshold can be used to assess asphaltene deposition. Differential pressures below the threshold of 0.6 kPa will be screened out henceforth.
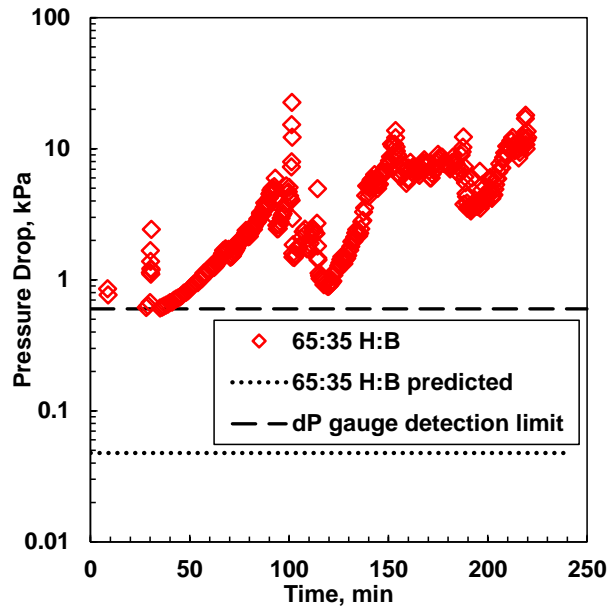
Figure 3.11 Pressure drop profiles above the onset of precipitation for a 65 wt% *n*-heptane mixture.

3.4.3 Flushing of the Capillary Tube

At the end of each experiment, any undeposited materials and the residual bitumen-solvent mixture must be flushed out of the capillary tube before it can be removed from the apparatus. In the ideal case, after the capillary tube is flushed, all of the non-deposit will be removed and the exact mass of the deposit will remain. However, if the capillary tube is not cleaned enough, a false high mass will be obtained for the deposit and the subsequent solvent content measurement will be inaccurate. On the other hand, if the capillary is flushed too much, some or all of the deposit may be removed from the capillary tube.

Three different flush methods were examined: gravity drainage, nitrogen flush, and cyclohexane flush. With the gravity drainage method, the capillary tube is removed from the apparatus set vertically to allow the free liquid inside the tube to drain out. Gravity drainage gives a low flow rate and is unlikely to remove any deposits inside the tube. Therefore, it can be used to assess if the other two flush methods will remove deposits inside the capillary tube. With the nitrogen method, nitrogen is injected to displace the residual liquid in the tube before it is isolated and removed from the apparatus. Since nitrogen is an inert gas, it should theoretically remove the residual fluid without interacting with the deposit. In the cyclohexane method, cyclohexane is

51

injected to remove the free liquid in the tube. Cyclohexane is not expected to dissolve asphaltenes from the deposit or precipitate asphaltenes from the residual liquid during the displacement time (see Section 3.4.4).

The first step in evaluating the flush methods was to determine if they could remove the residual bitumen-solvent mixture without removing the deposit. First, each flushing procedure was tested with a feed with 65 wt% n-heptane and 35 wt% bitumen, a flow rate of 2 cm³/min, and a duration of five minutes. This duration allowed the bitumen-solvent mixture to coat the capillary tube walls without having time to accumulate a deposit. Then, each procedure was tested for the same feed after a full deposition run. In all cases, the mass of deposit was measured immediately after the flush (wet mass) and after drying the capillary tube (dry mass). The residual wet and dry masses in these experiments are provided in Table 3.2. The uncertainty of the mass measurements for the N_2 flush and cyclohexane flush runs based on a 90% confidence interval and are provided in Table 3.3.

Table 3.2: Residual wet and dry masses in capillary tube for control and deposition runs. The control masses for the N2 flush and cyclohexane wash are averages from 2 runs.

Flush Method	Control Wet Mass (g)	Control Dry Mass (g)	Residual Wet Mass (g)	Residual Dry Mass (g)	Difference Dry Mass (g)
Gravity Drainage	0.131	0.024	0.161	0.032	0.008
N_2 Flush	0.061	0.021	0.114	0.044	0.023
N_2 Flush			0.135	0.073	0.052
Cyclohexane Wash	0.087	0.004	0.157	0.014	0.010
Cyclohexane Wash			0.145	0.017	0.013

Table 3.3: Uncertainties of the masses in the capillary tube.

Flush Method	Control Wet Mass (g)	Control Dry Mass (g)	Residual Wet Mass (g)	Residual Dry Mass (g)	Difference Dry Mass (g)
N_2 Flush	±0.038	±0.010	±0.017	±0.023	±0.033
Cyclohexane Wash	±0.043	±0.004	±0.010	±0.002	±0.006

First consider the control runs. Table 3.2 shows that the gravity drainage method failed to remove the residual liquid with a wet mass of 0.131 g in the control run compared with less than 0.09 g with the other methods. To put these numbers in perspective, the calculated mass of the fluid in a full tube is 0.87 g.

The residual dry mass from the gravity drainage method was non-zero indicating that some bitumen from the residual liquid remained in the tube after drying. Both the nitrogen and cyclohexane flushes appeared to remove most of the free liquid with the remaining wet mass likely representing a surface film. The nitrogen flush left a significant residual dry mass in the control run suggesting that it did not displace the original surface film leaving some bitumen behind. It is possible that the nitrogen flow evaporated some of the n-heptane leaving a bitumen enriched material behind. The cyclohexane flush left almost no residual dry mass indicting that it displaced the original surface film.

Next, consider the deposition runs. The mass of deposit was determined from the dry mass from the deposition run less the dry mass from the control run. The cyclohexane flush provided consistent deposit masses within 0.003 g of each other. The gravity drainage method provided a similar deposit mass. It appears that the mass of bitumen left from the undisplaced liquid after drainage was consistent in the control and deposition runs and therefore subtracted out of the deposit mass calculation. The deposit mass from the nitrogen flush was significantly higher indicating that the residual masses from the control and deposition run with this method were not consistent. Therefore, the nitrogen flush method was rejected.

Finally, the capillary tubes used in the deposition runs with the drainage and cyclohexane flush methods were cut into four equal segments in order to analyze the mass distribution along the length of the tube. Table 3.4 shows that the deposit forms at the tube inlet. While the gravity drainage left a residual film, the results after subtracting the control run mass are very similar to the results from the cyclohexane flush method. This consistency suggests that the cyclohexane wash does not remove any deposit. Therefore, the cyclohexane flush method was selected for all further runs because it removed most of the free liquid and did not appear to remove any deposit. It will be shown in Chapter 5 that at higher temperatures, there are significant deposit masses in

the tube even after the cyclohexane flush, which confirms that the cyclohexane wash does not displace the deposit.

Table 3.4: Deposit mass distribution in capillary tube for deposition runs under different flush methods. The dry mass from the control run was subtracted from the dry mass of the deposition run.

Flush Method	1st (mg)	2nd (mg)	3rd (mg)	4th (mg)	Total (mg)
Gravity Drainage	13.7	-5.7	-1.3	0.7	7.3
Cyclohexane Wash	8.7	2.5	-2.5	1.3	9.9
Cyclohexane Wash	16.9	2.4	-2.9	-2.8	12.6

Based on the dry mass differences in Table 3.2 for the gravity drainage and cyclohexane flush methods, the uncertainty of the deposit mass is ±6 mg. The uncertainties of the deposit mass from the cyclohexane flush method in Table 3.3 was similar at ±6 mg. The repeatability of the dry masses at 130°C was found to be ±5 mg. Therefore, the uncertainty of the dry masses is considered to be ±6 mg. The average dry mass of the deposits in the cyclohexane flush method was 11.2 mg, slightly less than double the experimental uncertainty.

3.4.4 Cyclohexane Solvency Tests

Bitumen yield tests were performed to assess if cyclohexane would generate or dissolve existing asphaltenes when used to flush the deposit. In particular, the yields from a sediment of precipitated asphaltenes were measured without washing and with cyclohexane washing to assess if the cyclohexane wash altered the yields. A procedure similar to the bench top method in Section 3.2 was used except that, for the base case run, the residue in the centrifuge tubes was not washed with solvent after the test tubes were centrifuged and decanted for the first time. Instead, the tubes were left to dry for 24 hours in a fume hood at ambient conditions and then placed in a 60°C oven under vacuum for 14 days. Finally, the residual masses in each tube was measured and the bitumen yield was calculated to establish a baseline. In the cyclohexane wash case, cyclohexane was dripped down the walls of the tube until the sediment bed was submerged. It was observed that the cyclohexane was able to effectively clean the coating on the test tube walls, confirming its ability to remove a surface film. After the sediment bed was submerged for approximately one minute,

the cyclohexane was decanted, and the test tubes follow the same drying procedure described above. Figure 3.12 shows the yield curves obtained from the base case and cyclohexane wash case are almost the same with an average deviation of 1.9 wt% compared with an experimental error of 1.0 wt%. In other words, the cyclohexane did not significantly dissolve the sediment or precipitate material from the residual continuous phase.
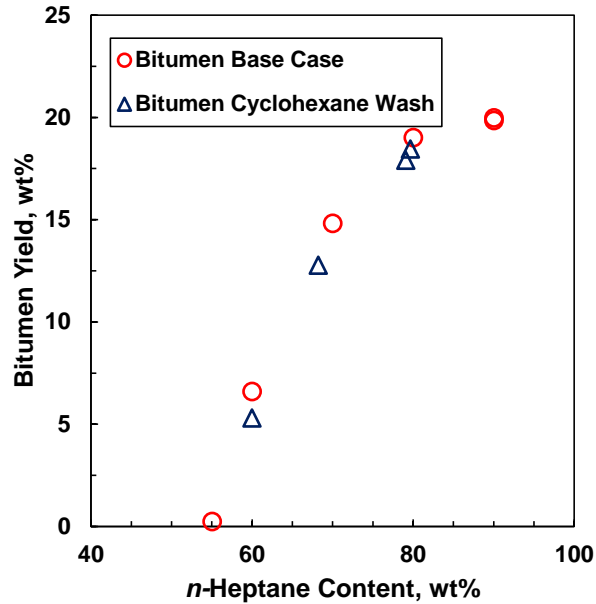
Figure 3.12 Comparison of bitumen yield with and without cyclohexane wash.

Chapter 4: Results and Discussion: Glassy Particle Regime

This chapter presents the results from deposition experiments of a bitumen and *n*-heptane system at temperatures where asphaltenes precipitate as glassy particles. First, the measured pressure drop and deposit mass and *n*-heptane content are presented. The effects of the capillary tube length, solvent composition, flow rate, and temperature are discussed. Then, the data are analyzed to determine the size of the deposits and the deposition rates. Finally, the results from this thesis are compared with data from the literature.

4.1 Direct Measurements: Pressure Drop and Deposit Mass and Solvent Content

Asphaltene deposition experiments were performed on mixtures of the WC-B-A3 bitumen and *n*-heptane. Capillary tube lengths of 3, 15, and 30 cm were used to evaluate the effect of the tube length. The I.D. of the capillary tube was 1.75 mm in all cases. Feed *n*-heptane contents from 65 to 90 wt% were assessed to determine the effect of the *n*-heptane content and insoluble asphaltene concentration on deposition. The total mixture flow rate was also varied between 2 and 4 cm³/min (at 21°C) to explore the effect of flow rate within the laminar regime (Reynold's numbers < 78 for flow through the clean tube in all cases). The Reynold's numbers within the orifice-like deposits discussed later were < 1400 in all cases. Experiments were performed at 90°C to investigate the impact of higher temperatures while remaining in the glassy particle regime. In addition, the effect of the mixing method on the deposition measurements was assessed. All experiments were performed at 0.5 MPa to ensure that no gas phase formed in the apparatus.

The data directly measured in a deposition experiment are the pressure drop profiles across the capillary tube and the mass and *n*-heptane content of the deposits. All of the recorded pressure drops were baseline shifted by correcting for the initial pressure drop reading before there was any flow in the apparatus. All data below the detection limit of the differential pressure gauge were screened out. For the sake of convenience, a mixture of X wt% *n*-heptane and (100-X) wt% bitumen will be referred to as X:(100-X) H:B.

4.1.1 Typical Deposition Experiment

Figure 4.1 shows the pressure drop profile for a mixture containing 65 wt% *n*-heptane and 35 wt% bitumen (65:35 H:B) in a 30 cm long capillary tube. The experiment was performed at 50°C and a flow rate of 2.0 cm³/min. The sharp increase in the pressure drop at the beginning of the experiment indicates that deposition occurred. The pressure drop increased approximately exponentially over time until it stabilized at approximately 150 minutes. There were also occasional fluctuations in the pressure drop during the experiment. Table 4.1 shows the mass distribution of the deposit along the test section after the tube was dried and cut into four equal segments. The deposit formed only at the tube inlet. The *n*-heptane content of the deposit was 89±7 wt%.

It appears that a small, orifice-like deposit formed at the inlet and grew for approximately 150 minutes until the velocity of the fluid through the orifice eroded the deposit as fast as it formed; that is, a steady state condition was established. The fluctuations in pressure drop suggest that the structure of the deposit was somewhat fragile such that pieces were occasionally washed away causing a sudden lower pressure drop. The deposit then regrew until the steady state was reestablished. The high *n*-heptane content of the deposit is consistent with a highly porous, easily broken structure.
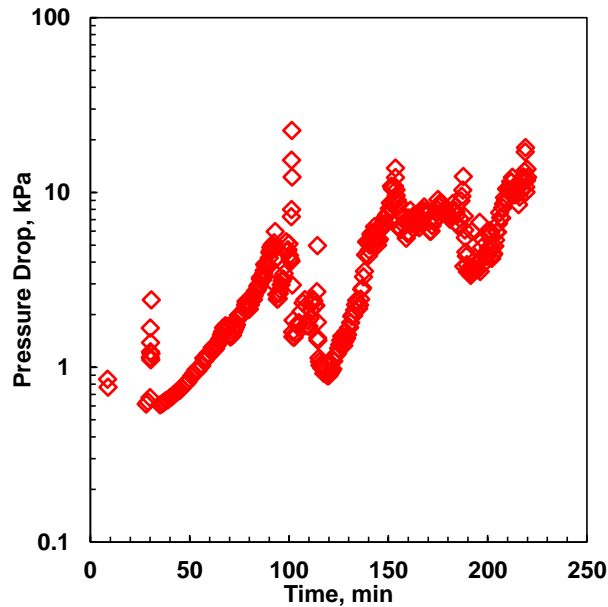
Figure 4.1 Pressure drop profile for a mixture of 65 wt% n-heptane and 35 wt% bitumen (65:35 H:B) flowing at 2.0 cm³/min in a 30 cm (1.75 mm I.D). capillary tube at 50°C. The uncertainty of the pressures is ±0.25 kPa.

Table 4.1: Mass distribution of dried deposit in a 30 cm (1.75 mm I.D) capillary tube for a 65:35 H:B feed at 2.0 cm³/min at 50°C. The uncertainty of the masses is ±6 mg. Negative values arise because the average residual surface film mass was subtracted from the total measured mass of each segment in order to obtain the deposit mass.

1st (mg)	2nd (mg)	3rd (mg)	4th (mg)	Total (mg)
16.9	2.4	-2.9	-3.9	12.6

4.1.2 Effect of Capillary Tube Length

If asphaltenes form an orifice-like deposit, then the pressure drop across the capillary is expected to be almost independent of the capillary length. In contrast, if asphaltenes form a uniform deposit along the length of the tube, the pressure drop is expected increase proportionally with the tube length. Figure 4.2a shows that changing the length of the test section did not affect the pressure drop profile at a fluid composition of 65 wt% *n*-heptane and total flow rate of 2.0 cm³/min. Figure 4.2b shows that similar results were also obtained at 90 wt% *n*-heptane.

The mass distribution along the capillary tubes for a 65:35 H:B feed are presented in Table 4.2. The deposit mass was observed at the inlet for both the 15 cm and 30 cm tubes, which confirms

the deposit was localized. The deposit mass for the 3 cm tube is not reported because the deposit shook loose from the test section when removing the tube from the apparatus. Nonetheless, the pressure drop data and the most reliable of the mass data confirm that the deposit was localized. Table 4.3 shows that the *n*-heptane content of the deposits are similar despite the differences in test section length. Both indicate that a highly porous deposit was formed.
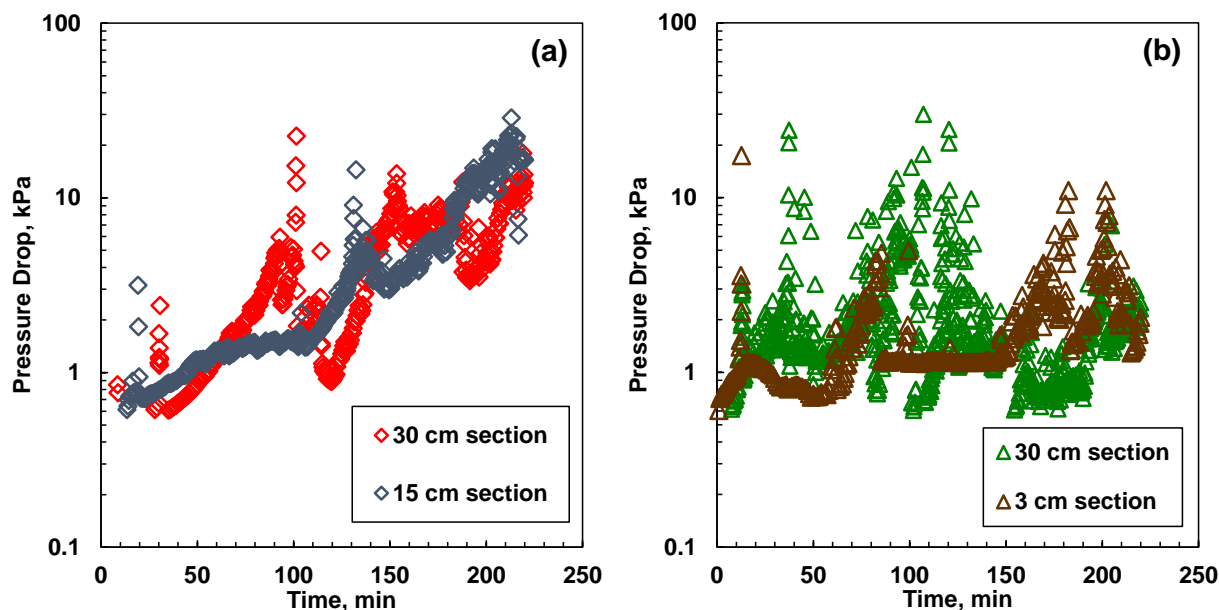
Figure 4.2: Pressure drop profile at 50°C and 2.0 cm³/min with different test section lengths: a) 65:35 H:B mixture b) 90:10 H:B mixture. The uncertainty of the pressures is ±0.25 kPa.

Table 4.2: Mass distribution of dried deposits in 15 and 30 cm (1.75 mm I.D) capillary tubes for a 65:35 H:B mixture at 2.0 cm³/min at 50°C. The uncertainty of the masses is ±6 mg.

Test Section Length (cm)	1st (mg)	2nd (mg)	3rd (mg)	4th (mg)	Total (mg)
15	10.5	3.9	5.5	4.2	24.1
30	16.9	2.4	-2.9	-3.9	12.6

Table 4.3: Effect of test section length on the *n*-heptane content of deposits for a 65:35 H:B mixture in a (1.75 mm I.D) capillary tube at 2.0 cm³/min and 50°C. The uncertainty of the solvent content is ±7 wt%.

Test Section Length (cm)	*n*-Heptane Content of Deposit (wt%)
15	87
30	88

4.1.3 Effect of *n*-Heptane Content in the Feed

The *n*-heptane content of the feed affects the concentration of precipitated asphaltene particles, the attractive forces between the precipitated particles, and the adhesion force between the particles and the tube surface. Higher amounts of precipitate increase the supply of potentially depositing material and may lead to faster deposition rates (Vilas Bôas Fávero *et al.* 2016). Greater attractive forces between particles leads to more flocculation and settling (Maqbool *et al.* 2011; Duran *et al.* 2018). Initially, flocculated asphaltenes may accelerate the deposition process because they are more likely to settle. However, as they increase beyond a critical size, they become less likely to form deposits because they can be transported away by fluid flow due to their inertia (Eskin *et al.* 2011; Eskin *et al.* 2012; Hoepfner *et al.* 2013). The adhesion of particles to the tube surface is related to the attractive forces between the particles because the tube surface is almost certainly coated with a molecular layer of adsorbed asphaltenes (Alboudwarej *et al.* 2005). Greater adhesion forces between the particles and the tube surface are expected to lead to faster deposition.

First consider the amount of precipitated particles. Duran *et al.* (2019) examined asphaltene precipitation from mixtures of bitumen and *n*-heptane. They found that asphaltenes precipitated as primary particles with diameters in the range of 200 nm to 1.5 μm. They assumed that the diameter of the primary particles was independent of the *n*-heptane content. In this case, the number of primary particles is proportional to the concentration of precipitated asphaltenes which peaked at an *n*-heptane content of approximately 75 wt% as shown in Figure 4.3.

However, aggregation also affects the number of particles. The primary particles are known to flocculate into aggregates spanning tens of microns within the first 30 seconds after precipitation

(Ferworn *et al.* 1993; Maqbool *et al*. 2011; Duran *et al*. 2018). For *n*-heptane diluted bitumen, the number and average size of the aggregates increased with increasing *n*-heptane content up to approximately 80 wt% (Duran et al., 2018). At higher *n*-heptane contents, the size of the aggregates reached a plateau and the number of aggregates decreased. Hence, the concentration of primary particles and the concentration of the aggregates both peaked at near the maximum in the mass concentration of precipitated asphaltenes (at an *n*-heptane content of approximately 80 wt%).
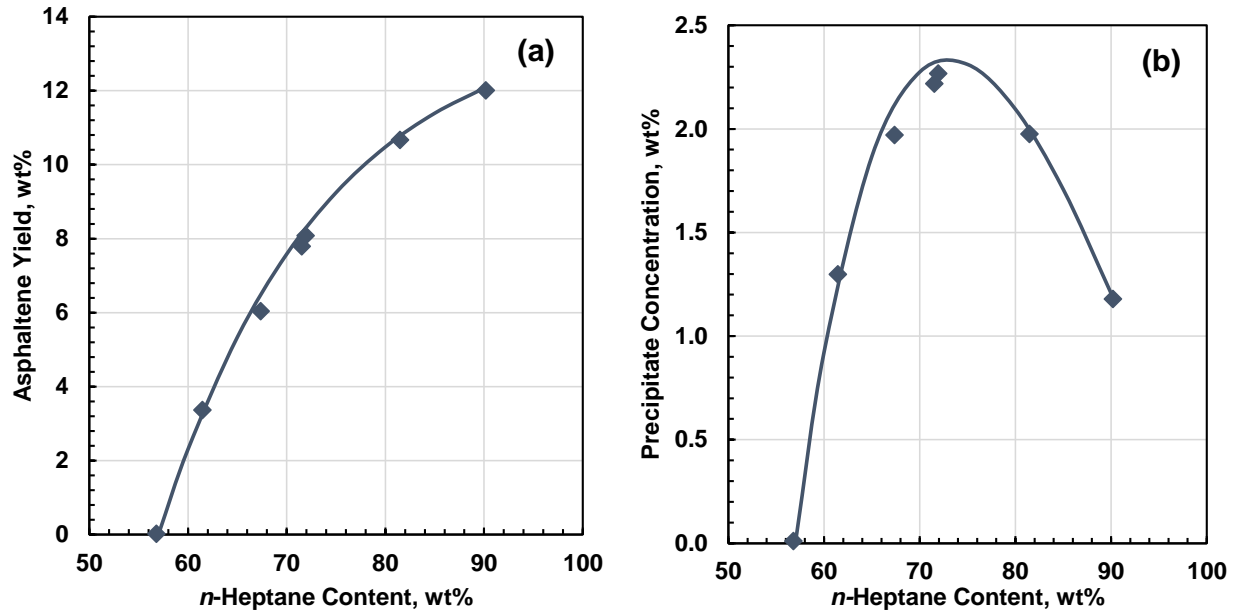
Figure 4.3 Asphaltene yield (a) and precipitate concentration (b) as a function of *n*-heptane content at 21°C after 24 hours contact time. The symbols are data; the lines are empirical equations fitted to the yield data and provided as visual aids. Adapted from Duran *et al*. (2018).

The insoluble precipitate concentration for the mixture of bitumen and *n*-heptane examined in this thesis was calculated from the asphaltene yields as follows:

$$C_A = \rho_{mix} w_{bit} Y \tag{4.1}$$

where C_A is the insoluble asphaltene concentration, ρ_{mix} is the density of the mixture, w_{bit} is the composition of bitumen in the mixture in weight percent, and Y is the asphaltene yield. Figure 4.4 shows the insoluble asphaltene concentration at different solvent contents at 21°C. As will be shown later, asphaltene solubility changes only slightly with temperature and therefore similar results are expected at 50°C. The insoluble precipitate concentration reaches a maximum at 75

wt% *n*-heptane. As discussed above, the primary and aggregate particle concentration is expected to peak at the same point. If the number of particles plays a role in the deposition process, the deposition rate would also be expected to peak at 75 wt% *n*-heptane. The deposition rate was not measured directly but the rate at which the pressure drop increased is an indirect indicator of the deposition rate. Figure 4.5 shows the pressure drop profile of the experiments at three different solvent contents. The initial deposition rate increased monotonically with increasing solvent content even above an *n*-heptane content of 75 wt%. Hence, the deposition rate cannot be attributed solely to the concentration of the precipitated particles.

Now consider the adhesion force between the asphaltenes and the tube surface. This force is expected to increase as the *n*-heptane content increases and the mixture becomes more incompatible with the asphaltenes. The deposition rate is expected to increase as the adhesion force increases and therefore is expected to increase monotonically with increasing *n*-heptane content, just as was observed. It appears that the increase in the adhesion force is the primary cause for the increase in the deposition rate.
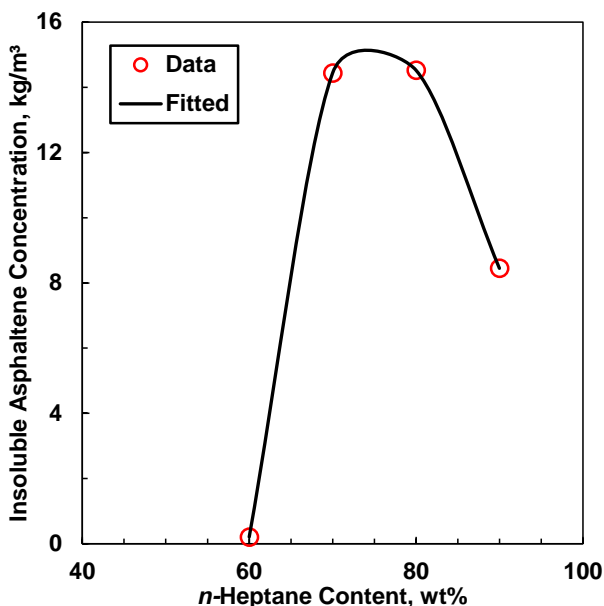
Figure 4.4 Insoluble asphaltene concentration for bitumen diluted with *n*-heptane at 21°C.
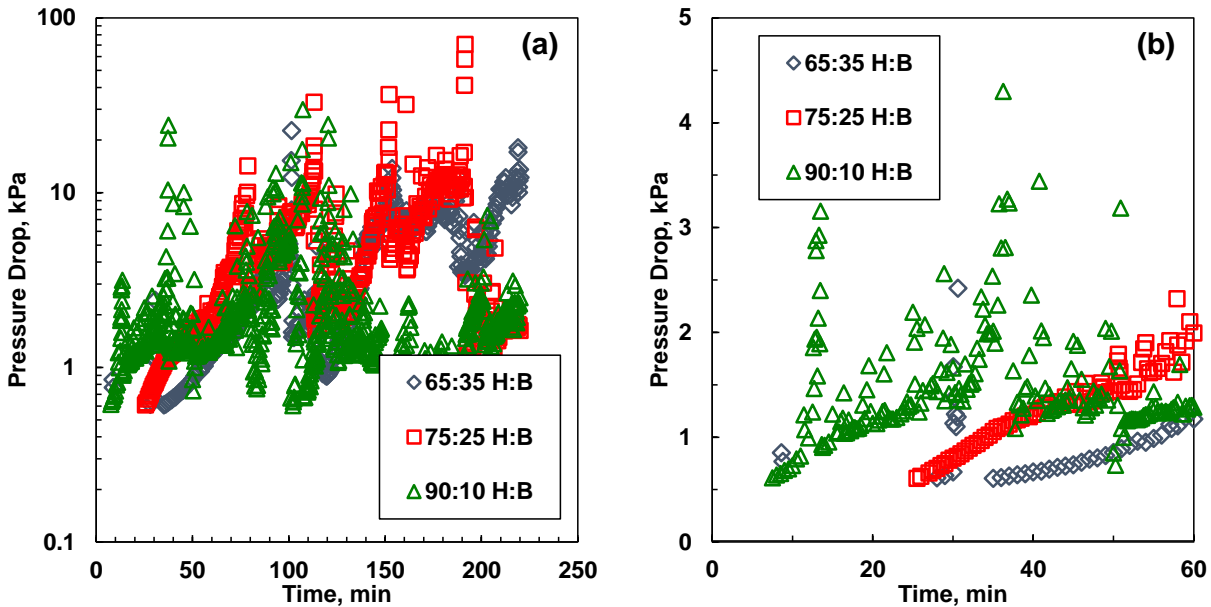
Figure 4.5 Effect of feed composition on the pressure drop profile in a 30 cm (1.75 mm I.D) capillary tube at 50°C and 2.0 cm³/min shown for: a) the entire experiment duration (3 hours and 40 minutes); b) the first 60 minutes. The uncertainty of the pressures is ±0.25 kPa.

Table 4.4 shows the mass distribution of the deposit along the capillary tube at the three different solvent compositions. The absolute masses for the deposits differed because the experiments were ended at different points in the cycles of deposition and erosion in each case. For example, there was almost no deposit left for one of the 75:25 H:B feeds with masses all within the experimental error of ±6 mg. However, in the majority of cases, the deposit was concentrated at the tube inlet, consistently forming an orifice-like deposit. In the case of the first 75:25 H:B feed and the 90:10 H:B feed, both experiments had similar final pressure drops (1.6 kPa versus 2.5 kPa), but significantly different dried masses of 3 mg and 45 mg respectively. These observations suggest that the orifice diameter did not change significantly and that the deposit grew along the length of the capillary tube. The size of the deposits will be discussed later. Table 4.5 shows that the *n*-heptane content of the deposit ranged from 71 to 95 wt%. In other words, highly porous deposits were formed at all conditions. The deposits appear to be more compact (lower *n*-heptane content in deposit) at 90 wt% *n*-heptane content in the feed. The reason for the higher compaction is not known.

Table 4.4: Effect of feed composition on the mass distribution of the dried deposits in a 30 cm (1.75 mm I.D) capillary tube at 2.0 cm³/min and 50°C. The uncertainty of the masses is ±6 mg.

H:B (w/w)	1st (mg)	2nd (mg)	3rd (mg)	4th (mg)	Total (mg)
65:35	16.9	2.4	-2.9	-3.9	12.6
65:35	8.7	2.5	-2.5	1.3	9.9
75:25	6.7	-6.4	-1.0	3.6	3.0
75:25	34.4	15.9	19.7	1.8	71.8
90:10	20.6	11.0	16.6	-2.9	45.2

Table 4.5: Effect of feed composition on n-heptane content of deposits in a 30 cm (1.75 mm I.D) capillary tube at 2.0 cm³/min and 50°C. The uncertainty of the solvent content is ±7 wt%.

H:B (w/w)	*n*-Heptane Content of Deposit (wt%)
65:35	88
65:35	91
75:25	95
75:25	79
90:10	71

4.1.4 Effect of Flow Rate

The flow rate can affect the pressure drop through the test section in two opposing ways: 1) the increase in velocity increases the pressure drop; 2) the greater erosion associated with a higher velocity (higher shear) reduces the size of the deposit and decreases the pressure drop. If the deposit is orifice-like, the pressure drop through the test section is expected to be dominated by the pressure drop through the orifice. The pressure drop is then given by:

$$\Delta P = \frac{\rho v^2}{2C_o^2}\left[1 - \left(\frac{d_o}{D}\right)^4\right] \tag{4.2}$$

where ΔP is the pressure drop across the orifice, ρ is the density of the fluid, v is the velocity of the fluid flowing through the orifice, C_o is the orifice discharge coefficient, d_o is the diameter of the orifice, and D is the diameter of the tube. Eq. 4.2 shows that an increase in velocity increases the pressure drop by 2 orders of magnitude while a decrease in the orifice diameter could decrease the pressure drop by 4 orders of magnitude.

Figure 4.6a shows that changing the flow rate from 2.0 to 4.1 cm³/min (Reynold's numbers of 17 and 33 through clean tube and 335 and 361 through the orifice) had little effect on the pressure drop profile for 65:35 H:B mixtures in a 30 cm test section at 50°C. It appears the additional shear at the higher flow rate erodes just enough deposit to counteract the increased pressure drop expected from the higher velocity. Assuming the deposit is orifice-like, Figure 4.6b shows the calculated velocities through the orifice were the same in both cases.

Table 4.6 shows the mass distribution of the deposit at the two different flow rates. There is more mass in the test section at 2.0 cm³/min and the masses at 4.1 cm³/min are within the uncertainty of the measurement (±6 mg). The effect of flow rate on the amount of deposition is inconclusive, as the absolute masses for the deposits are dependent on the endpoints in each experiment, which are dictated by the cycles of deposition and erosion. Table 4.7 show that the *n*-heptane content in the deposit was slightly higher at 4.1 cm³/min than at 2.0 cm³/min in the 65:35 H:B mixtures; however, the difference is within the uncertainty of the measurement (±7 wt%).
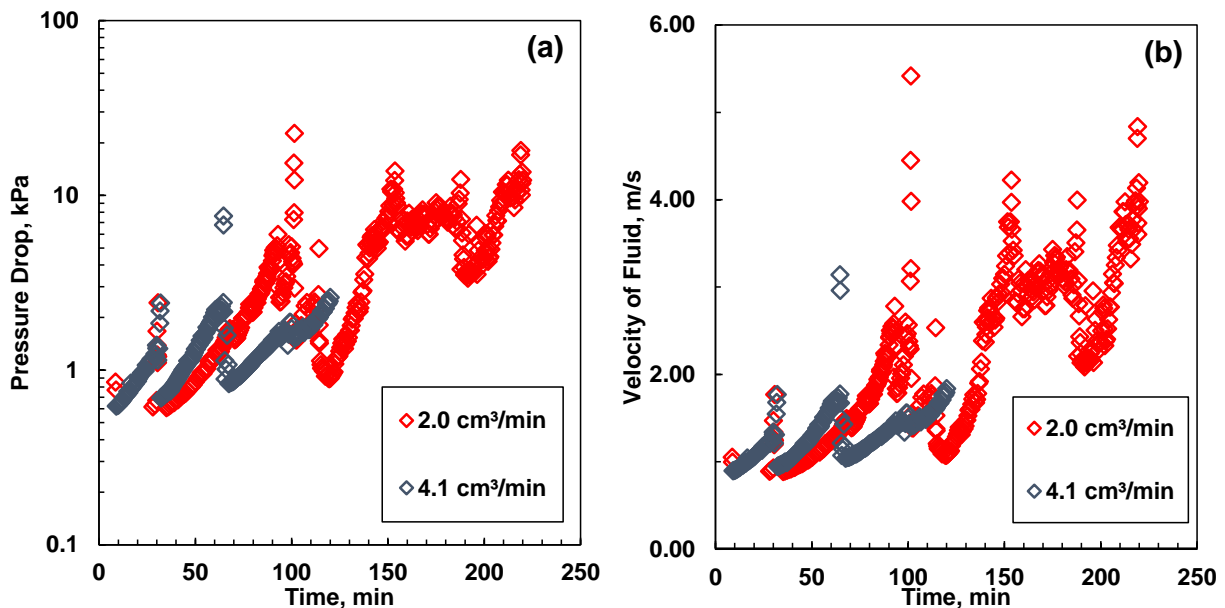
Figure 4.6 Measured pressure drop (a) and calculated velocity (b) profiles in a 30 cm capillary tube for a 65:35 H:B mixture at 50°C and flow rates of 2.0 and 4.1 cm³/min. The uncertainty of the pressures is ±0.25 kPa.

Table 4.6: Mass distribution of dried deposits in a 30 cm (1.75 mm I.D) capillary tube for a 65:35 H:B mixture at 50°C at flow rates of 2.0 and 4.1 cm³/min. The uncertainty of the masses is ±6 mg.

Flow rate (cm^3/min)	1st (mg)	2nd (mg)	3rd (mg)	4th (mg)	Total (mg)
2	16.9	2.4	-2.9	-3.9	12.6
4	-5.6	2.6	4.7	3.2	4.9

Table 4.7: Solvent content of deposits in a 30 cm (1.75 mm I.D) capillary tube for a 65:35 H:B mixture at 50°C. The uncertainty of the solvent content is ±7 wt%.

Flow rate (cm^3/min)	n-Heptane Content in Deposit (wt%)
2	88
4	93

4.1.5 Effect of Temperature

Temperature can affect deposition in several ways. At higher temperatures, asphaltenes are slightly more soluble in the oil, which reduces the amount of precipitated asphaltenes available for deposition, as shown in Figure 4.7. The precipitated asphaltenes will likely be more mobile at higher temperatures, which increase their probability of contacting the tube surface and allows deposition to be detected earlier in the pressure drop profiles (Bemani *et al.* 2019). In addition, they will likely form larger flocs which settle more quickly (Long *et al.* 2004; Casas *et al.* 2019). Finally, the adhesion force may change with temperature as well. In the literature, the effect of temperature on the amount of deposition is inconclusive, with some crude oils showing an increase in deposition with temperature while other crude oils have a decrease in deposition with temperature (Kuang *et al.* 2018).
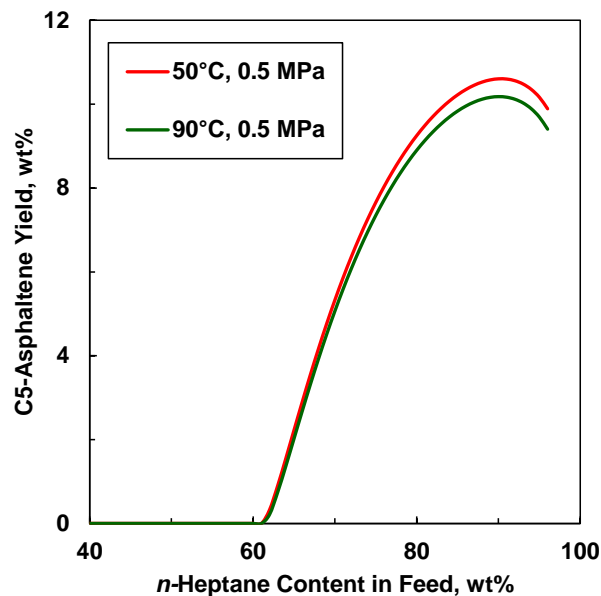
Figure 4.7 Asphaltene yields predicted by the Modified Regular Solution model at 0.5 MPa and different temperatures. The modeling is provided in Appendix A.

Figure 4.8 shows that changing the temperature while remaining in the glassy particle regime did not change the pressure drop profile. Similar results were obtained at all the solvent contents considered in this thesis. Hence, the changes in properties and forces with temperature were either too small to make an impact or cancelled each other out. Table 4.8 shows that the deposit formed at the tube inlet at both 50 and 90°C; however, the mass of the deposit increased at the higher temperature at all of the solvent contents considered in this thesis. Since the larger deposit did not alter the pressure drop, it is likely that the orifice diameter did not change significantly and that the deposit simply accumulated over a greater length of the capillary tube. The size of the deposits will be discussed later.

Table 4.9 shows that the *n*-heptane content in the deposit was lower at 90°C than at 50°C in the 65:35 H:B mixtures, indicting less porous deposits. Unlike the results at 50°C, the n-heptane content of the deposits increased for the 90:10 H:B mixtures. The reason for the changing solvent content can be attributed to experimental uncertainty since the ±7 wt% error ranges just overlap.
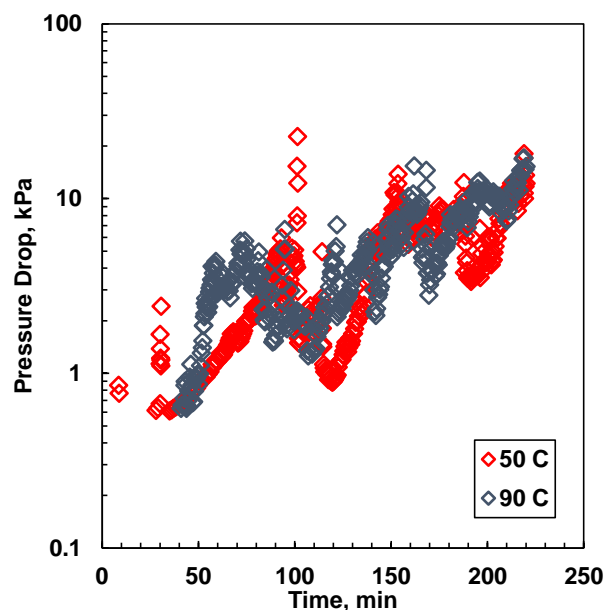
Figure 4.8 Pressure drop profile for a 65:35 H:B mixture in a 30 cm capillary tube at 2.0 cm3/min and 50 and at 2.1 cm3/min and 90°C. The uncertainty of the pressures is ±0.25 kPa.

Table 4.8: Mass distribution of dried deposits in 30 cm (1.75 mm I.D) capillary tube for a 65:35 H:B mixture at 2.0 cm^3/min and 50 and at 2.1 cm^3/min and 90°C . The uncertainty of the masses is ±6 mg.

Temperature (°C)	1st (mg)	2nd (mg)	3rd (mg)	4th (mg)	Total (mg)
50	16.9	2.4	-2.9	-3.9	12.6
90	40.2	5.7	-5.1	1.4	42.2

Table 4.9: Solvent content of deposits in a 30 cm (1.75 mm I.D) capillary tube at 2.0 cm^3/min and 50°C and at 2.1 cm^3/min and 90°C. The uncertainty of the solvent content is ±7 wt%.

H:B (w/w)	*n*-Heptane Content in Deposit (wt%)
65:35	73
75:25	73
90:10	84

4.1.6 Effect of Method of Solvent Addition

The method of solvent addition can also impact the observed deposition behavior particularly near the onset of precipitation. If the mixing is imperfect, localized regions of high solvent content can

cause local asphaltene precipitation and subsequent deposition. Figure 4.9 compares the pressure drops for two mixing methods: 1) feed a premixed 40:60 H:B mixtures into the apparatus (premix method); 2) feed *n*-heptane and a premixed 30:70 H:B mixture to obtain a 40:60 H:B mixture in the apparatus (stepwise method). There was no increase in the pressure drop above the detection limit with the premix method but a pressure drop above the limit was observed with the step-wise method indicating that some deposition occurred. Similar results were found for 50:50 H:B mixtures (not shown here). Hence, caution is required when designing and interpreting deposition experiments near the onset of precipitation. The impact of the mixing method will likely be negligible above the onset of precipitation because deposition is occurring anyway. The focus of this thesis is strictly on deposition above the onset of precipitation.
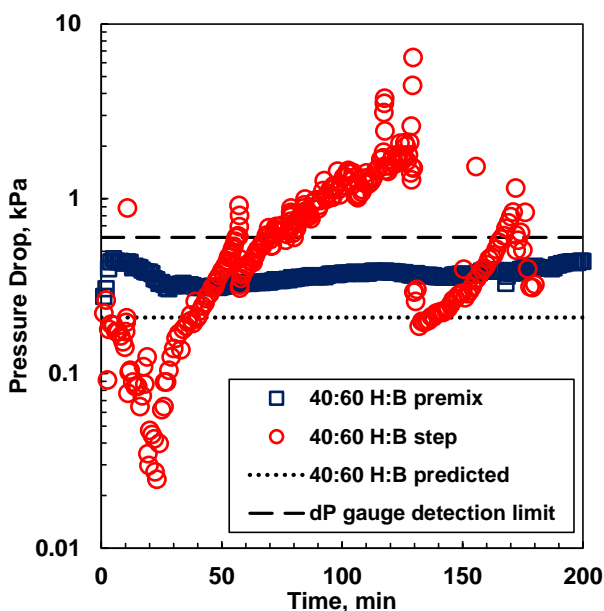
Figure 4.9 Comparison of pressure drop profiles below the onset of precipitation with premix method and stepwise solvent addition for a 40:60 H:B mixture in a 30 cm (1.75 mm I.D) capillary tube at 2.0 cm³/min and 50°C. The uncertainty of the pressures is ±0.25 kPa.

4.2 Indirect Measurements (Dimensions of Deposit and Deposition Rate)

The indirect measurements of the dimensions of the deposit and the initial mass deposition rate require some assumptions and additional calculations. Each is discussed below.

4.2.1 Size and Length of Deposit

Assuming the deposit forms an orifice-type structure, the recorded pressure drops and wet masses of the deposits can be used to calculate the size and length of the deposits using the following iterative approach. The first step is to determine the diameter of the orifice. An initial guess is made for the diameter and the velocity of the fluid is determined using the volumetric mixture flow rate. The corresponding Reynolds number is calculated as follows:

$$Re = \frac{\rho v d_o}{\mu} \tag{4.3}$$

where Re is the Reynolds number, ρ is the density of the fluid, v is the velocity of the fluid through the orifice, d_o is the diameter of the orifice, and μ is the viscosity of the fluid. The ratio of the orifice diameter and the tube diameter is then used with the Reynolds number to find the orifice discharge coefficient. Finally, the pressure drop is calculated using Equation 4.2, and the process is repeated with new values of the orifice diameter until the calculated pressure drop matches the final pressure drop. The density and viscosity of the fluid are predicted using an empirical correlation (Saryazdi *et al.* 2013) and the Expanded Fluid Viscosity Model (Ramos-Pallares *et al.* 2016) respectively. Details are provided in Appendix B.

Once the orifice diameter is known, the wet mass of the deposit is used to find the length of the deposit as follows:

$$L_{dep} = \frac{4V_{dep}}{\pi(D^2 - d_o^2)} \tag{4.4}$$

where L_{dep} is the length of the deposit, V_{dep} is the volume of the deposit, D is the diameter of the tube, and d is the diameter of the orifice. The volume of the deposit is calculated as follows:

$$V_{dep} = \frac{m_{wet\ dep}}{\rho_{dep}} \tag{4.5}$$

where $m_{wet\ dep}$ is the wet mass of the deposit, and ρ_{dep} is the density of the deposit. The density of the deposit is given by:

$$\rho_{dep} = w_{C7}\rho_{C7} + (1 - w_{C7})\rho_{non-solvent} \tag{4.6}$$

where w_{C7} is the mass fraction of *n*-heptane in the deposit, ρ_{C7} is the density of *n*-heptane, and $\rho_{non-solvent}$ is the density of the non-solvent components. The density of the deposit will first be calculated assuming the non-solvent component is asphaltenes and then assuming the non-solvent component is bitumen. This approach will generate a range for the density of the deposit as well as its length.

70

Table 4.10 shows the size and length of the deposits obtained from all experiments performed at different temperatures and solvent contents. In general, the deposit lengths are consistent with the mass profiles shown earlier in Table 4.4 and 4.8. The overall uncertainty in the length of the deposit is high (±50%) mainly due to the high uncertainty of the solvent content of the deposit. The higher wet masses with a feed of 75:25 H:B at 50°C and a feed of 90:10 H:B at 90°C and subsequently longer deposit lengths may be an artifact of incomplete drainage of residual fluid inside the capillary tubes during the cyclohexane flush stage at the end of the experiments.

Table 4.10: Mass and length of deposits in glassy particle regime in a 30 cm (1.75 mm I.D) capillary tube at a flow rate of at 2.0 cm3/min and 50°C and at 2.1 cm3/min and 90°C. The uncertainty of the deposit length is ±50%.

H:B (w/w)	Temperature (°C)	Orifice Diameter (mm)	Wet Mass of Deposit (mg)	Length of Deposit (cm)
65:35	50	0.10	111.5	6.4-6.7
65:35	50	0.11	109.0	6.4-6.6
75:25	50	0.17	67.5	4.1-4.2
75:25	50	0.07	347.0	18.7-19.8
90:10	50	0.15	163.0	8.4-9.0
65:35	90	0.10	162.0	8.7-9.4
75:25	90	0.14	79.0	4.2-4.6
90:10	90	0.13	355.0	20.7-21.8

4.2.2 Initial Deposition Rate

It is assumed that the initial 60 minutes of the deposition test can be characterized as a rapid deposition period that is relatively free of erosion. Unfortunately, the pressure drop in much of this interval was below the detection limit. In addition , since the apparatus required approximately 30 minutes to reach equilibrium during startup, it is possible that the deposit formed an orifice within this period and the buildup would not have been observed anyway. Therefore, the deposition rate was determined as the average deposition rate during the time before the first pressure drop measurement above the threshold. This average is the minimum value of the initial deposition.

The mass of the deposit was calculated as follows:

$$\dot{m}_{dep} = \frac{m(t)_{dep}}{At} \tag{4.7}$$

where $\dot{m}_{dep}$ is the deposition rate per unit area, $m(t)_{dep}$ is the estimated mass of the deposit at the time of the measurement, A is the area available for deposition, and t is the time of the pressure drop data point that are is to calculate the mass of deposit. The area available for deposition is the product of the circumference of the cross-sectional area open for flow and the deposit length. The length of the deposit is assumed to be constant at 3.0 cm because the pressure drop profiles between a 3 cm test section and a 30 cm test section were similar for the first 20 minutes as shown in Figure 4.2. The similarity confirms that the length of the deposit is no more than 3.0 cm at early times. The area open for flow and the mass of the deposit were determined using the first recorded pressure drop. First, the orifice diameter was calculated first using Eq. 4.2. The area open for flow is the cross sectional area inside the orifice diameter. The volume of the deposit was determined by rearranging Eq. 4.4 and the mass of the deposit by rearranging Eq. 4.5 and using the density from Eq. 4.6.

Table 4.11 shows the minimum initial deposition rate obtained from all experiments performed at different temperatures and solvent contents. The minimum initial deposition rate increased with solvent composition at all temperatures. As noted previously, this trends is consistent with increased adhesion forces in poorer solvent conditions. There was no consistent trend of deposition rate with temperature.

Table 4.11: Initial deposition rates in glassy particle regime in a 30 cm (1.75 mm I.D) capillary tube at a flow rate of 2.0-2.1 cm³/min.

H:B (w/w)	Temperature (°C)	Initial Deposition Rate (mg/cm²min)
65:35	50	0.86
65:35	50	0.93
75:25	50	1.14
75:25	50	1.65
90:10	50	2.39
65:35	90	0.75
75:25	90	0.82
90:10	90	2.73

4.3 Comparison with Literature Data

The overall trends in deposition behaviour obtained in this thesis are compared with literature data in the following categories: 1) pressure drop profiles; 2) deposition rates. The feed compositions are reported in terms of solvent wt% or solvent vol% as required to match the data as it was reported in the literature.

4.3.1 Pressure Drop Profiles

Hoepfner *et al.* (2013) measured pressure drops for horizontal flow of mixtures of light oil and *n*-heptane in a 0.01 inch (0.25 mm) I.D. 30 cm long capillary tube at 60°C and a constant flow rate of 5 cm³/h. Similarly, Bemani *et al.* (2019) investigated asphaltene deposition using crude oil diluted with toluene and *n*-heptane in a 1/16 inch (1.6 mm) I.D. 50 cm long capillary tube at 20°C and a constant flow rate of 0.05 cm³/min. The Reynolds number for clean tube flow in the Bemani study, the Hoepfner study, and this thesis were 0.31, 1.79, and 17 respectively.

Figure 4.10 compares the pressure drop profiles from this thesis with the profiles from these studies. All of the pressure drop profiles are qualitatively consistent. All show a rapid initial increase in pressure drop. The Hoepfner data also show a transition to steady state pressure drop similar to the data from this thesis. The literature data do not show pressure spikes but are possibly too sparse to detect them. In addition, the Reynold's number is higher in the experiments in this thesis compared with the others. It is possible that a higher Reynold's number is required to "blow out" the deposit.

Figure 4.11 shows that, consistent with the results from this thesis, both Hoepfner and Bemani found that the pressure drop profiles were independent of the length of the capillary. Hence, all of the data are consistent with an orifice-like deposit.
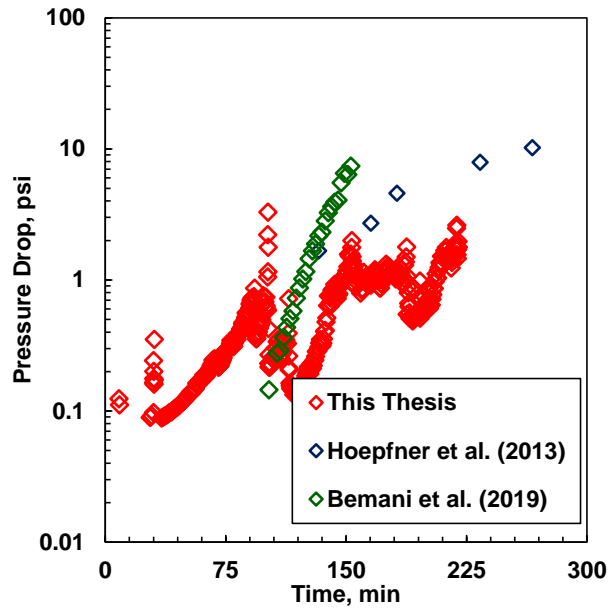
Figure 4.10 Comparison of pressure drop profiles with this thesis (74 vol% *n*-heptane and 26 vol% bitumen feed with 30 cm tube) with data from the literature. Data from Hoepfner *et al.* (2013) (30 vol% *n*-heptane and 70 vol% light oil feed with 30 cm tube) and Bemani *et al.* (2019) (60 vol% *n*-heptane, 16 vol% toluene, and 24 vol% oil feed with 50 cm tube).
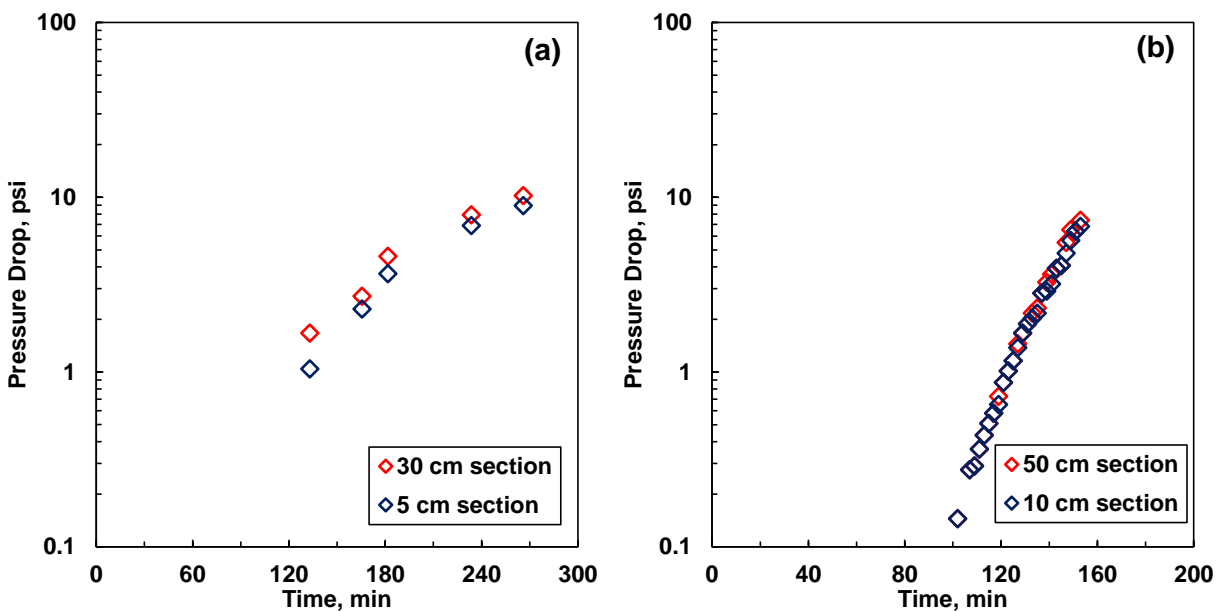
Figure 4.11 Pressure drop profiles from: a) 30 vol% *n*-heptane and 70 vol% light oil mixture from Hoepfner *et al.* (2013); b) 60 vol% *n*-heptane, 16 vol% toluene, and 24 vol% oil mixture from Bemani *et al.* (2019).

Figure 4.12a shows the pressure drop profile for mixtures of light oil and *n*-heptane with different solvent contents (vol%) in asphaltene deposition experiments at 60°C and a constant flow rate of 5 cm³/h reported by Hoepfner *et al.* (2013). Increasing the solvent composition causes the pressure drop to increase more rapidly, consistent with the trends obtained in this thesis. The pressure drop profiles from this thesis are shown in Figure 4.12b.
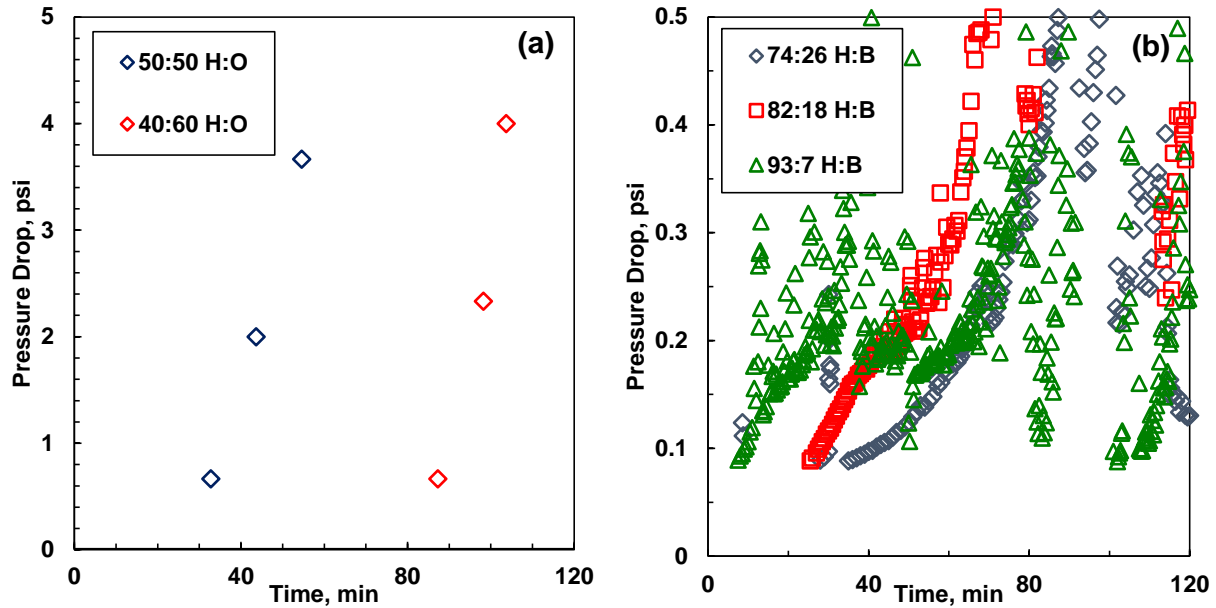
Figure 4.12 Comparison of pressure drop profiles at different solvent content (vol%) from a) Hoepfner *et al.* (2013); b) this thesis. The magnitudes of the pressure drops in the figures are different because the data were reported at different durations of the pressure buildup from deposition.

In addition, Hoepfner *et al.* (2013) found that the pressure drop profile consolidated into a single curve when the pressure drop was divided by the viscosity and insoluble asphaltene concentration of the mixture as shown in Figure 4.13a. The common trend suggests that settling rates and the particle concentration are significant factors in the deposition rate. However, the data do not extend past the maximum in the particle concentration. The same procedure was applied to the data in this thesis and the results are shown in Figure 4.13b. In this case, the data below the maximum in particle concentration do appear to collapse onto a single curve. However, the deposition rate continues to increase above the maximum (>82 vol% *n*-heptane). Therefore, it is not solely the

particle concentration that governs the deposition rate. The effect of the solvent on the adhesion forces must also be accounted for.
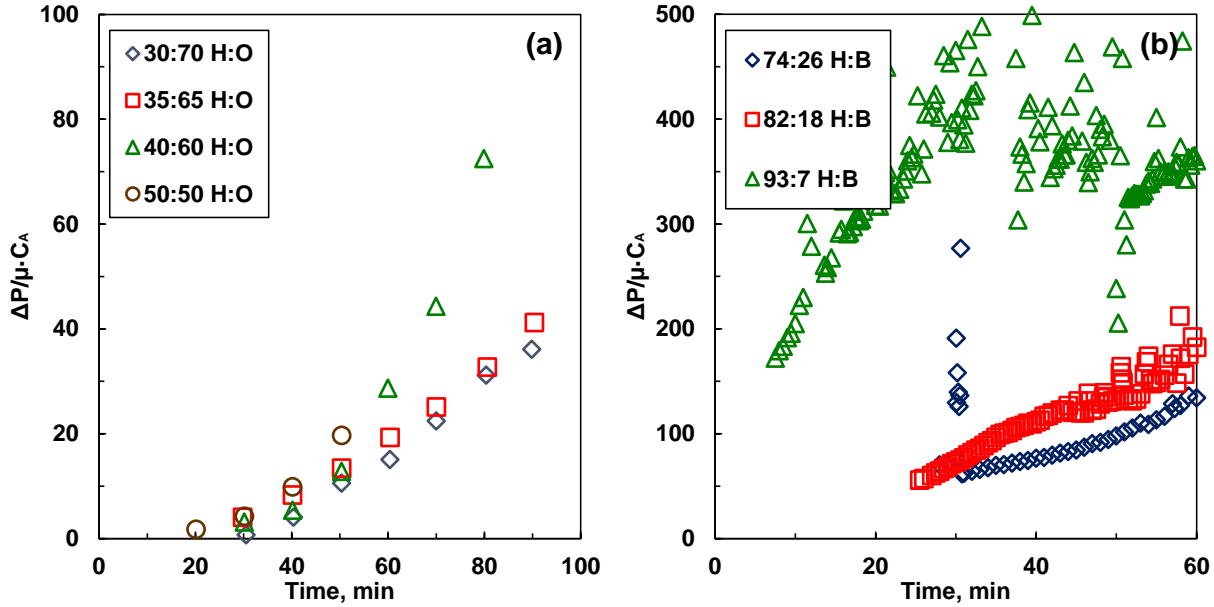
Figure **4.13** Comparison of normalized pressure drop profile at different solvent content (vol%) from a) Hoepfner *et al.* (2013); b) this thesis.

4.3.2 Deposition Rates with Different Solvent Content

Vilas Bôas Fávero *et al.* (2016) performed experiments with mixtures of light oil and *n*-heptane in a vertical glass column packed with stainless steel beads at ambient conditions under Stokes flow conditions (Re <1). The deposition rate was calculated by taking the final deposit mass at the end of each experiment and dividing it by the product of the run-time and the total surface area of the packed bed. Table 4.12 shows that the deposition rates from Vilas Bôas Fávero *et al.* were two orders of magnitude lower than those from this thesis. One possible reason for the difference is that the estimated deposit masses in this thesis are highly sensitive to the length of the deposit. Since the exact length of the deposit was unknown, a longer length could artificially inflate the deposition rate. Another possible explanation is that the deposition rates in the Vilas Bôas Fávero experiments were calculated at the end of each experiment. Initially, the asphaltene deposition rate will be high but eventually, a steady state balance will be reached between deposition and erosion and the deposition rate will decrease to zero. Therefore, the rates from Vilas Bôas Fávero *et al.*

may be lower than the initial deposition rates. Nonetheless, in both cases, the deposition rates increased with an increase in the feed *n*-heptane content.

Table 4.12: Comparison of deposition rates at different solvent contents estimated in this thesis and literature values.

H:B (w/w)	Source	Deposition Rate (mg/cm²min)
28:72	Vilas Bôas Fávero *et al.* (2016)	0.0010
30:70	Vilas Bôas Fávero *et al.* (2016)	0.0013
31:69	Vilas Bôas Fávero *et al.* (2016)	0.0017
33:67	Vilas Bôas Fávero *et al.* (2016)	0.0024
65:35	This Thesis	0.86
65:35	This Thesis	0.93
75:25	This Thesis	1.14
75:25	This Thesis	1.65
90:10	This Thesis	2.39

4.4 Summary

At all the experimental conditions considered in this thesis, the pressure drop profiles initially increased approximately exponentially over time indicating that the precipitated asphaltenes were depositing. The pressure drop eventually transitioned to a constant value consistent with a steady balance between deposition and erosion. There were occasional sharp drops in the differential pressure suggesting that the deposit were occasionally partially blown out.

The pressure drop profiles in different length capillary tubes were similar, indicating that the deposit was localized rather than evenly spread over the tube. The mass distribution profiles from the capillary tube cuttings showed that the deposit formed at the inlet. The deposits were also highly porous (solvent content of 70-90 wt%).

The deposition rate increased as solvent content in the feed increased. The increase correlated to the solvent content rather than the precipitated particle concentration. Hence, the increase appears to be caused by an increased attraction between asphaltene molecules and the tube surface. The

amount of deposition also increased at higher temperatures, where the deposit maintained its orifice-like structure but grew along the length of the tube.

In general, the trends observed in this thesis were consistent with the literature. Hence, the apparatus was considered to be validated and suitable for use in investigating asphaltene deposition at higher temperatures.

Chapter 5: Results and Discussion: Liquid Heavy Phase Regime

This chapter presents the results from deposition experiments of a bitumen and *n*-heptane system at 130°C where asphaltenes precipitate as a liquid. First, the measured pressure drop, deposit mass, and *n*-heptane content are presented for one run. These data are analyzed to identify the deposition mechanism. Then, the effects of the *n*-heptane content and capillary tube length are discussed.

5.1 Typical Deposition Experiment

5.1.1 Modeling Pressure Drop Profiles

Figure 5.1a and 5.1b shows the pressure drop profiles for mixtures containing 75 wt% *n*-heptane and 25 wt% bitumen (75:25 H:B) in 30 cm long capillary tubes. The experiments were performed at 130°C and a flow rate of 2.2 cm³/min. Figure 5.1a shows that there was initial sharp increase in the pressure drop indicating the start of the deposition process. The pressure drop continued to increase slowly over time until approximately 100 minutes where the pressure drop increased exponentially for 40 minutes and then fell rapidly to the pressure drop observed just before the exponential growth. The cycle of exponential growth and rapid decline repeated at intervals of approximately 40 minutes. Figure 5.1b shows that the behavior up to 75 minutes was repeatable. This run was terminated at 75 minutes so that the mass in the capillary tube before the exponential growth in pressure drop could be measured.

Table 5.1 shows the mass distribution of the recovered material along the test section for both experiments after the tube was dried and cut into four equal segments. In the shorter experiment, the recovered mass was small and concentrated in the second segment of the tube. The *n*-heptane content of the recovered mass was 68 wt%. For the longer experiment, the mass was measured at the end of the exponential growth period. The recovered mass was much higher than the mass at 70 minutes and was uniformly distributed along the length of the tube. The *n*-heptane content of the recovered mass was 42 wt%. Even on a dry basis, this mass would occupy 54% of the tube volume. At an *n*-heptane content of 42 wt%, it would occupy 94% of the tube volume.
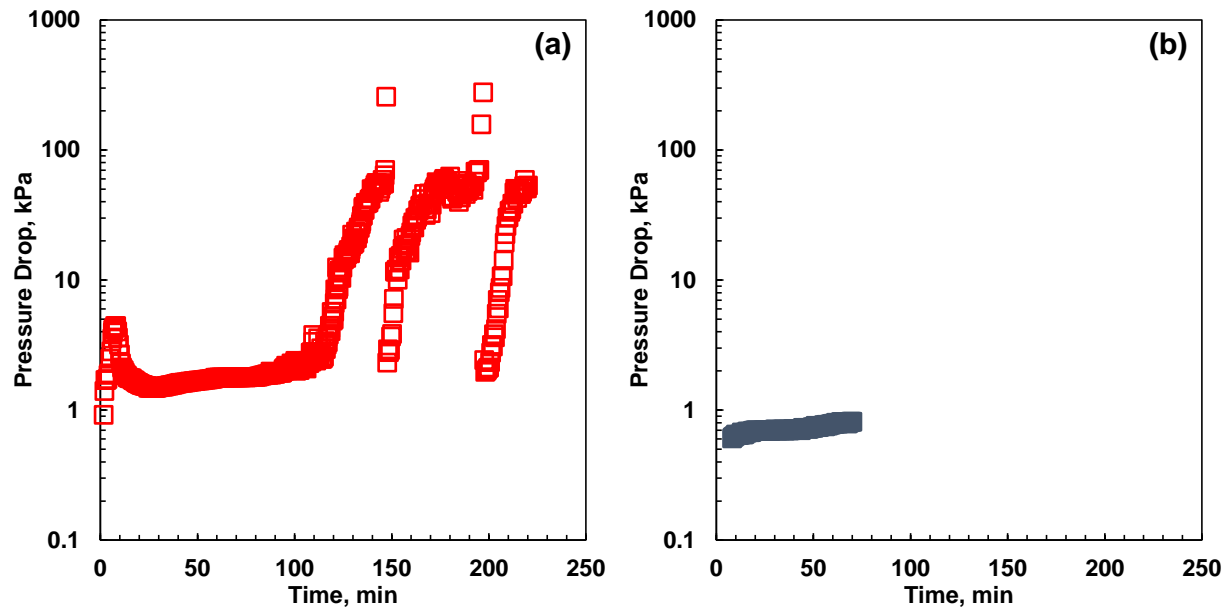
Figure 5.1 Pressure drop profile for 75:25 H:B mixtures at 130°C and 2.2 cm³/min in a 30 cm (1.75 mm I.D) capillary tube with different experimental runtimes: a) 220 minutes; b) 70 minutes. The uncertainty of the pressures is ±0.25 kPa.

Table 5.1: Mass distribution of dried recovered material in a 30 cm (1.75 mm I.D) capillary tube for a 75:25 H:B feed at 2.2 cm³/min at 130°C. The uncertainty of the masses is ±6 mg.

Experimental Run Time (min)	1st (mg)	2nd (mg)	3rd (mg)	4th (mg)	Total (mg)
220	73	85	88	85	330
70	3	10	4	3	20

The initial rapid increase in pressure drop with a small volume of deposit suggests that an obstruction formed and created an orifice effect even though the heavy phase was a liquid. The formation of an obstruction is plausible because the heavy phase contains a significant fraction of asphaltenes (Johnston *et al.* 2017a) and likely has a high viscosity. This deposit had a relative high *n*-heptane content, suggesting there was some entrainment of *n*-heptane within the deposit. In other words, the obstruction consisted of partially coalesced liquid droplets.

At the same time, it appears that a layer of heavy phase droplets settled and accumulated vertically, likely creating a stratified flow regime. Another possibility is the heavy phase accumulated as a

front progressively accumulating along the pipe but this explanation does not match the data as discussed in Appendix D. Eventually, the accumulated layer of heavy phase occupied enough of the tube to affect the pressure drop (start of exponential growth period). At some point with the increasing velocity in the more confined light phase, the flow likely transitioned to stratified wavy flow. The reason that this flow became unstable is unknown. It is possible that when the heavy phase occupied enough of the tube volume, the tube may have plugged; for example, when a wave crest of viscous heavy phase touched the top of the tube. The plug may have caused a pressure pulse that blew a significant fraction of the heavy phase out of the tube. The heavy phase layer then regrew and the cycle repeated itself. The *n*-heptane content of this accumulated heavy phase (42 wt% *n*-heptane) is consistent with heavy phase compositions reported in phase behavior experiments performed with mixtures bitumen and *n*-pentane (Johnston *et al.* 2017a).

5.1.2 Modeling Pressure Drop Profiles

A simplified model based on stratified flow was proposed to model the later pressure drop behaviour. The following assumptions were made:

- A fraction of the heavy phase entering the tube settles and accumulates,
- The settled heavy phase restricts the flow area for the light phase,
- The pressure drop can be determined by considering the light phase as a single liquid flowing through an effective tube diameter based on the restricted flow area (interfacial effects are neglected),
- The light phase is assumed to behave as a slurry.

First, the amount of bitumen partitioning to the heavy phase at 130°C and 0.5 MPa was calculated using the Modified Regular Solution model (see Appendix A). Figure 5.2 shows the predicted bitumen yield where yield is defined as the mass of bitumen in the heavy phase divided by the mass of bitumen in the feed.
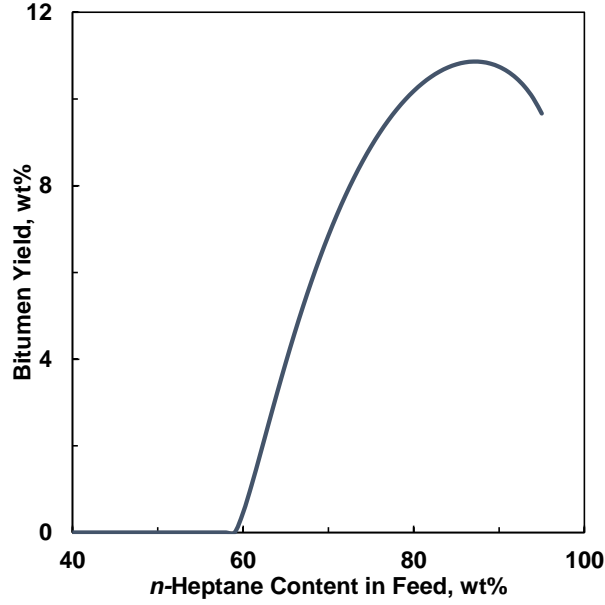
Figure 5.2 Bitumen yields predicted by the Modified Regular Solution model at 0.5 MPa and 130°C.

Next, the heavy phase mass flow rate is calculated as follows:

$$\dot{m}_{bit}^{H} = w_{bit} Y_{bit} \rho_{mix} Q_{feed} \tag{5.1}$$

where $\dot{m}_{bit}^{H}$ is the bitumen flow rate in the heavy phase, w_{bit} is the mass fraction of bitumen in the mixture, Y_{bit} is the bitumen yield, ρ_{mix} is the density of the mixture, and Q_{feed} is the total feed flow rate. The total mass of the heavy phase inside the tube at any given time is given by:

$$m_{k}^{H} = m_{k-1}^{H} + \frac{\xi_k \dot{m}_{bit}^{H} \Delta t}{(1 - w_{C7\,dep})} \tag{5.2}$$

where m_{k}^{H} is the mass of heavy phase inside the tube at time step k, ξ_k is the fraction of heavy phase that accumulates during the time step, Δt is the time-step of the calculation, and $w_{C7\,dep}$ is the mass fraction of n-heptane in the deposit. ξ_k is unknown and is used as a fitting parameter.

The volume occupied by the heavy phase is given by:

$$V_{k}^{H} = \frac{m_{k}^{H}}{\rho^{H}} \tag{5.3}$$

where V_{k}^{H} is the volume of the heavy phase at time step k and ρ^{H} is the density of the heavy phase. Since it was assumed the heavy phase was uniform along the length of the tube, the cross-sectional area occupied by the heavy phase, its height, and its perimeter could be determined using geometric

82

calculations. Similarly, these parameters could be determined for the light phase. Details of the geometric relations can be found in Appendix C. The hydraulic diameter the light phase flows through can be calculated as follows:

$$D_h^L = \frac{4A^L}{P^L} \tag{5.4}$$

where D_h^L is the hydraulic diameter of the light phase, A^L is the area occupied by the light phase, and P^L is the perimeter of the light phase. The hydraulic diameter of the light phase was also used in the Reynold's number calculation to confirm fluid flow remained in the laminar regime. In all cases considered in this chapter, the Reynold's numbers were < 250. Finally, the pressure drop across the tube is given by:

$$\Delta P = \frac{128\mu_{sl}Q_{feed}L}{\pi D_h^{L^4}} \tag{5.5}$$

where ΔP is the pressure drop across the capillary tube, μ_{sl} is the viscosity of the slurry, and L is the length of the capillary tube. The viscosity of the slurry is calculated from the Einstein's viscosity equation:

$$\frac{\mu_s}{\mu} = 1 + \frac{5}{2}\varphi \tag{5.6}$$

where μ is the viscosity of the feed mixture, and φ is the volume fraction of the heavy phase. The viscosity of the feed mixture was determined from the Expanded Fluid Viscosity Model (see Appendix B). The heavy phase volume fraction was calculated as follows:

$$\varphi = \frac{\dot{m}_{bit}^H}{(1-w_{C7\ dep})\rho^H Q_{feed}} \tag{5.7}$$

Figure 5.3a shows fractional heavy phase accumulation (ξ) used to obtain the fit the pressure drop data. Figure 5.3b shows the fitted pressure drops and Figure 5.3c shows the calculated heavy phase holdup. The initial fractional accumulation of 0.09 and is the average fractional accumulation for the first 100 minutes. The fractional accumulation decreased at later times, likely because the light phase velocity increased. A higher light phase velocity gives less time for settling and potentially increases liquid entrainment.

The early pressure drops could not be matched because they were created by the orifice-like deposit rather than the stratified flow. The calculated liquid hold up at the end of the exponential growth period was 0.95 (0.578 g) compared with a measured value of 0.94 (0.573 g), giving an

absolute relative deviation of 1.0%. Although the model is simplified, it confirms that the measurements are consistent with an accumulation of the heavy phase during stratified flow.
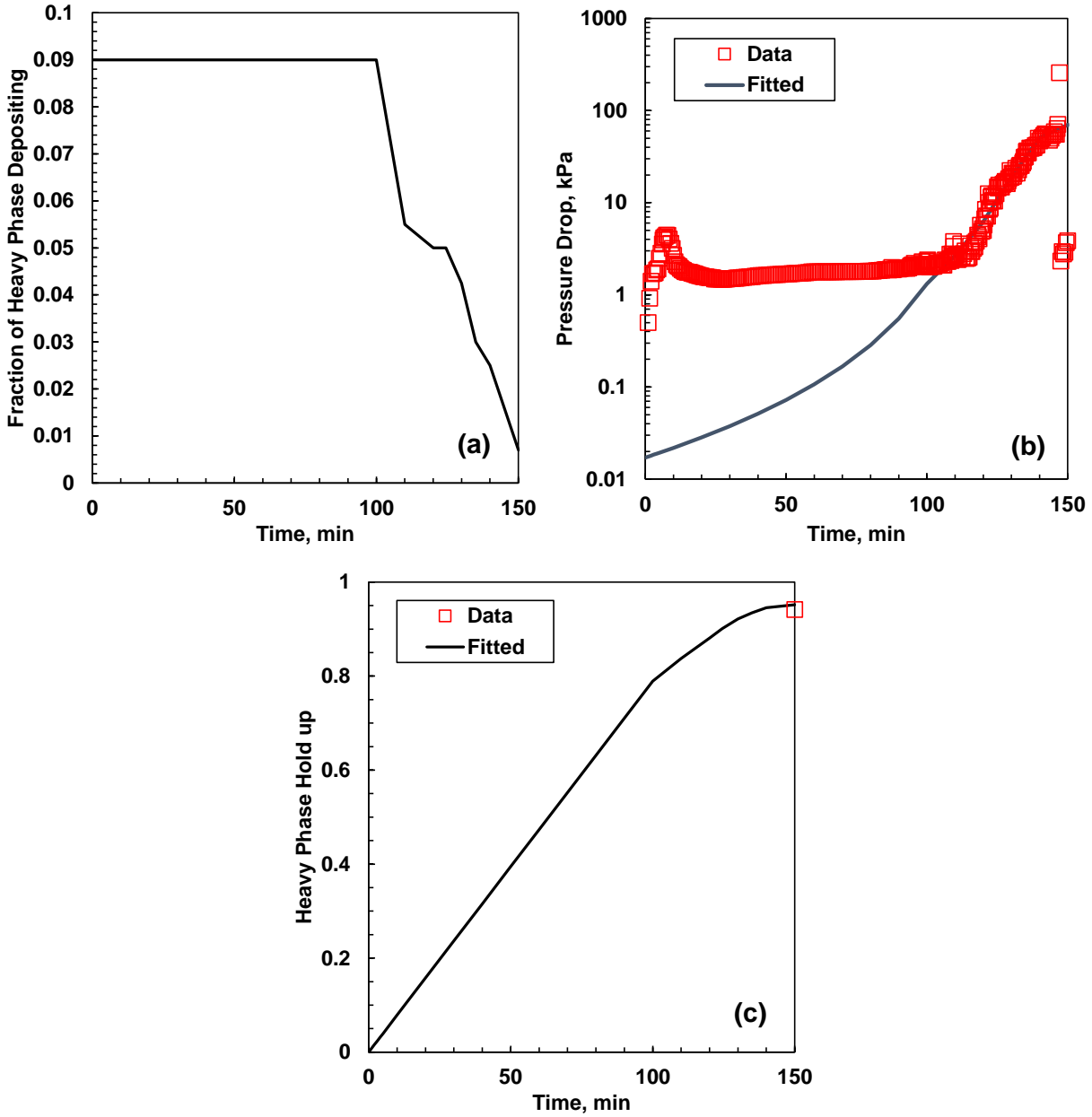
Figure 5.3 Heavy phase accumulation modeling results for a 75:25 H:B mixture at 130°C and 2.2 cm³/min in a 30 cm (1.75 mm I.D) capillary tube.: a) fitted fractional heavy phase deposition, b) pressure drop; c) heavy phase hold up.

5.2 Effect of *n*-Heptane Content in the Feed

<u>Measurements</u>

Figure 5.4 shows the pressure drop profile of the experiments at three different *n*-heptane contents. There was no initial rapid increase in pressure drop with the 90:10 and 65:35 H:B feeds; that is, no evidence of an orifice-like deposit forming. It is not clear why the orifice-like deposit only formed with the 75:25 H:B feed. This feed had the highest heavy phase fraction of the three feeds. Perhaps a threshold heavy phase concentration is required to form an orifice-like deposit in the liquid heavy phase regime.
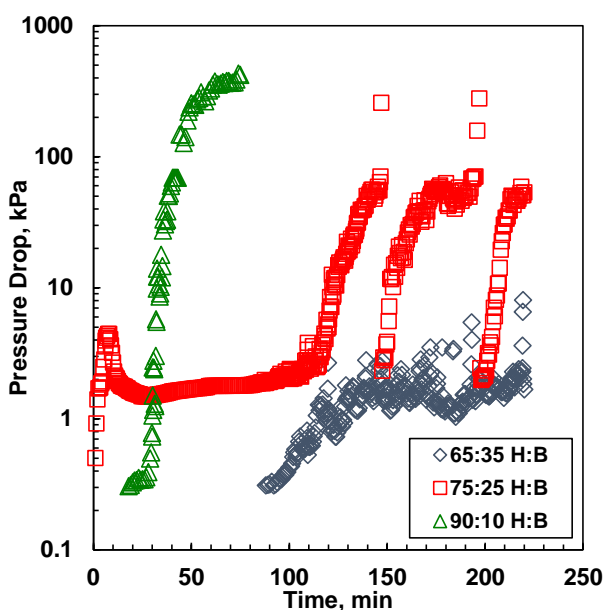
Figure 5.4 Effect of feed composition on the pressure drop profile in a 30 cm (1.75 mm I.D) capillary tube at 130°C and 2.2 cm³/min. The uncertainty of the pressures is ±0.25 kPa.

The later exponential increase in pressure drop first occurred at approximately 30 minutes for the 90:10 H:B feed, 100 minutes for 75:25 H:B, and not at all for the 65:35 H:B. In other words, the higher the *n*-heptane content, the more rapidly the heavy phase accumulated. The 65:35 H:B feed had increasing fluctuations in the pressure drop at later times, but it appears that the heavy phase buildup occurred too slowly have a significant effect within the timeframe of the experiment. The accumulation rate correlates to the *n*-heptane content rather than the mass fraction of heavy phase in the feed which peaks at 75 wt% *n*-heptane. The higher accumulation rate could be caused by

more rapidly settling or greater cohesive forces between the droplets leading to more rapid coalescence.

Table 5.2 shows the mass distribution of the deposit along the capillary tube at the three different feed *n*-heptane contents. The absolute masses for the deposits increased with *n*-heptane content at all of the *n*-heptane contents considered in this thesis. In addition, the masses are uniformly distributed along the length of the tube in both the 75:25 H:B and 90:10 H:B runs whereas localized deposits were formed in the 65:35 H:B runs. These observations are consistent with the earlier interpretation that the heavy phase buildup has not occurred yet in the 65:35 H:B run, and that the deposit starts developing in a localized region, typically at or near the inlet.

Table 5.3 shows that the *n*-heptane content of the deposit decreases as the *n*-heptane content in the feed increases. In other words, the deposits appear to be more compact and there is less *n*-heptane entrainment at higher *n*-heptane contents in the feed. The high *n*-heptane content in deposit of the 65:35 H:B runs is consistent with an orifice-like deposit of partially coalesced droplets. The lower *n*-heptane content in the other runs is consistent with greater cohesion and coalescence.

Table 5.2: Effect of feed composition on the mass distribution of dried recovered material in a 30 cm (1.75 mm I.D) capillary tube at 2.2 cm³/min and 130°C. The uncertainty of the masses is ±6 mg.

H:B (w/w)	1st (mg)	2nd (mg)	3rd (mg)	4th (mg)	Total (mg)
65:35	34	8	15	-5	52
65:35	30	7	0	8	44
75:25	73	85	88	85	330
90:10	86	114	117	99	416

Table 5.3: Effect of feed composition on *n*-heptane content of deposits in a 30 cm (1.75 mm I.D) capillary tube at 2.2 cm³/min and 130°C.

H:B (w/w)	*n*-Heptane Content of Deposit (wt%)
65:35	69
65:35	88
75:25	42
90:10	28

Modeling

Since the heavy phase buildup was not observed in the 65:35 H:B run, only the pressure drops for the 90:10 H:B run were modeled. Figure 5.3a, 5.3b, and 5.3c show the tuned fractional heavy phase accumulation (ξ), fitted pressure drops, and calculated heavy phase holdup, respectively. The initial average fractional accumulation was 0.80 much higher than the 0.09 value for the 75:10 H:B system. The higher fractional accumulation is consistent with more rapid settling and coalescence. The calculated liquid hold up at the end of the exponential growth period was 0.98 (0.66 g) compared with a measured value of 0.86 (0.58 g), giving an absolute relative deviation of 13.9%.
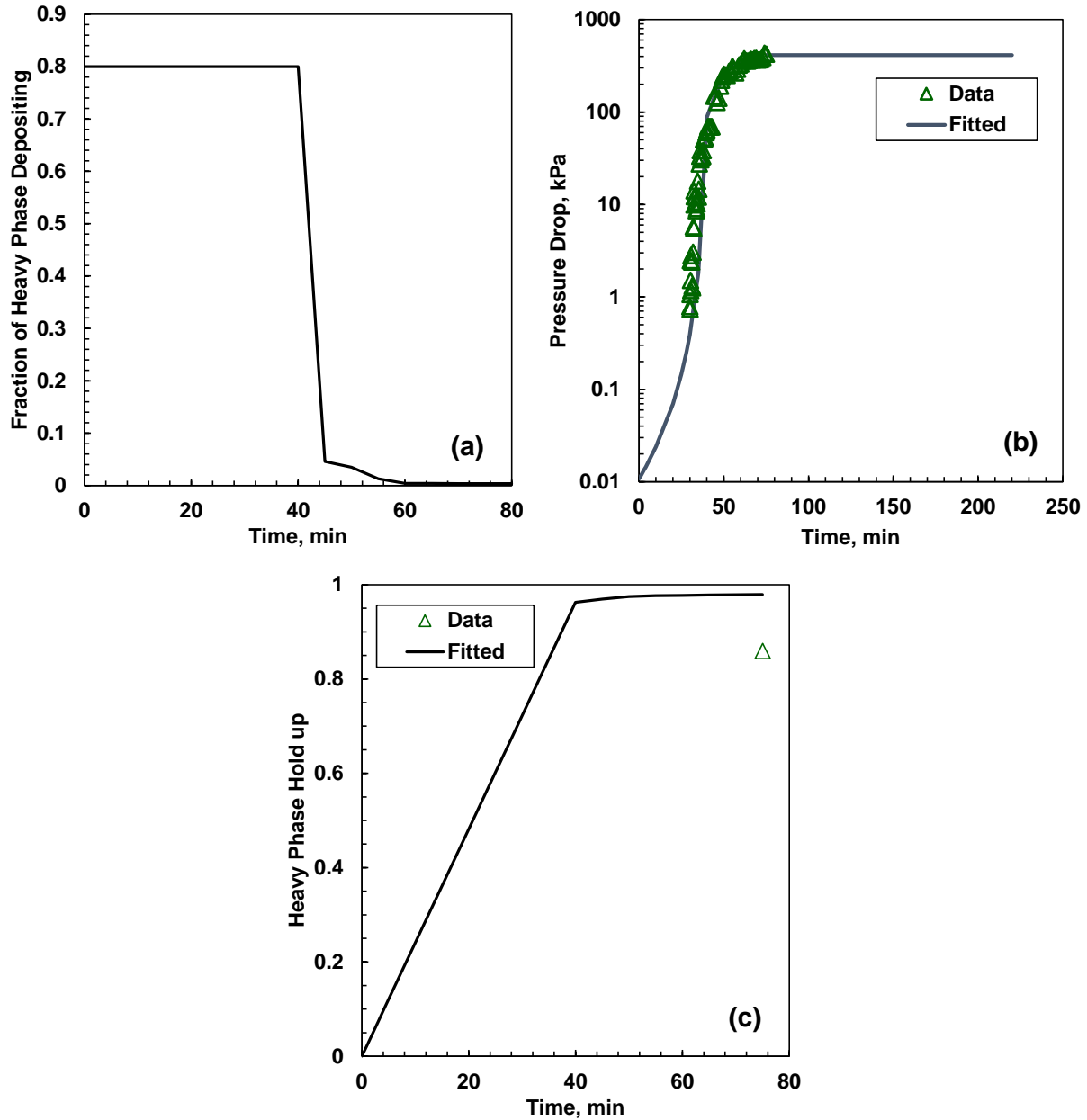
Figure 5.5 Heavy phase accumulation modeling results for a 90:10 H:B mixture at 130°C and 2.2 cm³/min in a 30 cm (1.75 mm I.D) capillary tube.: a) fitted fractional heavy phase deposition, b) pressure drop; c) heavy phase hold up.

5.3 Effect of Capillary Tube Length

In the previous section, it was shown that the asphaltenes formed a uniform deposit along the length of the tube in the 75:25 and 90:10 H:B runs at 130°C. Therefore, unlike the orifice deposits that formed at lower temperatures, the pressure gradient at 130°C is expected to be uniform along

the tube and the pressure drop proportional to the tube length. Figure 5.6a shows the pressure drop profiles for a 90:10 H:B feed with three different tube lengths and Figure 5.6b shows the pressure gradient (pressure drop divided by tube length) as a function of time. In all three cases, the flow is fully developed (entrance length = 0.7 cm). For both the 16.5 and 3 cm runs, there are periodic fluctuations in the pressure drop that indicate cycles of heavy phase removal from the tube.

In the runs with the 16.5 and 30 cm tubes, the pressure gradients increased with time as the heavy phase layer accumulated. The pressure gradients for the two runs are almost identical over time indicating that the liquid holdup developed similarly in both cases as would be expected with the accumulation of a uniform heavy phase layer along the length of the tube. Table 5.4 confirms that a uniform layer was formed and that the mass of the layer was proportional to the tube length. In other words, the holdup at the end of the exponential growth period was the same in both cases (0.98 and 0.98 for the 16.5 and 30 cm tube, respectively). Table 5.5 shows that the n-heptane content of the deposits were similar for the two runs. The n-heptane content of approximately 30 wt% is again consistent with the phase equilibrium measurements from Johnston *et al.* (2017a).

The run with the 3 cm tube behaved differently. The initial buildup of pressure was consistent with the formation of an orifice. The exponential growth associated with the buildup of a heavy phase layer occurred later than the other runs. It is not known why the heavy phase buildup was delayed in this case. This run was terminated shortly after the heavy phase had been displaced from the tube. Hence, the recovered heavy phase mass is lower than the other runs, as shown in Table 5.4. The 3 cm capillary tube was not cut into segments because it was too short to do so. The n-heptane content of the deposit is not reported because the drying curve obtained in this case lacked measurements at the relevant drying times.
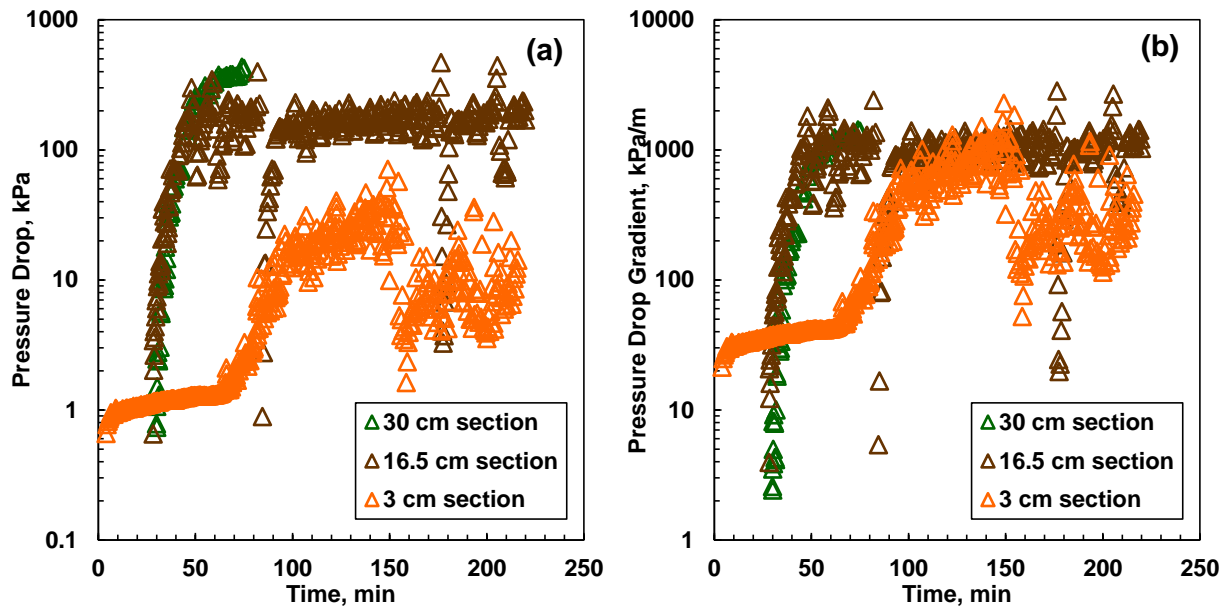
Figure 5.6 Pressure drop profile (a) and pressure drop gradient profile (b) for a 90:10 H:B feed at 130°C and 2.17 cm³/min with different test section lengths. The uncertainty of the pressures is ±0.25 kPa.

Table 5.4: Mass distribution of dried recovered material for a 90:10 H:B mixture in a (1.75 mm I.D) capillary tube at 2.2 cm³/min and 130°C with varying test section lengths. The uncertainty of the masses is ±6 mg.

Test Section Length (cm)	1st (mg)	2nd (mg)	3rd (mg)	4th (mg)	Total (mg)
3	-	-	-	-	16
16.5	42	50	60	64	216
30	86	114	117	99	416

Table 5.5: Effect of test section length on the *n*-heptane content of deposits for a 90:10 H:B mixture in a (1.75 mm I.D) capillary tube at 2.2 cm³/min and 130°C.

Test Section Length (cm)	*n*-Heptane Content of Deposit (wt%)
3	-
16.5	33
30	28

5.4 Summary

At 130°C, the asphaltenes precipitated in a heavy liquid phase that appeared to form a deposit in a localized section near the inlet and at the same time formed a vertically accumulating flowing layer along the length of the tube. The heavy phase layer contained as little as 30 wt% n-heptane (depending on the conditions and time), consistent with equilibrium heavy phase compositions reported in the literature (Johnston *et al.* 2017a). Only a fraction of the heavy phase joined this layer during its residence time in the tube and the rest remained dispersed in the light phase. The flow regime was interpreted as stratified flow of a light phase slurry over a heavy phase viscous liquid. The pressure gradients in different length capillary tubes were similar consistent with stratified flow as opposed to an orifice-like deposit.

The heavy phase accumulated over time and caused an exponential increase in the pressure drop until the liquid hold up was approximately 98%. At this point, the flow became unstable, likely temporarily plugging the tube until much of the heavy phase layer was rapidly displaced from the tube. The cycle of heavy phase accumulation and blow out then repeated.

The heavy phase layer accumulated more rapidly as the n-heptane content in the feed increased and the n-heptane content of the deposits decreased. These trends are consistent with more rapid settling and coalescence at higher n-heptane contents in the feed. The attractive interaction forces between the heavy phase liquid droplets are expected to become stronger as the n-heptane content of the continuous phase increases.

In summary, the deposition mechanism at 130°C where asphaltenes precipitate as liquid droplets is significantly different from at lower temperatures when asphaltenes precipitate as glassy particles. The trends observed in this chapter are a preliminary study of asphaltene deposition at higher temperatures and recommendations for further investigation in understanding the heavy phase deposition behaviour are discussed in Chapter 6.

Chapter 6: Conclusions and Recommendations

The main objectives of this thesis were to: 1) design, build, and commission an apparatus to investigate asphaltene deposition in capillary tube flow for temperatures up to 130°C; 2) measure the pressure drop profiles, mass of deposit, and solvent content of deposit in deposition experiments for different capillary tube lengths, solvent contents in the feed, flow rates, and temperatures; 3) identify the deposition mechanism at different temperatures. This chapter summarizes contributions and findings of this thesis and recommendations for future work in the area.

6.1 Contributions and Conclusions

New Apparatus

The first contribution from this thesis was the construction and commissioning of an apparatus to analyze asphaltene deposition at temperatures up to 130°C in capillary flow based on pressure drop and mass measurements in a *n*-heptane diluted bitumen system. In this apparatus, pre-diluted bitumen and additional *n*-heptane are fed through a static mixer to induce asphaltene precipitation. Next, the mixture is horizontally displaced through a 1.75 mm ID capillary tube (the test section). The pressure drop across the tube is monitored during the flow period for indications of deposition. At the end of each experiment, the capillary tube is removed from the apparatus and its mass is monitored over time to determine the solvent content of the deposit and the dry mass of the deposit. The location of the deposits is also determined by cutting the tube into segments.

As part of the commissioning, it was demonstrated that the bitumen and solvent were well mixed at the exit of the static mixer. This conclusion was reached because asphaltene yields from the static mixer exit matched asphaltene yields from an independent bench top procedure at a given contact time.

In addition, a procedure was developed to wash the continuous phase from the capillary tube after the experiment with cyclohexane without disturbing the deposit. In control runs with no deposition, the cyclohexane flush method was observed to leave the smallest residual dry mass compared to other flush methods (gravity drainage and nitrogen flush), thus confirming its ability to remove

free liquid. Similar deposit masses were obtained for runs with different flush methods (gravity drainage and cyclohexane wash) after accounting for the residual masses from non-deposit material. This consistency confirms that the cyclohexane wash did not displace the deposit.

Deposition Measurements and Observations

The main contributions from the deposition experiments were:

6. The measurement of pressure drop profiles and deposit masses for mixtures of Western Canadian bitumen and *n*-heptane in a 1.75 mm ID capillary tube with different tube lengths (3, 15, 16.5, and 30 cm), feed solvent compositions (65, 75, and 90 wt% *n*-heptane), flow rates (2 and 4 cm^3/min) and temperatures (50℃, 90℃, and 130℃).

7. The confirmation that, in the glassy particle and glass transition regime (temperature below approximately 130°C for this system), the asphaltenes form an orifice-like deposit near the inlet of the test section; that is, either near where they first precipitate or at the first region of flow disturbance. Similar deposits have been reported in the literature (Seifried *et al.* 2013b; Hoepfner *et al.* 2013a; Bemani *et al.* 2019).

8. The demonstration that deposition mechanisms in open flow may change significantly with changes in asphaltene morphology; that is, at temperatures above the glass transition. When the asphaltene-rich phase is fully liquid, a periodically unstable stratified flow regime develops. In some cases, an orifice-like deposit near the inlet may also occur.

Some additional conclusions are as follows:

1. Below the onset of precipitation, a premixed feed of bitumen and solvent produced no indications of deposition. However, when bitumen and solvent were fed through a static mixer, local high solvent zones resulted in local asphaltene precipitation and consequent deposition. Therefore, any data collected below the onset of precipitation are suspect.

2. In the glassy particle regime, the pressure drop measurements showed rapid initial deposition followed by a balance between deposition and erosion. Intermittently, sudden peaks in the differential pressure suggested temporary blockage of the capillary tube before a sharper decline resulted in a partial blowout of the deposit. Similar pressure drop profiles were obtained between different length capillary tubes, indicating local deposition. This

conclusion was confirmed through mass measurements from capillary tube segments. The orifice-like deposits at these conditions were highly porous with a high solvent content.

3. In the glassy particle regime, the deposition rate was controlled by solvent content in the feed instead of the precipitated particle concentration. A higher solvent composition in the feed results in more attraction between asphaltene molecules and the tube surface.

4. In the liquid droplet regime, the pressure drop gradients were similar in capillary tubes of different lengths, indicating the accumulation of a uniform heavy phase layer. The solvent content of the heavy phase was lower compared to glassy particle deposits and consistent with equilibrium heavy phase compositions reported in the literature.

5. In the liquid droplet regime, a higher solvent content in feed caused the heavy phase liquid to settle and coalesce faster. The heavy phase accumulation rate was enhanced at higher solvent compositions.

6.2 Recommendations

Recommendations for future studies are provided below:

1. Modify the experimental procedure to shorten the amount of time the apparatus needs to equilibrate during start-up. This modification will allow a more accurate estimate of the initial asphaltene deposition rates.

2. Adapt the asphaltene deposition apparatus to evaluate asphaltene deposition in vertical flow. With the capillary tube in a vertical configuration, it would be possible to study asphaltene deposition in a flow configuration closer to offshore field conditions.

3. Modify existing/develop a new deposition model to account for the changes in deposition mechanisms and flow behaviour when asphaltenes are undergoing glass transition or in the liquid regime.

4. Measure the viscosity of the asphaltene-rich heavy phase in the liquid regime.

5. Measure the adhesion forces between the asphaltene-rich heavy phase and metal surfaces and between the same phase and asphaltene coated surfaces.

References

Abraham, T., Christendat, D., Karan, K., Xu, Z., and Masliyah, J. (2002). Asphaltene - Silica interactions in aqueous solutions: Direct force measurements combined with electrokinetic studies. *Industrial and Engineering Chemistry Research*, *41*(9), 2170–2177. https://doi.org/10.1021/ie0107690

Abudu, A., and Goual, L. (2009). Adsorption of crude oil on surfaces using quartz crystal microbalance with dissipation (QCM-D) under flow conditions. *Energy and Fuels*, *23*(3), 1237–1248. https://doi.org/10.1021/ef800616x

Agrawal, P., Schoeggl, F. F., Satyro, M. A., Taylor, S. D., and Yarranton, H. W. (2012). Measurement and modeling of the phase behavior of solvent diluted bitumens. *Fluid Phase Equilibria*, *334*, 51–64. https://doi.org/10.1016/j.fluid.2012.07.025

Agrawala, M., and Yarranton, H. W. (2001). An asphaltene association model analogous to linear polymerization. *Industrial and Engineering Chemistry Research*, *40*(21), 4664–4672. https://doi.org/10.1021/ie0103963

Akbarzadeh, K., Alboudwarej, H., Svrcek, W. Y., and Yarranton, H. W. (2005). A generalized regular solution model for asphaltene precipitation from n-alkane diluted heavy oils and bitumens. *Fluid Phase Equilibria*, *232*(1–2), 159–170. https://doi.org/10.1016/j.fluid.2005.03.029

Akbarzadeh, K., Eskin, D., Ratulowski, J., and Taylor, S. (2012). Asphaltene deposition measurement and modeling for flow assurance of tubings and flow lines. *Energy and Fuels*, *26*(1), 495–510. https://doi.org/10.1021/ef2009474

Alboudwarej, H., Akbarzadeh, K., Beck, J., Svrcek, W. Y., and Yarranton, H. W. (2003). Regular Solution Model for Asphaltene Precipiation from Bitumens and Solvents. *AIChE Journal,* 59(11), 2948-2956.

Alboudwarej, H., Pole, D., Svrcek, W. Y., and Yarranton, H. W. (2005). Adsorption of asphaltenes on metals. *Industrial and Engineering Chemistry Research*, *44*(15), 5585–5592. https://doi.org/10.1021/ie048948f

Alhammadi, A. A., Chen, Y., Yen, A., Wang, J., Creek, J. L., Vargas, F. M., and Chapman, W. G. (2017). Effect of the Gas Composition and Gas/Oil Ratio on Asphaltene Deposition. *Energy and Fuels*, *31*(4), 3610–3619. https://doi.org/10.1021/acs.energyfuels.6b02313

Asomaning, S., and Watkinson, A. P. (2000). Petroleum stability and heteroatom species effects in fouling of heat exchangers by asphaltenes. *Heat Transfer Engineering*, *21*(3), 10–16. https://doi.org/10.1080/014576300270852

Asomaning, Samuel. (1997). HEAT EXCHANGER FOULING BY PETROLEUM ASPHALTENES. PhD Dissertation. University of British Columbia.

Bae, J., Fouchard, D., Garner, S., Macias, J., and Champion, N. (2016, May 2-5). Advantages of Applying a Multifaceted Approach to Asphaltene Inhibitor Selection. OTC paper 27171, Offshore Technology Conference, Houston, Texas.

Barrera, D. M., Ortiz, D. P., and Yarranton, H. W. (2013). Molecular weight and density distributions of asphaltenes from crude oils. *Energy and Fuels*, *27*(5), 2474–2487. https://doi.org/10.1021/ef400142v

Bemani, A., Poozesh, A., Bahrami, M., and Ashoori, S. (2019). Experimental study of asphaltene deposition: Focus on critical size and temperature effect. *Journal of Petroleum Science and Engineering*, *181*. https://doi.org/10.1016/j.petrol.2019.106186

Broseta, D., Robin, M., Savvidis, T., Féjean, C., Durandeau, M., and Zhou, H. (2000, April 3 – 5). Detection of Asphaltene Deposition by Capillary Flow Measurements. SPE paper 59294, SPE/DOE Improved Oil Recovery Symposium, Tulsa, Oklahoma.

Calles, J. A., Dufour, J., Marugán, J., Peña, J. L., Giménez-Aguirre, R., and Merino-García, D. (2008). Properties of asphaltenes precipitated with different n-Alkanes. A study to assess the most representative species for modeling. *Energy and Fuels*, *22*(2), 763–769. https://doi.org/10.1021/ef700404p

Casas, Y. A., Duran, J. A., Schoeggl, F. F., and Yarranton, H. W. (2019). Settling of Asphaltene Aggregates in n-Alkane Diluted Bitumen. *Energy and Fuels*, *33*(11), 10687–10703. https://doi.org/10.1021/acs.energyfuels.9b02571

Castellanos-Díaz, O., Modaresghazani, J., Satyro, M. A., and Yarranton, H. W. (2011). Modeling the phase behavior of heavy oil and solvent mixtures. *Fluid Phase Equilibria*, *304*(1–2), 74–85. https://doi.org/10.1016/j.fluid.2011.02.011

Cenegy, L. (2001, September 30 - October 3). survey of Successful World-wide Asphaltene Inhibitor Treatments in Oil Production Fields, SPE paper 71542, SPE Annual Technical Conference and Exhibition, New Orleans, Louisiana.

Chaisoontornyotin, W., Haji-Akbari, N., Fogler, H. S., and Hoepfner, M. P. (2016). Combined Asphaltene Aggregation and Deposition Investigation. *Energy and Fuels*, *30*(3), 1979–1986. https://doi.org/10.1021/acs.energyfuels.5b02427

de Boer, R., Leerlooyer, K., Laboratorium, P., Eigner, M., IntI Petroleum Mij, S. B., and van Bergen, A. (1995). *Screening of Crude Oils for Asphalt Precipitation: Theory, Practice, and the Selection of Inhibitors*. http://onepetro.org/PO/article-pdf/10/01/55/2126087/spe-24987-pa.pdf/1

Dickie, J. P., and Fu Yen, T. (1967). Marcostructures of the Asphaltic Fractions by Various Instrumental Methods. *Analytical Chemistry., 39,* 1847-1852.

Ducker, W., Senden, T., and Pashley, R. (1992). Direct measurement of colloidal forces using an atomic force microscope. *Nature*.

Duran, J. A., Casas, Y. A., Xiang, L., Zhang, L., Zeng, H., and Yarranton, H. W. (2018). Nature of Asphaltene Aggregates. *Energy and Fuels, 33*(5), 3694-3710. https://doi.org/10.1021/acs.energyfuels.8b03057

Duran, J. A., Schoeggl, F. F., and Yarranton, H. W. (2019). Kinetics of asphaltene precipitation/aggregation from diluted crude oil. *Fuel*, *255*. https://doi.org/10.1016/j.fuel.2019.115859

E, H., and Watkinson, A. (2009). Precipitation and Fouling in Heavy Oil Diluent Blends. *Heat Transfer Engineering*, *30*(10–11), 786–796.

Ebert, W., and Panchal, C.B. (1997). Analysis of Exxon Crude Oil-Slip Stream Coking Data. *Fouling Mitigation of Industrial Heat Exchange Equipment,* ed. C.B. Panchal, pp.451-460, Begell House, New York.

Epstein, N. (1997). Elements of Particle Deposition onto Nonporous Solid Surfaces Parallel to Suspension Flows. *Experimental Thermal and Fluid Science*, *14*, 323–334.

Eskin, D., Ratulowski, J., Akbarzadeh, K., and Andersen, S. (2012). Modeling of asphaltene deposition in a production tubing. *AIChE Journal*, *58*(9), 2936–2948. https://doi.org/10.1002/aic.12800

Eskin, Dmitry, Mohammadzadeh, O., Akbarzadeh, K., Taylor, S. D., and Ratulowski, J. (2016). Reservoir impairment by asphaltenes: A critical review. *Canadian Journal of Chemical Engineering*, *94*(6), 1202–1217. https://doi.org/10.1002/cjce.22476

Eyssautier, J., Hénaut, I., Levitz, P., Espinat, D., and Barré, L. (2012). Organization of asphaltenes in a vacuum residue: A small-angle x-ray scattering (SAXS)-viscosity approach at high temperatures. *Energy and Fuels*, *26*(5), 2696–2704. https://doi.org/10.1021/ef201412j

Eyssautier, J., Levitz, P., Espinat, D., Jestin, J., Gummel, J., Grillo, I., and Barré, L. (2011). Insight into asphaltene nanoaggregate structure inferred by small angle neutron and X-ray scattering. *Journal of Physical Chemistry B*, *115*(21), 6827–6837. https://doi.org/10.1021/jp111468d

Ferworn, K. A., Svrcek, W. Y., and Mehrotra', A. K. (1993). Measurement of Asphaltene Particle Size Distributions in Crude Oils Diluted with n-Heptane. In *Ind. Eng. Chem. Res* (Vol. 32).

Fouchard, D., and Carmichael, J. (2014). Method of assessing asphaltene inhibitor efficiency.

Ghahfarokhi, A. K., Kor, P., Kharrat, R., and Soulgani, B. S. (2017). Characterization of asphaltene deposition process in flow loop apparatus; An experimental investigation and modeling approach. *Journal of Petroleum Science and Engineering*, *151*(July 2016), 330–340. https://doi.org/10.1016/j.petrol.2017.01.009

Gonzalez, D. L., Hirasaki, G. J., Creek, J., and Chapman, W. G. (2007). Modeling of asphaltene precipitation due to changes in composition using the perturbed chain statistical associating fluid theory equation of state. *Energy and Fuels*, *21*(3), 1231–1242. https://doi.org/10.1021/ef060453a

Gonzalez, D. L., Ting, P. D., Hirasaki, G. J., and Chapman, W. G. (2005). Prediction of asphaltene instability under gas injection with the PC-SAFT equation of state. *Energy and Fuels*, *19*(4), 1230–1234. https://doi.org/10.1021/ef049782y

Gray, M.R. (2015). *Upgrading Oilsands Bitumen and Heavy Oil.*

Grimaldos-Aguilar, F. A. (2018). Measurement of Liquid-Liquid Diffusion in Solvent-Bitumen Systems. MSc. Thesis. University of Calgary.

Guha, A. (2008). Transport and deposition of particles in turbulent and laminar flow. In *Annual Review of Fluid Mechanics* (Vol. 40, pp. 311–341). https://doi.org/10.1146/annurev.fluid.40.111406.102220

Hoepfner, M. P., Limsakoune, V., Chuenmeechao, V., Maqbool, T., and Scott Fogler, H. (2013). A fundamental study of asphaltene deposition. *Energy and Fuels*, *27*(2), 725–735. https://doi.org/10.1021/ef3017392

Hoepfner, M. P., Vilas Boîas Fávero, C., Haji-Akbari, N., and Fogler, H. S. (2013). The fractal aggregation of asphaltenes. *Langmuir*, *29*(28), 8799–8808. https://doi.org/10.1021/la401406k

Hu, Y.-F., and Guo, T.-M. (2001). Effect of temperature and molecular weight of n-alkane precipitants on asphaltene precipitation. In *Fluid Phase Equilibria* (Vol. 192).

Israelachvili, J., Min, Y., Akbulut, M., Alig, A., Carver, G., Greene, W., Kristiansen, K., Meyer, E., Pesika, N., Rosenberg, K., and Zeng, H. (2010). Recent advances in the surface forces apparatus (SFA) technique. *Reports on Progress in Physics*, *73*(3). https://doi.org/10.1088/0034-4885/73/3/036601

Jamialahmadi, M., Soltani, B., Müller-Steinhagen, H., and Rashtchian, D. (2009). Measurement and prediction of the rate of deposition of flocculated asphaltene particles from oil. *International Journal of Heat and Mass Transfer*, *52*(19–20), 4624–4634. https://doi.org/10.1016/j.ijheatmasstransfer.2009.01.049

Johnston, K. A., Satyro, M. A., Taylor, S. D., and Yarranton, H. W. (2017). Can a Cubic Equation of State Model Bitumen-Solvent Phase Behavior? *Energy and Fuels*, *31*(8), 7967–7981. https://doi.org/10.1021/acs.energyfuels.7b01104

Johnston, K. A., Schoeggl, F. F., Satyro, M. A., Taylor, S. D., and Yarranton, H. W. (2017). Fluid Phase Equilibria Phase behavior of bitumen and n- pentane. *Fluid Phase Equilibria*, *442*, 1–19. https://doi.org/10.1016/j.fluid.2017.03.001

Kelland, M. A. (2014). *Production chemicals for the oil and gas industry*. Boca Raton : CRC Press; Second edition.

Kuang, J., Tavakkoli, M., Yarbrough, J., Wang, J., Jain, S., Ashtekar, S., Abdallah, D. S., Punnapala, S., and Vargas, F. M. (2018). Investigation of Asphaltene Deposition at High Temperature and under Dynamic Conditions. *Energy and Fuels*, *32*(12), 12405–12415. https://doi.org/10.1021/acs.energyfuels.8b03318

Kurup, A. S., Vargas, F. M., Wang, J., Buckley, J., Creek, J. L., Subramani, H. J., and Chapman, W. G. (2011). Development and application of an asphaltene deposition tool (ADEPT) for well bores. *Energy and Fuels*, *25*(10), 4506–4516. https://doi.org/10.1021/ef200785v

Kurup, A. S., Wang, J., Subramani, H. J., Buckley, J., Creek, J. L., and Chapman, W. G. (2012). Revisiting asphaltene deposition tool (ADEPT): Field application. *Energy and Fuels*, *26*(9), 5702–5710. https://doi.org/10.1021/ef300714p

Li, Z., and Firoozabadi, A. (2010a). Modeling asphaltene precipitation by n-alkanes from heavy oils and bitumens using cubic-plus-association equation of state. *Energy and Fuels*, *24*(2), 1106–1113. https://doi.org/10.1021/ef9009857

Li, Z., and Firoozabadi, A. (2010b). Cubic-plus-association equation of state for asphaltene precipitation in live oils. *Energy and Fuels*, *24*(5), 2956–2963. https://doi.org/10.1021/ef9014263

Liu, J., Zhang, L., Xu, Z., and Masliyah, J. (2006). Colloidal interactions between asphaltene surfaces in aqueous solutions. *Langmuir*, *22*(4), 1485–1492. https://doi.org/10.1021/la052755v

Long, Y., Dabros, T., and Hamza, H. (2004). Structure of water/solids/asphaltenes aggregates and effect of mixing temperature on settling rate in solvent-diluted bitumen. *Fuel*, *83*(7–8), 823–832. https://doi.org/10.1016/j.fuel.2003.10.026

Mancilla-Polanco, A., Schoeggl, F. F., Johnston, K., Richardson, W. D. L., Yarranton, H. W., and Taylor, S. D. (2017). *SPE-184988-MS The Phase Behavior of Heavy Oil and Propane Mixtures*.

Maqbool, T., Balgoa, A.T., Fogler, H.S. (2009). Revisiting Asphaltene Precipitation from Crude oils: A Case of Neglected Kinetic Effects. *Energy Fuels*, *23*, 3681–3686.

Maqbool, T., Raha, S., Hoepfner, M. P., and Fogler, H. S. (2011). Modeling the aggregation of asphaltene nanoaggregates in crude oil-precipitant systems. *Energy and Fuels*, *25*(4), 1585–1596. https://doi.org/10.1021/ef1014132

Merino-Garcia, D., Murgich, J., and Andersen, S. I. (2004). Asphaltene self-association: Modeling and effect of fractionation with a polar solvent. *Petroleum Science and Technology*, *22*(7–8), 735–758. https://doi.org/10.1081/LFT-120038710

Motahhari, H., Satyro, M. A., Taylor, S. D., and Yarranton, H. W. (2013). Extension of the expanded fluid viscosity model to characterized oils. *Energy and Fuels*, *27*(4), 1881–1898. https://doi.org/10.1021/ef301575n

Mullins, O. C., and Research, S.-D. (2008). *Review of the Molecular Structure and Aggregation of Asphaltenes and Petroleomics*. http://onepetro.org/SJ/article-pdf/13/01/48/2125917/spe-95801-pa.pdf/1

Nabzar, L., and Aguiléra, M. E. (2008). The colloidal approach. A promising route for asphaltene deposition modelling. *Oil and Gas Science and Technology*, *63*(1 SPEC. ISS.), 21–35. https://doi.org/10.2516/ogst:2007083

Natarajan, A., Kuznicki, N., Harbottle, D., Masliyah, J., Zeng, H., and Xu, Z. (2014). Understanding mechanisms of asphaltene adsorption from organic solvent on mica. *Langmuir*, *30*(31), 9370–9377. https://doi.org/10.1021/la500864h

Natarajan, A., Xie, J., Wang, S., Masliyah, J., Zeng, H., and Xu, Z. (2011). Understanding molecular interactions of asphaltenes in organic solvents using a surface force apparatus. *Journal of Physical Chemistry C*, *115*(32), 16043–16051. https://doi.org/10.1021/jp2039674

Panuganti, S. R., Vargas, F. M., Gonzalez, D. L., Kurup, A. S., and Chapman, W. G. (2012). PC-SAFT characterization of crude oils and modeling of asphaltene phase behavior. *Fuel*, *93*, 658–669. https://doi.org/10.1016/j.fuel.2011.09.028

Perez Claro, Y. A., Schoeggl, F. F., Taylor, S. D., and Yarranton, H. W. (2019). Phase Behavior of Mixtures of Bitumen and n-Butane. *Energy and Fuels*, *33*(9), 8530–8543. https://doi.org/10.1021/acs.energyfuels.9b02113

Pfeiffer, J. P., and Saal, R. N. J. (1939, July 6-8). ASPHALTIC BITUMEN AS COLLOID SYSTEM. Sixteenth Colloid Symposium.

Powers, D. P., Sadeghi, H., Yarranton, H. W., and Van Den Berg, F. G. A. (2016). Regular solution based approach to modeling asphaltene precipitation from native and reacted oils: Part 1, molecular weight, density, and solubility parameter distributions of asphaltenes. *Fuel*, *178*, 218–233. https://doi.org/10.1016/j.fuel.2016.03.027

Punnapala, S., and Vargas, F. M. (2013). Revisiting the PC-SAFT characterization procedure for an improved asphaltene precipitation prediction. *Fuel*, *108*, 417–429. https://doi.org/10.1016/j.fuel.2012.12.058

Rahmani, N. H. G., Dabros, T., and Masliyah, J. H. (2005). Fractal structure of asphaltene aggregates. *Journal of Colloid and Interface Science*, *285*(2), 599–608. https://doi.org/10.1016/j.jcis.2004.11.068

Rahmani, N. H. G., Masliyah, J. H., and Dabros, T. (2003). Characterization of Asphaltenes Aggregation and Fragmentation in a Shear Field. *AIChE Journal,* 49(7), 1645-1655.

Ramirez-Corredores, M. M. (2017). Asphaltenes. In *The Science and Technology of Unconventional Oils* (pp. 41–222). Elsevier. https://doi.org/10.1016/b978-0-12-801225-3.00002-4

Ramos-Pallares, F., Schoeggl, F. F., Taylor, S. D., Satyro, M. A., and Yarranton, H. W. (2016). Predicting the Viscosity of Hydrocarbon Mixtures and Diluted Heavy Oils Using the Expanded Fluid Model. *Energy and Fuels*, *30*(5), 3575–3595. https://doi.org/10.1021/acs.energyfuels.5b01951

Ramos-Pallares, F., and Yarranton, H. W. (2020). Extending the Modified Regular Solution Model to Predict Component Partitioning to the Asphaltene-Rich Phase. *Energy and Fuels*, *34*(5), 5213–5230. https://doi.org/10.1021/acs.energyfuels.9b03489

Rastegari, K., Svrcek, W. Y., and Yarranton, H. W. (2004). Kinetics of asphaltene flocculation. *Industrial and Engineering Chemistry Research*, *43*(21), 6861–6870. https://doi.org/10.1021/ie049594v

Rudrake, A., Karan, K., and Horton, J. H. (2009). A combined QCM and XPS investigation of asphaltene adsorption on metal surfaces. *Journal of Colloid and Interface Science*, *332*(1), 22–31. https://doi.org/10.1016/j.jcis.2008.12.052

Saryazdi, F., Motahhari, H., Schoeggl, F. F., Taylor, S. D., and Yarranton, H. W. (2013). Density of hydrocarbon mixtures and bitumen diluted with solvents and dissolved gases. *Energy and Fuels*, *27*(7), 3666–3678. https://doi.org/10.1021/ef400330j

Seifried, Christine M., Crawshaw, J., and Boek, E. S. (2013). Kinetics of asphaltene aggregation in crude oil studied by confocal laser-scanning microscopy. *Energy and Fuels*, *27*(4), 1865–1872. https://doi.org/10.1021/ef301594j

Seifried, Christine Maria, Al Lawati, S., Crawshaw, J. P., and Boek, E. S. (2013, September 30-October 2). Asphaltene Deposition in Capillary Flow. SPE paper 166289, SPE Annual Technical Conference and Exhibition, New Orleans, Louisiana.

Soleimani-Khormakala, H., Torkaman, M., and Bahrami, M. (2019). The Effect of Shear Rate on Aggregation and Fragmentation of Asphaltene Aggregates. *Journal of Dispersion Science and Technology*, *40*(6), 836–845. https://doi.org/10.1080/01932691.2018.1485579

Speight, J. G., and Long, R. B. (1996). Concept of asphaltenes revisited. *Fuel Science and Technology International*, *14*(1–2), 1–12. https://doi.org/10.1080/08843759608947559

Speight, J. (2007). *The Chemistry and Technology of Petroleum* (4th ed.)

Srivastava, R., Huang, S., and Dong, M. (1999). *Asphaltene Deposition During CO 2 Flooding*.

Torkaman, M., Bahrami, M., and Dehghani, M. R. (2018). Influence of Temperature on Aggregation and Stability of Asphaltenes. II. Orthokinetic Aggregation. *Energy and Fuels*, *32*(5), 6144–6154. https://doi.org/10.1021/acs.energyfuels.7b03601

Vargas, F. M., Creek, J. L., and Chapman, W. G. (2010). On the development of an asphaltene deposition simulator. *Energy and Fuels*, *24*(4), 2294–2299. https://doi.org/10.1021/ef900951n

Vilas Bôas Fávero, C., Hanpan, A., Phichphimok, P., Binabdullah, K., and Fogler, H. S. (2016). Mechanistic Investigation of Asphaltene Deposition. *Energy and Fuels*, *30*(11), 8915–8921. https://doi.org/10.1021/acs.energyfuels.6b01289

Wang, J., Buckley, J. S., and Creek, J. L. (2004). Asphaltene deposition on metallic surfaces. *Journal of Dispersion Science and Technology*, *25*(3), 287–298. https://doi.org/10.1081/DIS-120037697

Wang, S., Liu, J., Zhang, L., Masliyah, J., and Xu, Z. (2010). Interaction forces between asphaltene surfaces in organic solvents. *Langmuir*, *26*(1), 183–190. https://doi.org/10.1021/la9020004

Watkinson, A. Paul. (2007). Deposition from crude oils in heat exchangers. *Heat Transfer Engineering*, *28*(3), 177–184. https://doi.org/10.1080/01457630601064413

Watkinson, Alan Paul. (1968). PARTICULATE FOULING OF SENSIBLE HEAT EXCHANGERS. PhD Dissertation. University of British Columbia.

Wiehe, I. A., Yarranton, H. W., Akbarzadeh, K., Rahimi, P. M., and Teclemariam, A. (2005). The paradox of asphaltene precipitation with normal paraffins. *Energy and Fuels*, *19*(4), 1261–1267. https://doi.org/10.1021/ef0496956

Xie, K., and Karan, K. (2005). *Kinetics and Thermodynamics of Asphaltene Adsorption on Metal Surfaces: A Preliminary Study †*. https://doi.org/10.1021/ef049689

Yarranton, H. W., Ortiz, D. P., Barrera, D. M., Baydak, E. N., Barré, L., Frot, D., Eyssautier, J., Zeng, H., Xu, Z., Dechaine, G., Becerra, M., Shaw, J. M., McKenna, A. M., Mapolelo, M. M., Bohne, C., Yang, Z., and Oake, J. (2013). On the size distribution of self-associated asphaltenes. *Energy and Fuels*, *27*(9), 5083–5106. https://doi.org/10.1021/ef400729w

Yarranton, Harvey W., and Ramos-Pallares, F. (2021). Regular solution theory applied to asphaltene related phase behaviour. *Canadian Journal of Chemical Engineering*, *99*(5), 1050–1067. https://doi.org/10.1002/cjce.24059

Yaws, C.L. (2014). Transport Properties of Chemicals and Hydrocarbons: Second Edition. In *Transport Properties of chemical and Hydrocarbons: Second Edition.* https://doi.org/10.1016/C2013-0-12644-X

Yeap, B. L., Wilson, D. I., Polley, G. T., and Pugh, S. J. (2005). Retrofitting crude oil refinery heat exchanger networks to minimize fouling while maximizing heat recovery. *Heat Transfer Engineering*, *26*(1), 23–34. https://doi.org/10.1080/01457630590890139

Zahabi, A., Gray, M. R., and Dabros, T. (2012). Kinetics and properties of asphaltene adsorption on surfaces. *Energy and Fuels*, *26*(2), 1009–1018. https://doi.org/10.1021/ef2014698

Zhang, L., Shi, C., Lu, Q., Liu, Q., and Zeng, H. (2016). Probing Molecular Interactions of Asphaltenes in Heptol Using a Surface Forces Apparatus: Implications on Stability of Water-in-Oil Emulsions. *Langmuir*, *32*(19), 4886–4895. https://doi.org/10.1021/acs.langmuir.6b01000

Zhang, W., Wang, Y., and Ren, T. (2017). Influence of injection pressure and injection volume of CO2 on asphaltene deposition. *Petroleum Science and Technology*, *35*(4), 313–318. https://doi.org/10.1080/10916466.2016.1258419

Zhang, Yan, Takanohashi, T., Sato, S., Saito, I., and Tanaka, R. (2004). Observation of glass transition in asphaltenes. *Energy and Fuels*, *18*(1), 283–284. https://doi.org/10.1021/ef0301147

Zhang, Yechun, Arya, A., Kontogeorgis, G., and Yarranton, H. (2019). Modeling the phase behaviour of bitumen/n-alkane systems with the cubic plus association (CPA) equation of state. *Fluid Phase Equilibria*, *486*, 119–138. https://doi.org/10.1016/j.fluid.2019.01.004

Zúñiga-Hinojosa, M. A., Justo-García, D. N., Aquino-Olivos, M. A., Román-Ramírez, L. A., and García-Sánchez, F. (2014). Modeling of asphaltene precipitation from n-alkane diluted heavy oils and bitumens using the PC-SAFT equation of state. *Fluid Phase Equilibria*, *376*, 210–224. https://doi.org/10.1016/j.fluid.2014.06.004

Appendix A: Modified Regular Solution Model

This appendix presents the modified regular solution (MRS) model which was used to predict the amount of asphaltene partitioning to the heavy phase; that is, the asphaltene yield. The MRS model is an activity coefficient based model and a liquid-liquid equilibrium is assumed between the asphaltene-rich heavy phase and the solvent-rich light phase. Details of the MRS model are provided elsewhere (Alboudwarej *et al.* 2003; Akbarzadeh *et al.* 2005; Ramos-Pallares and Yarranton, 2020).

The partition coefficient for a component in the mixture at equilibrium can be calculated as follows:

$$K_i = \frac{x_i^H}{x_i^L} = \frac{\gamma_i^L}{\gamma_i^H} \tag{A.1}$$

where K_i is the partition coefficient for component i in the mixture, x is the mole fraction, γ is the activity coefficient, and superscript L and H denote the light and heavy phase, respectively. The activity coefficient for the light phase is defined as a summation of an enthalpic contribution from a regular solution and an entropic contribution due to mixing molecules of different sizes and is determined as follows:

$$\ln \gamma_i^L = \ln \left(\frac{v_i}{v^L} \right) + 1 - \frac{v_i}{v^L} + \frac{v_i}{RT} (\delta_i - \delta^L)^2 \tag{A.2}$$

where v is the molar volume, R is the universal gas constant, T is the absolute temperature, and δ is the solubility parameter. For the heavy phase, the activity coefficient consists only of the enthalpic component from a regular solution with an ideal entropy of mixing as shown below:

$$\ln \gamma_i^H = \frac{v_i}{RT} (\delta_i - \delta^H)^2 \tag{A.3}$$

The molar volume of a phase is calculated using the molar average of all the components (SARA) in the phase as follows:

$$v^\alpha = \sum x_i^\alpha v_i \tag{A.4}$$

where the superscript α represents the heavy or light phase. The solubility parameter of a phase is determined as a volumetric average given by:

$$\delta^\alpha = \sum \varphi_i^\alpha \delta_i \tag{A.5}$$

The required inputs to the model are the temperature, pressure, composition of the fluid, and the molecular weight, density, and solubility parameter of each component. The temperature, pressure, and composition must be specified. In this case, the composition and properties must be specified for a mixture of *n*-heptane and bitumen. The properties of *n*-alkanes are known and are available elsewhere (Yarranton and Ramos-Pallares, 2021). The bitumen is characterized into pseudo-components corresponding to SARA fractions where the asphaltene fraction is defined as the *n*-pentane insoluble fraction of the oil (C5-asphaltenes). Correlations are available for the properties of saturates, aromatics, and resins (Yarranton and Ramos-Pallares, 2021). Some of the asphaltene properties must be tuned and therefore asphaltenes are discussed in more detail below.

The asphaltenes are further divided into pseudo-components based on their molecular weights using a gamma distribution function as discussed by Akbarzadeh *et al.* (2005). The density of each asphaltene pseudo-component at standard conditions (25°C, 0.1 MPa) is calculated with the following correlation (Ramos-Pallares and Yarranton, 2020):

$$\rho_{A,i}^0 = 1047 + 151.4[1 - exp(-9w_{A,i})] \qquad (A.6)$$

where $\rho_{A,i}^0$ is the density of pseudo-component *i* at 25°C and 0.1 MPa, and $w_{A,i}$ is the mass fraction of pseudo-component *i*. At higher temperatures, the density of the asphaltenes is calculated as follows (Ramos-Pallares and Yarranton, 2020):

$$\rho_{A,i} = \rho_{A,i}^0 - (3.1635 - 0.00239\rho_{A,i}^0)(T - 298.15) \qquad (A.7)$$

where $\rho_{A,i}$ is the density of pseudo-component *i* at the temperature of the system. The asphaltenes are assumed to be incompressible.

The solubility parameter of each asphaltene pseudo-component at standard conditions (25°C, 0.1 MPa) is calculated as follows (Powers *et al.* 2016):

$$\delta_{A,i}^0 = \delta_{min}^0 + (\delta_{max}^0 - \delta_{min}^0)w_{A,i}^{1.2} \qquad (A.8)$$

where $\delta_{A,i}^0$ is the solubility parameter of pseudo-component *i* at 25°C and 0.1 MPa, subscripts "*max*" and "*min*" represent the maximum and minimum solubility parameter of the distribution, and $w_{A,i}$ is the mass fraction of pseudo-component *i*. The values of δ_{min}^0 and δ_{max}^0 are determined by fitting the model to experimental yield data. For this thesis, the tuned values of δ_{min}^0 and δ_{max}^0 were 19.65 MPa$^{0.5}$ and 20.08 MPa$^{0.5}$ respectively. The measured and modeled asphaltene yields

from the WC-B-A3 bitumen diluted with *n*-heptane are shown in Figure A.1. The following correlation was used to calculate the solubility parameter of the asphaltenes at higher temperatures (Ramos-Pallares and Yarranton, 2020):

$$\delta_{A,i} = \delta_{A,i}^0 - 0.0191(T - 298.15) \tag{A.9}$$

where $\delta_{A,i}$ is the the solubility parameter of pseudo-component *i* at the temperature of the system. The asphaltene solubility parameters are assumed to be independent of pressure.
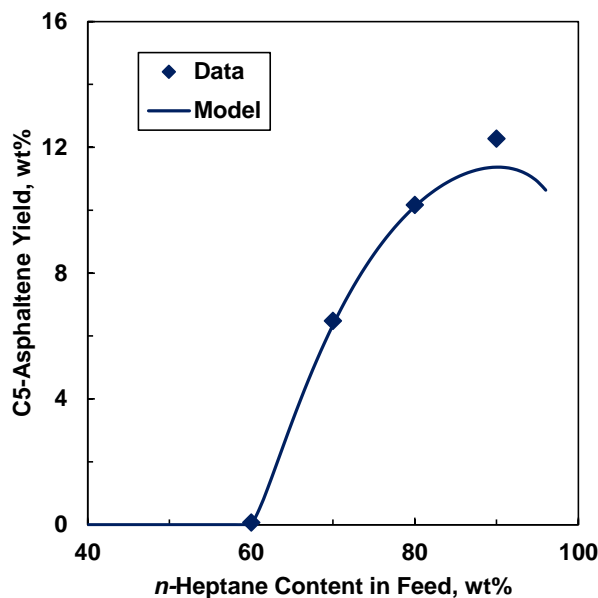
Figure A.1 Measured and modeled asphaltene yields from WC-B-A3 bitumen diluted with *n*-heptane at 25°C and 0.1 MPa.

Once the solubility parameter is known, the model can be used to determine the liquid-liquid equilibrium at different conditions. The MRS model has been shown to predict C5-asphaltene and bitumen yields from mixtures of *n*-alkanes with carbon numbers greater than 4 to within ±1 wt% and ±2 wt% respectively (Yarranton and Ramos-Pallares, 2021). Figures A.2a and A2.b show the modeled C5-asphaltene and bitumen yields at the experimental conditions considered in this thesis.
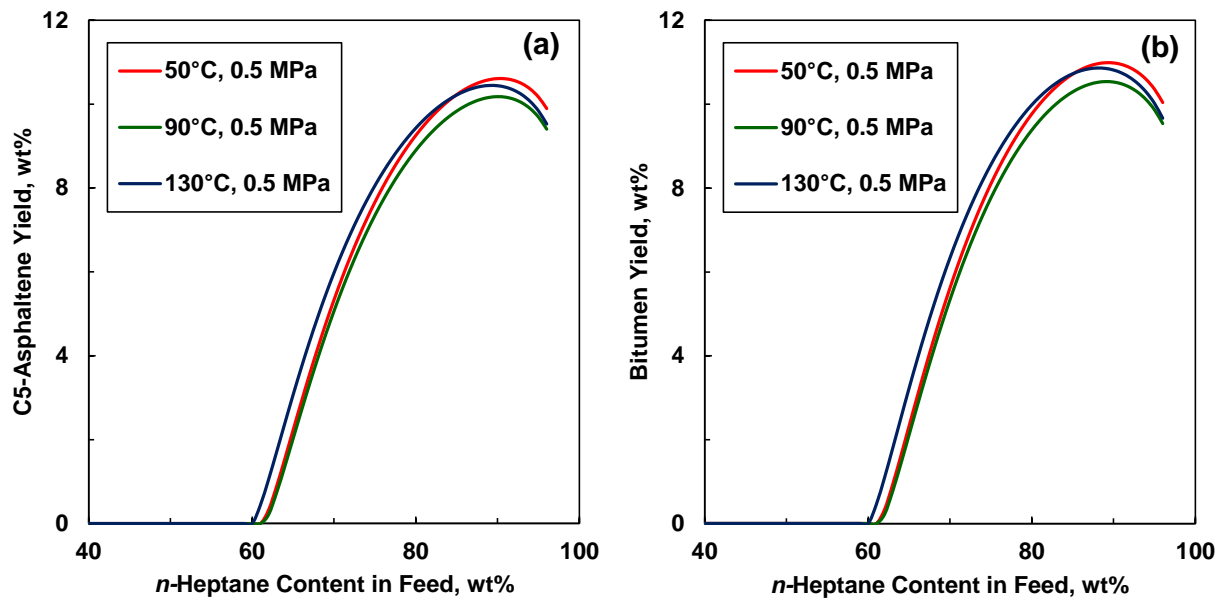
Figure A.2 Predicted yields from WC-B-A3 bitumen diluted with *n*-heptane at various temperatures and 0.5 MPa: a) C5-asphaltenes only; b) bitumen.

Appendix B: Density and Viscosity Correlations

This appendix presents the correlations used to predict the density and viscosity of n-heptane and bitumen mixtures.

B.1. Density Correlation

The effective density of n-heptane was calculated using the following correlation (Saryazdi *et al.* 2013):

$$\rho_{C7} = (a_1^* + a_2^*T) + [(b_1^* + b_2^*T)P] \tag{B.1}$$

where ρ_{C7} is the effective density of n-heptane, a_1^*, a_2^*, b_1^* and b_2^* are fluid-specific parameters, T is the absolute temperature in K, and P is the pressure in MPa. The fluid-specific parameters for n-heptane are listed in Table B.1.

Table B.1: Fluid-specific parameters for n-heptane for the effective density correlation from Saryazdi *et al.* 2013.

Component	a_1^* kg/m^3	a_2^* kg/(m^3·K)	b_1^* kg/(m^3·MPa)	b_2^* kg/(m^3·MPa·K)
n-heptane	918.603	-0.79155	-0.17738	0.002692

The density of the WC-B-A3 bitumen used in this thesis was measured by Grimaldo-Aguilar (2018) and fitted with the following empirical equation (Saryazdi *et al.* 2013):

$$\rho_{bit} = (A^* - B^*T)exp\{[C^*\exp(D^*T](P - 0.1)\} \tag{B.2}$$

where ρ_{bit} is the density of the bitumen, T is the absolute temperature in K, P is the pressure in MPa, and A^*, B^*, C^*, and D^* are fitting parameters. The fitting parameters are shown in Table B.2.

Table B.2: Fitting parameters for WC-B-A3 bitumen in density correlation.

Component	A^* kg/m^3	B^* kg/(m^3·K)	C^* 1/MPa	D^* 1/K
WC-B-A3	1196.2	0.63743	0.00014	0.00433

The density of the mixture was calculated using the mixing rule developed by Saryazdi *et al.* (2013). For a binary system of n-heptane and bitumen, the mixing rule is given by:

$$\rho_{mix} = \left[\frac{w_{C7}}{\rho_{C7}} + \frac{w_{bit}}{\rho_{bit}} - w_{C7}w_{bit}\left(\frac{1}{\rho_{C7}} + \frac{1}{\rho_{bit}}\right)\beta_{sb}\right] \qquad \text{(B.3)}$$

where ρ_{mix} is the mixture density, w_{C7} is the weight fraction of n-heptane in the mixture, w_{bit} is the weight fraction of bitumen in the mixture, and β_{sb} is the density binary interaction parameter between solvent and bitumen. The binary interaction parameter was determined using the following correlations (Saryazdi *et al.* 2013):

$$\beta_{sb} = \beta_{sb}^{298} + 8.74 \times 10^{-5}(T - 298) \qquad \text{(B.4)}$$

$$\beta_{sb}^{298} = -0.092\left|0.435 - 2\left(\frac{|v_{C7298} - v_{bit298}|}{(v_{C7298} + v_{bit298})}\right)\right| + 0.022 \qquad \text{(B.5)}$$

where β_{sb}^{298} is the binary interaction parameter between solvent and bitumen at 298 K, v_{C7298} and v_{bit298} are the specific volume of heptane and bitumen respectively at 298 K.

The predicted densities of the n-heptane-bitumen mixtures at the experimental conditions are shown in Table B.3. The fitted densities of n-heptane and bitumen by Eq. B.1 and Eq. B.2 are expected to have a maximum deviation of 0.7 kg/m³ and 0.3 kg/m³ respectively (Grimaldo-Aguilar, 2018). The predicted densities of the n-heptane-bitumen mixtures are expected to have an average deviation of less than 1% from the actual value for the range of temperatures and pressures used in this thesis (Saryazdi *et al.* 2013).

Table B.3: Density and viscosity of WC-B-A3 bitumen and n-heptane mixtures at 500 kPa.

n-heptane composition (wt%)	Temperature °C	Density kg/m³	Viscosity mPa·s
65	50	756.2	1.094
75	50	727.7	0.719
90	50	687.9	0.423
65	90	725.5	0.677
75	90	696.7	0.474
90	90	656.5	0.298
65	130	694.7	0.463
75	130	665.5	0.334
90	130	625.0	0.222

B.2 Viscosity Correlation

The Expanded Fluid Viscosity Model (Yarranton and Satyro, 2009; Motahari *et al.* 2013; Ramos-Pallares *et al.* 2016) was used to calculate the viscosity of pure fluids and mixtures. For a pure component, the viscosity is calculated as a density dependent departure function from its dilute gas viscosity:

$$\mu - \mu_D = 0.165(\exp(c_2\beta) - 1) \tag{B.6}$$

where μ_D is the dilute gas viscosity, c_2 is a fluid-specific parameter, and β is a parameter that correlates changes in density to changes in viscosity that can be determined as follows:

$$\beta = \frac{1}{exp\left(\left(\frac{\rho_s^*}{\rho}\right)^{0.65} - 1\right) - 1} \tag{B.7}$$

where ρ is the fluid density and ρ_s^* is the compressed state density given by:

$$\rho_s^* = \frac{\rho_s^0}{\exp(-c_3 P)} \tag{B.8}$$

where P is the pressure in MPa, and c_3 and ρ_s^0 are fluid specific parameters. The fluid-specific parameters for *n*-heptane and the WC-B-A3 bitumen are listed in Table B.4. The parameters for *n*-heptane were obtained from Ramos-Pallares *et al.* (2016). The parameters for the bitumen were obtained by fitting Eq. B.6 to experimental data collected by Grimaldo-Aguilar (2018). The model fit the bitumen viscosity with an average absolute relative deviation of 1.1%, within the measurement error of 2.8% reported by Grimaldo-Aguilar (2018).

Table B.4: Expanded Fluid Model fluid-specific parameters.

Component	ρ_s^0 kg/m^3	c_2	c_3 10^{-3} MPa^{-1}
n-heptane	857.8	0.2130	0.17
WC-B-A3	1061.2	0.63743	0.34

The dilute gas viscosity is calculated using the following empirical correlation:

$$\mu_D = A_0 + B_0 T + D_0 T^2 + E_0 T^3 \tag{B.9}$$

where T is the temperature in K, A_0, B_0, D_0, and E_0 are fitting parameters that were obtained from Yaws (2018).

The viscosity of the mixture is determined from the Expanded Fluid model using mixture parameters obtained from mixing rules (Motahari *et al.* 2013). For a binary system of *n*-heptane and bitumen, the mixture parameters are calculated as follows:

$$\rho_{s,mix}^0 = \left[\frac{w_{C7}}{\rho_{C7}^0} + \frac{w_{bit}}{\rho_{bit}^0} - w_{C7}w_{bit}\left(\frac{1}{\rho_{C7}^0} + \frac{1}{\rho_{bit}^0}\right)\varepsilon_{sb} \right]^{-1} \tag{B.10}$$

$$\frac{c_{2,mix}}{\rho_{s,mix}^0} = \left[\frac{w_{C7}c_{2,C7}}{\rho_{C7}} + \frac{w_{bit}c_{2,bit}}{\rho_{bit}} - w_{C7}w_{bit}\left(\frac{c_{2,C7}}{\rho_{C7}} + \frac{c_{2,bit}}{\rho_{bit}}\right)\varepsilon_{sb} \right] \tag{B.11}$$

$$c_{3,mix} = \left[\frac{w_{C7}}{c_{3,C7}} + \frac{w_{bit}}{c_{3,bit}} \right]^{-1} \tag{B.12}$$

$$\mu_{D,mix} = \sum_{m=1}^{nc} \frac{x_m \mu_{D,m}}{\sum_{n=1}^{nc} x_n \delta_{mn}} \tag{B.13}$$

$$\delta_{mn} = \frac{\left[1 + (\mu_{D,m}/\mu_{D,n})^{0.5}(MW_n/MW_m)^{0.25} \right]^2}{[8(1 + MW_m/MW_n)]} \tag{B.14}$$

$$\varepsilon_{sb} = 0.038304 - 0.10478 \Delta SG_{norm} \tag{B.15}$$

$$\Delta SG_{norm} = \frac{2|SG_{C7} - SG_{bit}|}{SG_{C7} + SG_{bit}} \tag{B.16}$$

where *nc* is the number of components in the system, δ_{mn} is a fitting parameter for the dilute gas viscosity mixing rule, x_m and MW_m are the mole fraction and molecular weight of component "*m*" respectively, ε_{sb} is the viscosity binary parameter between solvent and bitumen, SG_{C7} is the specific gravity of *n*-heptane, and SG_{bit} is the specific gravity of bitumen.

The predicted viscosity of the *n*-heptane-bitumen mixture at various experimental conditions were shown in Table B.3. The predicted viscosities of the *n*-heptane-bitumen mixtures are expected to have an average deviation of 14% from the actual value (Ramos-Pallares *et al.* 2016).

Appendix C: Geometric Relations for Asphaltene-Rich Heavy Phase in Liquid Droplet Regime

This appendix presents the geometric relations used to calculate the height of the asphaltene-rich heavy phase liquid at 130°C. A schematic for the cross-sectional area of the capillary tube filled with heavy phase is shown in Figure C.1.
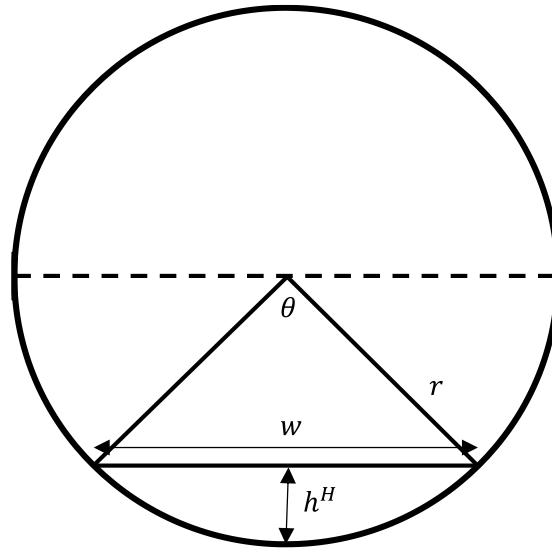
Figure C.1 Schematic for cross-sectional area of capillary tube.

In Figure C.1, h^H is the height of the heavy phase, r is the radius of the capillary tube, θ is the central angle, and w is the width of the circle segment. Assuming that the height of the heavy phase is uniform for the entire length of the tube, the area occupied by the light and heavy phases can be calculated as follows:

$$A^H = \frac{V^H}{L} \tag{C.1}$$

$$A^L = A_\Sigma - A^H \tag{C.2}$$

where V^H is volume occupied by the heavy phase, L is the length of the capillary tube, A^H is the area occupied by the heavy phase, A^L is the area occupied by the light phase, and A_Σ is the total cross-sectional area of the tube.

The following procedure is used when the heavy phase occupies less than half the tube ($V^H \leq \frac{1}{2}V_\Sigma$). An iterative approach is used to solve for the central angle of the circle. An initial guess is made for the central angle and the area occupied by the heavy phase is calculated using Eq. C.3 below. Next, the calculated area is compared with the area obtained from Eq. C.1. The process is repeated with new values of the central angle until the calculated area from both equations match each other. Once the central angle of the circle is known, it is used to solve for the height of the heavy phase, height of the light phase, width of the circle segment, and the wetted perimeter for both the heavy and light phases using the following relationships:

$$A^H = \frac{r^2}{2}(\theta - \sin\theta) \tag{C.3}$$

$$h^H = r\left(1 - \cos\frac{\theta}{2}\right) \tag{C.4}$$

$$h^L = D - h^H \tag{C.5}$$

$$w = 2\sqrt{wrh^H - h^{H^2}} \tag{C.6}$$

$$P^H = D - h^L \tag{C.7}$$

$$P^L = \pi D - P^H + 2w \tag{C.8}$$

where h^L is the height of the light, D is the diameter of the capillary tube, P^H is the wetted perimeter of the heavy phase, P^L and is the wetted perimeter of the light phase.

When the volume of the heavy phase occupies more than half of the total volume of the capillary tube, the light phase occupies less than half of the tube and the problem is simply a mirror image and is solved in the same way using the light phase as the basis.

Appendix D: Heavy Phase as a Propagating Front

If the heavy phase layer accumulated as a propagating front, similar to saturation changes in porous media, the accumulation rate would be highest at the front end of the tube and would decrease along the length of the tube. In addition, the pressure drop profiles would scale to throughput where throughput is defined as the number of pipe volumes displaced through the tube. Figure D.1 shows that the pressure drop profiles do not collapse onto a single curve when plotted versus throughput.
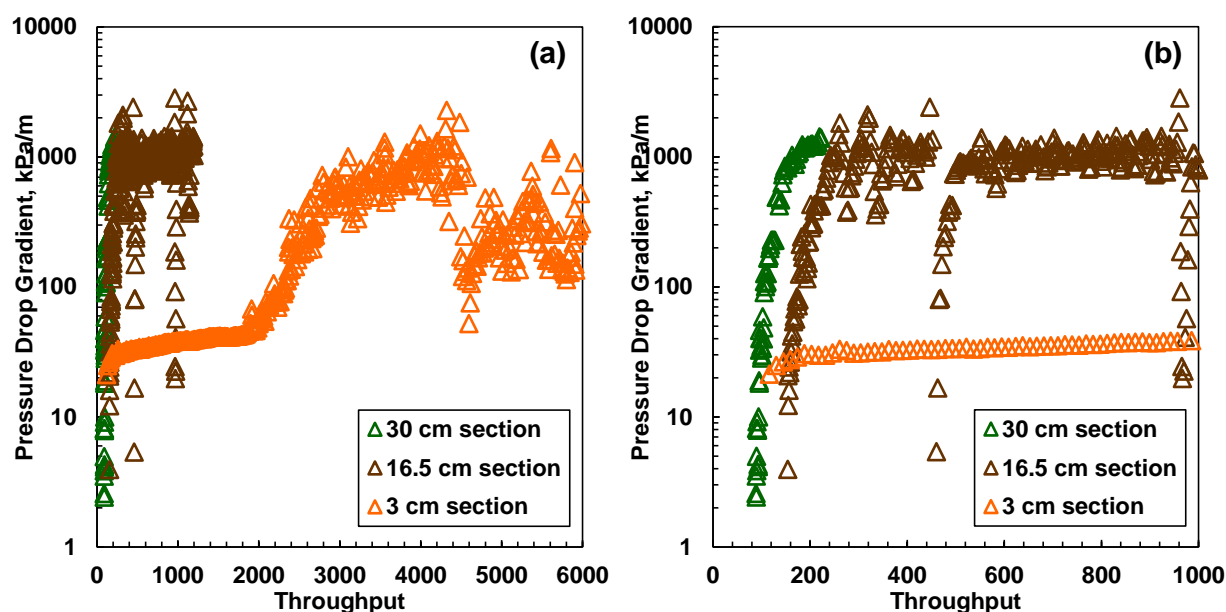
Figure D.1 Pressure drop gradient profile for a 90:10 H:B feed at 130°C and 2.2 cm³/min with different test section lengths. Pressure drop gradient versus throughput for: a) the entire throughput duration; b) the initial 1000 throughput period. The uncertainty of the pressures is ±0.25 kPa.

The accumulation rate is examined in terms of the accumulation efficiency, here defined as the fraction of the heavy phase that flowed through the tube (or tube section) over a given time that settles into the heavy phase flowing layer. The settling efficiency of the asphaltene liquid droplets at 130°C and a flow rate of 2.2 cm³/min is examined here as an example. First, the procedure to determine the settling efficiency in each tube section is presented. Then, the effects of the *n*-heptane content in the feed and capillary tube length are discussed.

Using the mass distribution of the dried "deposits" along the capillary tube, the wet mass of the heavy phase in each tube section can be calculated as follows:

$$m_{wet\ dep}^i = m_{dry\ dep}^i \left(\frac{m_{wet\ dep}}{m_{dry\ dep}}\right) \tag{D.1}$$

where $m_{wet\ dep}^i$ is the wet mass of deposit in the ith section, $m_{dry\ dep}^i$ is the dry mass of deposit in the ith section, $m_{wet\ dep}$ is the total wet mass of the deposit, and $m_{dry\ dep}$ is the total dry mass of the deposit. Next the total mass of heavy phase that flowed through the capillary tube in an experiment is given by:

$$m^H = \left(\frac{\dot{m}_{bit}^H}{1 - w_{C7\ dep}}\right) t \tag{D.2}$$

where m^H is the total mass of heavy phase, $\dot{m}_{bit}^H$ is the bitumen flow rate in the heavy phase, $w_{C7\ dep}$ is the mass fraction of n-heptane in the deposit, and t is the runtime of the experiment. Finally, the accumulation efficiency of the heavy phase per tube section can be calculated as follows:

$$\psi^i = \frac{m_{wet\ dep}^i}{m^H L^i} \tag{D.3}$$

where ψ^i is the accumulation efficiency of the heavy phase in the ith section and L^i is the length of the capillary tube in the ith section. To consider the effect of heavy phase droplet removal in later sections of the capillary tube, the wet mass of the deposit in preceding tube sections must be subtracted from the total heavy phase mass when calculating the accumulation efficiency. For example, the accumulation efficiency of the heavy phase in the second tube section when considering the effects of heavy phase removal is given by:

$$\psi^2 = \frac{m_{wet\ dep}^2}{(m^H - m_{wet\ dep}^1) L^2} \tag{D.4}$$

Table D.1 shows the wet mass distribution and Table D.2 shows the effect of droplet removal on heavy phase accumulation efficiency for a mixture containing 75 wt% n-heptane and 25 wt% bitumen in a 30 cm long capillary tube. In both cases, the accumulation efficiency of the heavy phase droplets are very low and are relatively uniform across the entire length of the capillary tube. When the effect of droplet removal is considered, the later segments of the test section show an increase in accumulation efficiency. However, the magnitude of these increases are minute. In other words, the effect of droplet removal is negligible and the amount of asphaltene settling is

controlled by the accumulation efficiency. For the remaining tables in this appendix, the effect of droplet removal will be ignored in the accumulation efficiency calculations.

Table D.1: Heavy phase wet mass distribution for a 75:25 H:B feed in a 30 cm (1.75 mm I.D) capillary tube at 2.2 cm³/min and 130°C.

H:B (w/w)	1st (mg)	2nd (mg)	3rd (mg)	4th (mg)	Total (mg)
75:25	127	148	152	147	573

Table D.2: Effect of heavy phase droplet removal on accumulation efficiency for a 75:25 H:B feed in a 30 cm (1.75 mm I.D) capillary tube at 2.2 cm³/min and 130°C.

Droplet Removal	ψ^1 (10^{-3} cm^{-1})	ψ^2 (10^{-3} cm^{-1})	ψ^3 (10^{-3} cm^{-1})	ψ^4 (10^{-3} cm^{-1})	ψ (10^{-3} cm^{-1})
No	1.42	1.66	1.74	1.64	1.62
Yes	1.42	1.68	1.79	1.71	1.62

Table D.3 shows the heavy phase wet mass distribution along the capillary tube at three different feed n-heptane contents while Table D.4 shows the accumulation efficiencies for these experiments. The accumulation efficiency increased with n-heptane content at all of the conditions considered in this thesis, which is consistent with faster settling or greater cohesion between heavy phase droplets at higher solvent contents. The accumulation efficiencies are uniform along the length of the tube in the 75:25 H:B and 90:10 H:B runs. In the 65:35 H:B run, the accumulation efficiency is highest near the inlet because an obstruction had formed at the inlet at this condition.

Table D.3: Effect of feed composition on wet mass distribution in a 30 cm (1.75 mm I.D) capillary tube at 2.2 cm³/min and 130°C.

H:B (w/w)	1st (mg)	2nd (mg)	3rd (mg)	4th (mg)	Total (mg)
65:35	110	26	48	-16	168
65:35	242	54	-2	62	357
75:25	127	148	152	147	573
90:10	120	160	164	138	582

Table D.4: Effect of feed composition on accumulation efficiency in a 30 cm (1.75 mm I.D) capillary tube at 2.2 cm³/min and 130°C.

H:B (w/w)	ψ^1 $(10^{-3}$ cm$^{-1})$	ψ^2 $(10^{-3}$ cm$^{-1})$	ψ^3 $(10^{-3}$ cm$^{-1})$	ψ^4 $(10^{-3}$ cm$^{-1})$	ψ $(10^{-3}$ cm$^{-1})$
65:35	0.80	0.20	0.34	-0.12	0.31
65:35	1.82	0.41	-0.01	0.46	0.66
75:25	1.42	1.66	1.74	1.64	1.62
90:10	10.3	13.8	14.4	11.8	12.6

The wet mass distribution along capillary tubes with varying lengths are shown in Table D.5 and the corresponding accumulation efficiencies are shown in Table D.6. While the absolute masses differ between runs, the overall accumulation efficiencies in the runs with the 3 cm and 16.5 cm tubes were similar, whereas the accumulation efficiency in the 30 cm tube was significantly higher. It is possible that the accumulation efficiency in the 30 cm tube may be inflated due to a shorter runtime of 75 minutes (lower total heavy phase mass) compared to 220 minutes in the 3 cm and 16.5 cm tubes. Since the heavy phase holdup in both the 16.5 cm and 30 cm tube reached 98% at the end of the exponential growth period at approximately the same time, it is also possible that the actual accumulation efficiency for the 16.5 cm tube is underestimated. In other words, the initial accumulation efficiency in the 16.5 cm tube is high but eventually, a steady state balance will be reached between heavy phase settling and removal and the calculated accumulation efficiency will continue to decrease as a function of runtime.

Table D.5: Heavy phase wet mass distribution for a 90:10 H:B feed in a (1.75 mm I.D) capillary tube at 2.2 cm³/min and 130°C with varying test section lengths.

Test Section Length (cm)	1st (mg)	2nd (mg)	3rd (mg)	4th (mg)	Total (mg)
3	-	-	-	-	59
16.5	62	72	88	102	325
30	120	160	164	138	582

Table D.6: Effect of test section length on accumulation efficiency for a 90:10 H:B feed at 2.2 cm³/min and 130°C.

Test Section Length (cm)	ψ^1 (10^{-3} cm^{-1})	ψ^2 (10^{-3} cm^{-1})	ψ^3 (10^{-3} cm^{-1})	ψ^4 (10^{-3} cm^{-1})	ψ (10^{-3} cm^{-1})
3					4.24
16.5	3.39	4.09	4.84	5.18	4.39
30	10.3	114	14.4	11.8	12.6

Overall, neither the pressure drop profiles nor the accumulation efficiencies are consistent with a heavy phase that accumulates as a propagating front. They are more consistent with a vertically rising layer of flowing heavy phase.